

NAVAL POSTGRADUATE SCHOOL MONTEREY, CALIFORNIA



THESIS

**EVOLUTION OF THE TEMPERATURE PROFILE IN
A SIMPLE THERMOACOUSTIC STACK**

by

Arthur R. Salindong

and

David D. Hebert

DTIC QUALITY INSPECTED 2

December, 1996

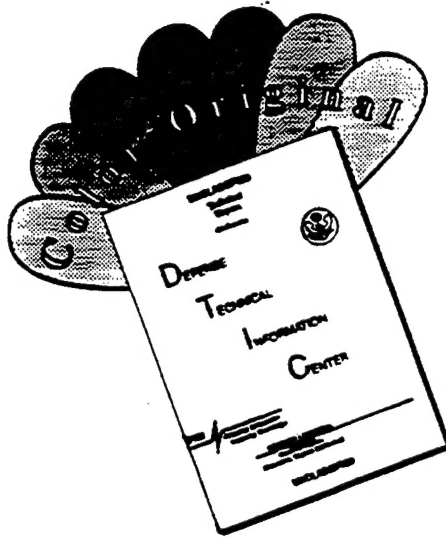
Thesis Advisor:

Anthony A. Atchley

Approved for public release; distribution is unlimited.

19970520 012

DISCLAIMER NOTICE



THIS DOCUMENT IS BEST
QUALITY AVAILABLE. THE COPY
FURNISHED TO DTIC CONTAINED
A SIGNIFICANT NUMBER OF
COLOR PAGES WHICH DO NOT
REPRODUCE LEGIBLY ON BLACK
AND WHITE MICROFICHE.

REPORT DOCUMENTATION PAGE

Form Approved OMB No. 0704-0188

Public reporting burden for this collection of information is estimated to average 1 hour per response, including the time for reviewing instruction, searching existing data sources, gathering and maintaining the data needed, and completing and reviewing the collection of information. Send comments regarding this burden estimate or any other aspect of this collection of information, including suggestions for reducing this burden, to Washington Headquarters Services, Directorate for Information Operations and Reports, 1215 Jefferson Davis Highway, Suite 1204, Arlington, VA 22202-4302, and to the Office of Management and Budget, Paperwork Reduction Project (0704-0188) Washington DC 20503.

1. AGENCY USE ONLY (<i>Leave blank</i>)	2. REPORT DATE	3. REPORT TYPE AND DATES COVERED	
	December 1996.	Master's Thesis	
4. TITLE AND SUBTITLE EVOLUTION OF THE TEMPERATURE PROFILE IN A SIMPLE THERMOACOUSTIC STACK		5. FUNDING NUMBERS	
6. AUTHOR(S) Salindong, Arthur and Hebert, David			
7. PERFORMING ORGANIZATION NAME(S) AND ADDRESS(ES) Naval Postgraduate School Monterey CA 93943-5000		8. PERFORMING ORGANIZATION REPORT NUMBER	
9. SPONSORING/MONITORING AGENCY NAME(S) AND ADDRESS(ES)		10. SPONSORING/MONITORING AGENCY REPORT NUMBER	
11. SUPPLEMENTARY NOTES The views expressed in this thesis are those of the author and do not reflect the official policy or position of the Department of Defense or the U.S. Government.			
12a. DISTRIBUTION/AVAILABILITY STATEMENT Approved for public release; distribution is unlimited.		12b. DISTRIBUTION CODE	
13. ABSTRACT (<i>maximum 200 words</i>) The purpose of this thesis is to provide data on the evolution of the temperature profile in a simple thermoacoustic stack. These measurements are made to support the development of nonlinear time-dependent models of thermoacoustics. An acoustic resonator and driver is used with a five-plate stainless steel stack. The center plate of the stack is instrumented with nine thermocouples, one in the midpoint and four near each end of the plate. The edge thermocouples are located within an acoustic displacement amplitude of one another at high amplitude drive conditions.			
14. SUBJECT TERMS Thermoacoustics; Transient Phenomena; Heat Engine; Resonator; Drive Ratio, Thermocouple		15. NUMBER OF PAGES 135	
		16. PRICE CODE	
17. SECURITY CLASSIFICATION OF REPORT Unclassified	18. SECURITY CLASSIFICATION OF THIS PAGE Unclassified	19. SECURITY CLASSIFICATION OF ABSTRACT Unclassified	20. LIMITATION OF ABSTRACT UL

NSN 7540-01-280-5500

Standard Form 298 (Rev. 2-89)
Prescribed by ANSI Std. Z39-18 298-102

Approved for public release; distribution is unlimited.

**EVOLUTION OF THE TEMPERATURE PROFILE IN A SIMPLE THERMOACOUSTIC
STACK**

Arthur R. Salindong
Lieutenant Commander, United States Navy
B.S., United States Naval Academy, 1982

Submitted in partial fulfillment
of the requirements for the degrees of

**MASTER OF SCIENCE IN PHYSICS
MASTER OF SCIENCE IN ENGINEERING ACOUSTICS**

David D. Hebert
Lieutenant, United States Navy
B.S., United States Naval Academy, 1990

Submitted in partial fulfillment
of the requirements for the degree of

MASTER OF SCIENCE IN APPLIED PHYSICS

from the

NAVAL POSTGRADUATE SCHOOL

December 1996

Authors:

Arthur Raphael Salindong David D. Hebert
Arthur Raphael Salindong David D. Hebert

Approved by:

Anthony A. Atchley Thesis Advisor

Thomas J. Hofler Robert Keolian
Thomas J. Hofler, Coadvisor Robert Keolian, Coadvisor

Anthony A. Atchley, Chairman, Department of Physics

Robert Keolian
Robert Keolian, Chairman, Engineering Acoustics Academic Committee

ABSTRACT

The purpose of this thesis is to provide data on the evolution of the temperature profile in a simple thermoacoustic stack. These measurements are made to support the development of nonlinear time-dependent models of thermoacoustics. An acoustic resonator and driver is used with a five-plate stainless steel stack. The center plate of the stack is instrumented with nine thermocouples, one in the midpoint and four near each end of the plate. The edge thermocouples are located within an acoustic displacement amplitude of one another at high amplitude drive conditions.

Temperature evolution data is recorded for both argon and helium gases at several mean pressures and several drive ratios with the stack located between a pressure node and antinode. This data showed a deviation from linear theory at drive ratios above 1.5%. A crossover of gradient magnitudes is evident during gradient formation with edge thermocouple pairs initially forming larger gradients but dropping in magnitude to less than those of the inner thermocouple pairs after 25-50 seconds. As the gradients approached steady state conditions, they split into two groups of gradient pairs that appeared independent of displacement amplitude. Measurements are also made with the stack positioned in the vicinity of a pressure node and a pressure antinode. This data will be used for future study.

TABLE OF CONTENTS

I. INTRODUCTION.....	1
II. THEORY	3
A. INTRODUCTION	3
B. BASIC PHENOMENA.....	3
C. THERMOACOUSTIC HEATING EFFECTS.....	7
III. EXPERIMENTAL APPARATUS AND PROCEDURE.....	11
A. INTRODUCTION	11
B. EXPERIMENTAL APPARATUS	11
1. Resonator Tube and Acoustic Driver Housing.....	11
2. Stack	16
3. Thermocouple Assembly.....	18
4. Signal Generation, Microphone, and Electronic Instrumentation	21
5. Gas Pressurization and Evacuation System.....	24
C. EXPERIMENTAL PROCEDURE	25
1. Resonator Setup.....	25
2. Evacuation and Fill System.....	25
3. Determining Resonator Characteristics.....	25
4. Data Collection.....	26
IV. OBSERVATIONS, RESULTS, AND DISCUSSION	29
A. RESONATOR TUBE CHARACTERISTICS.....	29
B. RESULTS AND DISCUSSION	30
1. Comparison of Low and High Drive Ratio	30
2. Comparison at Different Mean Pressures.....	36
3. Comparison with Helium	38
4. Measurements at Pressure Node and Pressure Antinode	38
V. CONCLUSIONS AND FUTURE WORK.....	43
A. CONCLUSIONS.....	43
B. FUTURE WORK.....	44
APPENDIX A. LABVIEW	45
A. LABVIEW: OVERVIEW AND SETUP	45
1. Program Pressure_Measure	46
2. Program Plate_Measure	49
APPENDIX B. GRAPHS OF FREQUENCY ANALYSIS OF RESONATOR FOR DIFFERENT GASES AND PRESSURES	56
APPENDIX C: ARGON GAS, 3 PSIA POSITIONED HALFWAY BETWEEN PRESSURE AND VELOCITY NODES	62

APPENDIX D. ARGON AT 5PSI A POSITIONED HALFWAY BETWEEN PRESSURE AND VELOCITY NODES	70
APPENDIX E. ARGON AT 10 PSIA, POSITIONED HALFWAY BETWEEN PRESSURE AND VELOCITY NODES	76
APPENDIX F. ARGON AT 18 PSIA, POSITIONED HALFWAY BETWEEN PRESSURE AND VELOCITY NODES	88
APPENDIX G. ARGON AT 29 PSIA, POSITIONED HALFWAY BETWEEN PRESSURE AND VELOCITY NODES	93
APPENDIX H. HELIUM AT 15 PSIA, POSITIONED HALFWAY BETWEEN PRESSURE AND VELOCITY NODES	95
APPENDIX I: ARGON AT 5 PSIA, VELOCITY NODE.....	101
APPENDIX J: ARGON AT 10 PSIA, VELOCITY NODE	107
APPENDIX K. ARGON AT 10 PSIA, PRESSURE NODE	114
LIST OF REFERENCES	121
DISTRIBUTION LIST	123

ACKNOWLEDGEMENT

First and foremost, I give all glory and honor to God for the strength, wisdom, and patience that He has provided me to endure the academics and the arduous details of research. I would like to express my sincere appreciation and love for my family, my wife Arlene, and my children, Amanda, Andrea, and Alyssa. They have been a constant source of my strength and happiness, and I thank God for this blessing.

I would like to acknowledge my advisor, Dr. Anthony Atchley, whose guidance, encouragement, and inspiration, have taught me more than what could be learned in the classroom. I would also like to thank Gary Beck and George Jashka for their insight and superb machining skills in developing an outstanding apparatus. Finally, I thank Mickey Lin, Ralph Muehleisen, and Robert Wong for their assistance during difficulties experienced throughout this research.

Art Salindong

I owe a sincere expression of thanks to almighty God for leading me first to the Naval Postgraduate School and from there, introducing me to Prof. Atchley and thermoacoustics. My work on this thesis has been the most demanding, but also the most rewarding experience of my postgraduate education, and the skills I have developed have included a lot more than just soldering wires or manipulating acoustic equations. Patience and the ability to troubleshoot problems systematically are two of the more important lessons God has taught me as we grappled with the many setbacks and successes of these experiments together.

None of that could have happened if not for the unrelenting support and tireless dedication shown by my advisor and mentor Prof. Anthony Atchley. I would be remiss if I did not mention how indebted I am for his constant encouragement and continued faith in my ability to succeed.

I would also like to thank Gary Beck and George Jaska of the physics department machine shop. The experiment could never have taken place had they not been so diligent and rapid in building our apparatus. Similarly, I need to thank Robert Wong for helping us with any computing difficulties that arose, and Mary Atchley for teaching me how to use various pieces of test equipment and supplying us with all the unusual tools required to finish this project.

Most of all I need to thank God for my wife, Dawn. A constant source of love and strength, she made my success her goal, tirelessly championing my cause. I could have never found this work so enjoyable if she had not put her whole heart and soul behind supporting me.

Dave Hebert

I. INTRODUCTION

The first observation of a thermoacoustic phenomenon was reported over 100 years ago. Active research began in the 1970's and early 1980's. The technology and practical applications have matured significantly over the last decade. Many studies have been conducted at several institutions including Los Alamos National and the Naval Postgraduate School. At this point, the efficiencies and coefficients of performances of thermoacoustic devices continue to improve but are still less than those of conventional heat engines. Linear steady state models of thermoacoustic engines have been developed, and accurately predict engine performance in the appropriate parameter range. Because the cooling power of thermoacoustic engines is nominally proportional to the square of the drive ratio (ratio of acoustic pressure amplitude to mean gas pressure), one route to high power devices is to increase the drive ratio. However, doing so quickly takes one out of the linear regime. In fact, experiments have shown serious discrepancy between measured and predicted performance at high drive ratios [Ref. 1]

Recent work by Prosperetti [Ref. 2], Knio [Ref. 3], and others is directed toward developing nonlinear time-dependent models of thermoacoustics. These models are capable of treating only the simplest engine geometry. Because most published data are from practical devices, there is a shortage of data with which to test these new models.

The purpose of this thesis is to provide data on the evolution of the temperature profile in a simple thermoacoustic stack. The center plate of a five-plate stack is instrumented with nine thermocouples, one in the midpoint and four near each end of the plate. The four edge thermocouples are located within an acoustic displacement amplitude of one another at high amplitude drive conditions.

The outputs of the thermocouples are recorded as functions of time prior to and after application of a high amplitude standing wave. The sound field is applied long enough for the temperature differences to reach steady state. Temperature evolution data is recorded for both argon and helium gases at several mean pressures and several drive ratios. This work extends the measurements of Wheatley, et. al. [Refs. 4,5] and other researchers at the Naval Postgraduate School [Ref. 1].

A theoretical discussion as well as derivation of important parameters will be covered in the Chapter II. Chapter III is a description of the experimental apparatus including the acoustic resonator and all peripheral equipment. In addition, a detailed discussion of the data collection procedure will be covered. Chapter IV is an analysis of the data obtained during temperature evolution measurements. Chapter V will list the summary of findings and recommendations for future work. Appendices include a detailed description of the data acquisition software LabVIEW as well as data for all measurements made.

II. THEORY

A. INTRODUCTION

When considering the presence of a sound wave within a gas, one acknowledges the existence of coupled pressure and displacement oscillations. The presence of temperature oscillations, however, is a phenomenon often overlooked, but almost always accompanies pressure oscillations. The combination of all of these oscillations, and their interactions with solid boundaries, give rise to thermoacoustic heat transport. Thermoacoustic devices exploit this process to convert sound to a heat flow (a refrigerator) or heat into sound (a prime mover). A basic description of this process follows.

B. BASIC PHENOMENA

To illustrate the basic principles of thermoacoustic engines more clearly, this section discusses a simple example where the acoustic and thermodynamic effects are nearly distinct. In addition, a Lagrangian point of view will be used to better observe the effects of a standing wave and the resulting heat transport to a solid boundary.

Consider a fluid (gas or liquid) supporting an acoustic plane standing wave in the presence of a single solid plate aligned parallel to the direction of oscillation. The presence of the plate causes two important effects: (1) a time-averaged heat flux near the surface of the plate, along the direction of acoustic oscillation, and (2) the generation or absorption of real acoustic power (work) near the surface of the plate [Ref. 6]. These two effects, produced by the interaction between sound wave and solid boundary, are the result of the time phase difference between temperature and displacement and is the basis of all thermoacoustic engine phenomena. The introduction of this second thermodynamic medium, a single or small stack of plates, stimulates a hydrodynamic entropy flow where the resulting phase difference is due to the natural irreversible process of thermal conduction [Refs. 6,7].

It is important to understand the relevant length scales when discussing the heat transport process. Most thermoacoustic engines and heat pumps have a steady or pure tone oscillation such that velocity, pressure, and temperature essentially vary sinusoidally with time at the oscillating frequency f . The wavelength $\lambda=a/f$ where a is the sound speed, is an important length scale, especially in the direction of the gas displacement oscillations. Most thermoacoustic devices have wavelengths where $10\text{ cm} \leq \lambda \leq 10\text{ m}$ and the lengths of the stacks or plates are very much less than λ [Ref. 7].

In the directions perpendicular to the displacement oscillations, the key length parameters are the thermal penetration depth δ_κ and viscous penetration depth δ_v . These parameters determine the nature of thermal contact between the plate and a typical parcel of gas. The thermal penetration depth is approximately the distance that heat can diffuse through the gas in the time $1/\pi f$ and can be described by

$$\delta_\kappa = \sqrt{\frac{\kappa}{\pi f \rho c_p}},$$

where κ is the thermal conductivity of the gas, ρ is the density, and c_p is its isobaric heat capacity per unit mass. Gas that is several δ_κ from the nearest solid surface will experience adiabatic oscillations, and will not participate in thermoacoustic heat transport. Gas that is very much closer to the solid boundary than δ_κ experience isothermal oscillations, and will not participate either. The viscous penetration depth, which is closely related to the thermal penetration depth, is approximately the distance over which momentum can diffuse in a time $1/\pi f$ and can be described by

$$\delta_v = \sqrt{\frac{\mu}{\pi f \rho}} = \sqrt{\frac{\nu}{\pi f}},$$

where μ is viscosity and ν is the kinematic viscosity. Gas within δ_v of the solid surface, will have viscous shear and as a result gradients will develop in the oscillatory velocity

and displacement, leading to energy dissipation. The ratio $\frac{\delta_v}{\delta_\kappa} = \sqrt{\frac{\mu c_p}{\kappa}}$ is the square root of the Prandtl number, a dimensionless measure of the ratio of viscous to thermal effects, and is of order 1 for ideal gases.

In describing the phenomena of thermoacoustic prime movers and heat pumps, we will use the limit of zero Prandtl number σ , so that viscous penetration depth δ_v is negligible and the fluid flows like a plug, slipping along the boundary of a solid surface. Additionally, we will assume that the acoustic cycle of pressure or particle displacement is represented by a square waveform rather than the usual sinusoid. Imagine a single short plate, shown in Figure 2-1, inserted into the end of an acoustic resonator, where the plate is short compared both with its distance from the closed end and the radian wavelength $\lambda = \lambda/2\pi$, and long when compared to the acoustic displacement amplitude. The plate has a high effective heat capacity per unit area and uniform temperature throughout. An acoustic standing wave exists in the resonator, which is generated by a driver at the other end of the tube (not shown) and a pressure antinode exists at the rigid end.

Rigid Closed Resonator Tube

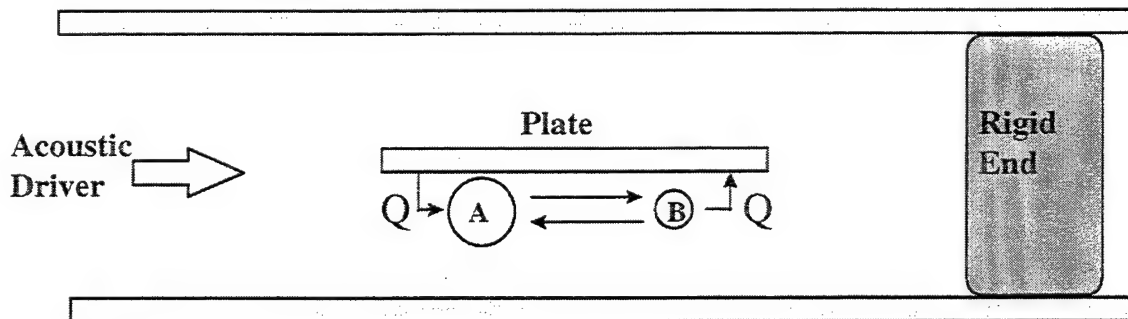


Figure 2-1. Simplified diagram of thermoacoustic heat transport near the center of the plate.

We will describe what happens thermally to a parcel of gas [Refs. 4,8]. This parcel is located about a thermal penetration depth δ_k from the plate and, as a consequence of the pressure fluctuations, oscillates along the plate. Consider the parcel located below the plate at position A. As it moves to position B, there is no time for heat flow, so that its entropy remains constant and thus, adiabatic. But at B, the pressure is

increased and the temperature increased by the adiabatic amount $T_i = \left(\frac{T_m \beta}{\rho_m c_p} \right) p_i$, where

the subscript m denotes mean values and β is the isobaric expansion coefficient. As the

gas at B is now hotter than the plate and close enough to the plate for heat to transfer to it, heat Q passes from the parcel to the plate, thereby decreasing the entropy of the parcel by some amount ΔS . The gas parcel is then pushed to the left from B to A during the expansion phase, which again is adiabatic and so the entropy carried to the left is diminished by ΔS . The gas pressure is reduced at A, so the temperature is now reduced below that of the plate by the adiabatic amount. Hence, heat Q flows into the parcel from the plate, thereby increasing the entropy of the parcel by approximately ΔS . ("Approximately" because $\Delta S = Q/T$ and the T is slightly different in the two cases.) Hence, in one complete cycle entropy $\approx 2\Delta S$ has been carried from left to right. The same conclusion holds for all parcels along the plate which, like A, are in contact with the plate at each end of the stroke. Except near the ends, if one parcel adds heat Q to one piece of the plate during one part of a cycle, another parcel will remove that same amount of heat from the same piece during another part of the cycle. Therefore, the average thermal condition of the plate remains unchanged while entropy flows, on the average, hydrodynamically along the plate in the fluid, within a lateral distance of order δ_k from the plate, toward the pressure antinode.

At the ends, where the symmetry of the heat transfer is broken, the physics is a bit different. Consider the parcel C at the left of the end of the plate in Figure 2-2.

Rigid Closed Resonator Tube

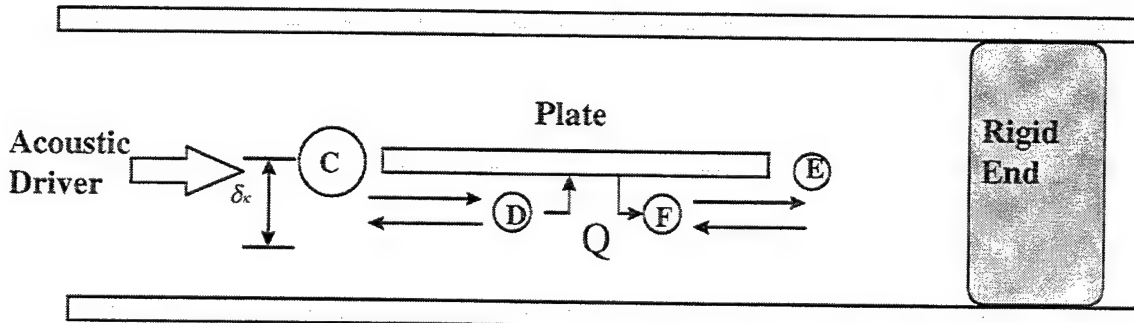


Figure 2-2. Simplified diagram of thermoacoustic heat transport near the ends of the plate.

Its trajectory moves in and out of thermal contact with the plate. In the compressed state at D, it is in thermal contact with the left end of the plate, but when it expands back to C, it loses thermal contact and simply remains cold. On compression from C to D, there is

an adiabatic temperature increase, but in steady state this just increases the temperature back up to the temperature of the left end of the plate. Therefore, the gas to the left of the end of the plate will have a lower temperature than the adjacent plate by the fluid's adiabatic temperature difference. Parcel C plays no role in the average heat flow while parcels to the right, like A described above, have an uncompensated heat extraction effect. As a consequence there is a net heat extraction from the left end of the plate. Note that while T_1 may be small, so is δ_k and so the temperature gradient for this diffusive heat transfer can be substantial.

Similarly, a parcel E to the right of the right end of the plate will have its trajectory move in and out of thermal contact with the plate moving from position E to F and vice versa. This motion again is essentially adiabatic. The parcel at F has the same temperature as the right end of the plate while, when at E, there is no thermal contact. In the compressed state, the gas to the right of the right end of the plate is hotter than that end by the adiabatic temperature difference. Parcel F plays no role in the average heat transfer at the right end. If the plate is made of a highly thermally conducting material, very little temperature difference will occur across the plate. For the case of this thesis, only plates of poor thermal conductivity/high heat capacity will be considered.

C. THERMOACOUSTIC HEATING EFFECTS

We now turn our attention to the cooling and heating effects at the ends of the stack by describing experiments with a very short stack that we call a thermoacoustic couple. Subsequent analysis will show that the cooling and heating occur because application of acoustic power by the driver causes an average flow of entropy out of the end of the stack closer to the pressure node, down along the thermal boundary layer in the gas, and into the end of the stack closer to the pressure antinode as depicted in Figure 2-3. The derivation of the steady state temperature difference was first presented by Wheatley et.al. [Ref. 5]. It is only approximate and contains a number of limiting assumptions. Nonetheless it serves as a reasonable starting point from which to understand the important parameters.

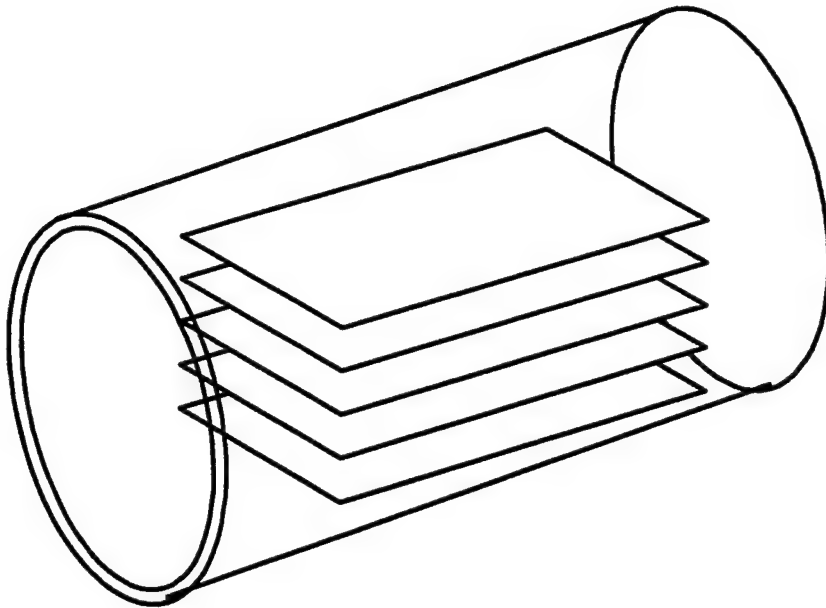


Figure 2-3. Schematic showing the geometry of a stack of parallel plates near the closed end of an acoustic engine.

This stack of plates can be used to demonstrate the dramatic cooling and heating effects central to thermoacoustic phenomena. Furthermore, all phenomena can be described by observation of a single short plate. If the stack had been placed at either a pressure or velocity antinode, then the output of the couple is zero. Elsewhere the end of the couple toward the nearest pressure antinode is always hotter.

To understand the couple and how the evolution of a temperature gradient occurs, note that the work flow over the entire tube cross section is continuous and slowly varying at both the entrance and the exit of the couple. For a solid plate of length ΔX , width $\Pi/2$, and negligible thickness, heat can be transported along X by the hydrodynamic transport of entropy, carried by the oscillatory velocity u_1 . The time-averaged longitudinal energy flow in the gas is the same as the time-averaged longitudinal enthalpy flow [Ref 5]:

$$\bar{H} = \Pi \int dy (\bar{\rho} u h)$$

where Π is the surface area per unit length, or the perimeter of the stack, ρ is the gas density, u is the longitudinal component of the gas velocity, h is the gas enthalpy per unit mass, y is the transverse dimension in the gas, and the integral is taken over the entire

tube cross section [Ref. 5]. The time average is indicated by a bar. When corrected to second order this equation can be divided in both a heat flow and a work flow with

$$\bar{H} = \bar{Q} + \bar{W}$$

where $\bar{Q} = \Pi \int dy \overline{(\rho_m c_p T_1 - p_1) u_1}$ and $\bar{W} = \Pi \int dy \overline{p_1 u_1}$. The m subscript denotes mean values, p_1 and u_1 are the first-order pressure and x-velocity, and c_p is the specific heat capacity.

\bar{Q} is responsible for the temperature differences observed in the couple and can be quite large compared to \bar{W} if we assume a short stack approximation. The computation of \bar{Q} can be further refined if first-order sinusoidally time varying quantities are used as well as assuming a lossless resonator tube. Now

$$\bar{Q} = -\frac{\Pi}{4} \frac{\omega P_0^2}{\rho_m} \delta_k \left[\frac{1+\sqrt{\sigma}}{1+\sigma} \left(\frac{a}{2\omega} \right) \sin \frac{2\omega x}{a} + 2 \frac{1-\sigma\sqrt{\sigma}}{1-\sigma^2} \frac{\theta}{\gamma-1} \left(\frac{a}{2\omega} \right)^2 \left(1 - \cos \frac{2\omega x}{a} \right) \right]$$

where the first term represents the heat flow in absence of a longitudinal temperature gradient, and the second gives the modification caused by a temperature gradient [Ref. 5]. Near $x=0$ the sign of \bar{Q} is negative which means that the average heat flow in the gas due to the dynamic entropy flow is toward the closed end. In general this heat flow is directed toward the nearest pressure antinode and away from the pressure node.

If the internal thermal conductance of the couple is sufficiently high, then in dynamic equilibrium for each point x along the couple

$$\bar{Q} - KA \frac{dT}{dx} = 0,$$

where KA is the effective product of diffusive thermal conductivity and cross-sectional area of the couple [Ref. 5]. This assumes that the heat transferred via entropy flow in the gas is returned by diffusive conduction in the solid. To solve for dT/dx , the expression for \bar{Q} previously derived is inserted then integrated with respect to x over the length $\Delta x = L$ of the couple for $\Delta T \equiv T_H - T_C$. Hence

$$\Delta T \equiv \frac{\frac{1}{4} P_0^2 \delta_k (1 + \sigma^{1/2})}{\rho_m c \left(\frac{Kd_2}{L} \right) (1 + \sigma)} \sin \frac{2\omega}{c} \bar{x}$$

$$\frac{1 + P_0^2 \delta_k (1 - \sigma^{3/2})}{\left(4 \left(\frac{\kappa d_2}{L} \right) \rho_m L T_m \omega (\gamma - 1) (1 - \sigma^2) \right)} \left(1 - \cos \frac{2\omega \bar{x}}{c} \right)$$

were ΔT is the temperature difference across the plate, P_0 is the peak acoustic pressure of the driver, δ_k is the thermal penetration depth, σ is the Prandtl number of the gas, γ is the specific heat ratio of the gas, L is the plate length, T_m is the mean ambient temperature, ρ_m is the mean density of the gas, c is the sound velocity in the gas, ω is the angular frequency, x is center of the couple position measured from the rigid end of the resonator, κ is the thermal conductivity, and d_2 is the thickness of the plate [Ref. 5].

One can notice that the temperature difference depends upon many parameters, including P_0^2 , plate position, gas type, and mean pressure. Previous work has shown that the measured ΔT are significantly less than that predicted by this simple expression [Refs. 1,5]. However the functional dependence is representative.

We choose three positions for our stack in the resonator: 1) half way between a pressure node and an anti-node, where simple theory says ΔT should peak at low drive ratios, 2) at a pressure node, where only viscous losses should be important, and 3) at a pressure antinode where only thermal losses should be important.

III. EXPERIMENTAL APPARATUS AND PROCEDURE

A. INTRODUCTION

A description of the experimental apparatus and the procedures for data acquisition are presented in this chapter. The first section will include a description of the resonator tube and driver housing assembly, the 5-plate stainless steel stack, the thermocouple assembly, the microphone and electronic instrumentation, and the evacuation/fill system. The second section discusses the LabVIEW based data acquisition system. The third and final section is a detailed discussion of the experimental procedure.

B. EXPERIMENTAL APPARATUS

1. Resonator Tube and Acoustic Driver Housing

Figure 3-1 is an illustration of the resonator tube and acoustic driver housing. When considering the material selection for this resonator, several factors came to mind. Pressure tightness with the ability to sustain up to three atmospheres pressure, machining capability for ease of fabrication, and the ability to disassemble the system to adjust stack positioning and frequency, were the three factors that led to the selection of Schedule 40 PVC (Polyvinyl chloride). Clear PVC was used and allowed visual sighting of both the stack positioning as well as the rigid end within the resonator.

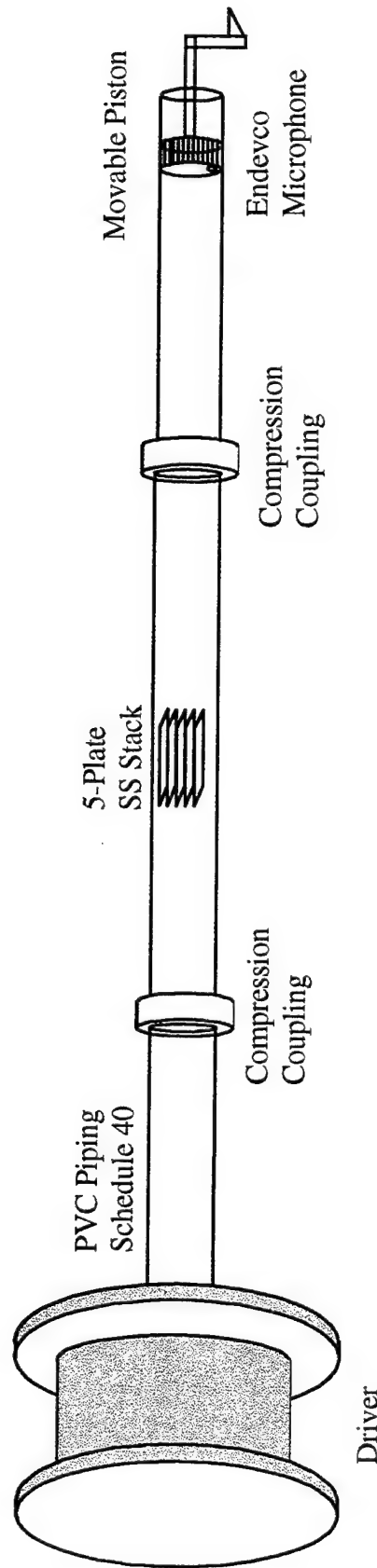


Figure 3-1. Illustration of acoustic resonator and driver housing.

The standing wave was generated with a 10-inch woofer located within the driver pressure housing. The driver housing is an aluminum cylinder with an 11 inch outer diameter, capped at both open ends with a 1-inch thick aluminum plate. The two plates were bolted together with eight $\frac{1}{2}$ inch threaded rods and nuts. The cylinder is 14.5 cm long with a 25.4 cm inside diameter with a 1.27 cm wall thickness. Internal pressure within the housing is monitored by an OMEGA Engineering general service dial pressure gauge mounted on the back end plate. A 150 psi relief valve is installed on the forward end plate.

The acoustic driver used to generate the standing wave is a Peerless CSX-257SWR-39115 10-inch Woofer. With 220 W nominal power capacity and a 9.0 mm excursion, it provided sufficient amplitude to obtain standing waves with drive ratios ranging up to 6% in air at 87 Hz. A Hewlett Packard 33120A function generator was used to provide input waveforms via a Techron 7520 power amplifier with amphenol isolated bulkhead jack connections established on the back plate.

Figure 3-2 is a cross-sectional view of the driver housing and driver. The driver is secured to the housing with screws in four of the eight holes provided in the mounting ring. The remaining four holes served as a flow path to allow pressure equalization across the driver during pressure changes. The front of the driver is approximately 3.5 cm from the inside surface of the 1 inch thick plate.

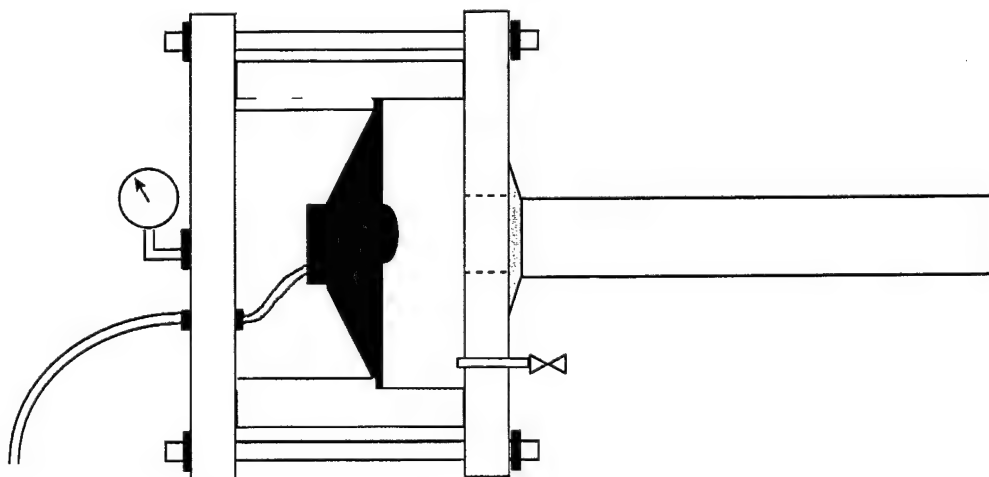


Figure 3-2. Cross-sectional view of the driver and driver housing.

The driver housing is bolted via a galvanized steel threaded flange to the end of the resonator tube. The resonator tube is approximately 3 meters in length with a 5.08 cm inner diameter. Although the greater compliance of PVC piping in comparison to that of metal tubing, resulted in lower quality factors than might be achieved with a thick walled metal pipe, its ease of machining and assembly outweighed this disadvantage. A movable 3 cm plastic piston plug, as seen in Figure 3-3, served as the rigid end of the resonator tube. The variable positioning of the end allowed slight changes in resonance frequency and served to fine tune stack position. This plug maintained system pressure integrity through the use of o-rings and an aluminum block assembly that fit snugly about the outer tube at the plug. An ENDEVCO piezoresistive pressure transducer (Model #8510C-50) that was used to monitor pressure within the resonator, was also mounted in the plug. The microphone was situated such that its protective screen face was flush with the inside surface of the plug.

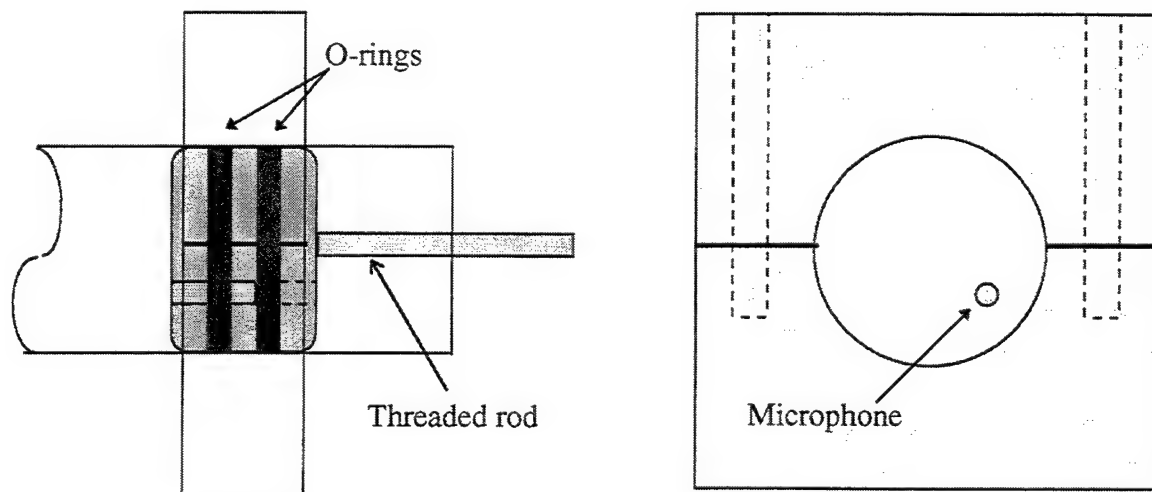


Figure 3-3. Side and front view of rigid end and aluminum block assembly

The desire to put the stack at three different locations dictated the need for sectioning of the resonator. The tube was configured with one section that would permanently contain the stack and thermoacoustic couples. Other various length sections were then coupled to the stack section to maintain consistent overall tube dimensions. The three configurations utilized in this experiment are depicted below in Figure 3-4.

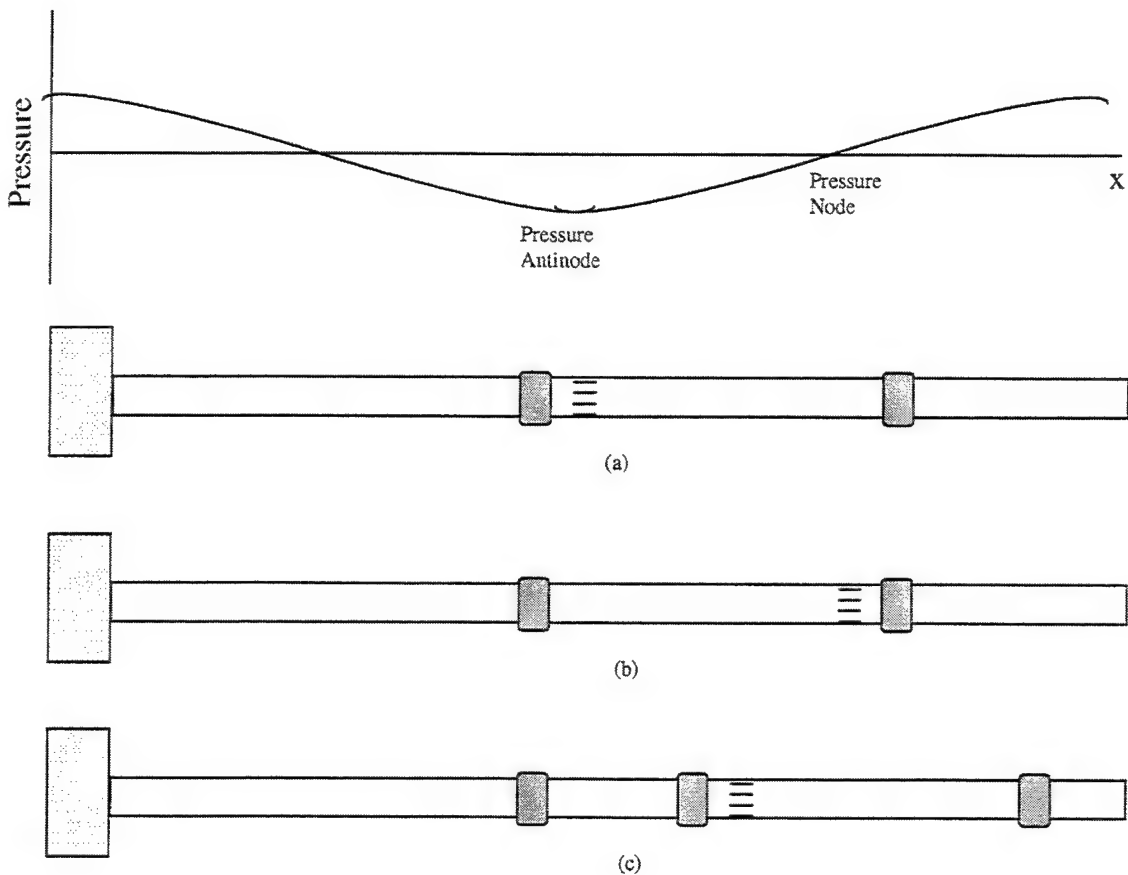


Figure 3-4. Three positions of the stack inside the resonator tube. (a) stack at the PAN (Pressure Antinode). (b) stack at PN (Pressure Node) and (c) stack at a position half way between PAN and PN.

As seen in this figure, the desired stack positions are at the pressure antinode, pressure node, and a position halfway between. The stack section is constructed such that the center of the stack is 6.00 inches from the end. This facilitated routing of thermocouple wires through small holes drilled in the tube directly adjacent the stack. The holes are sealed with epoxy to maintain pressure tightness.

Individual sections of PVC piping are held together with PVC compression couplings and reinforced with aluminum restraining blocks on either end. The compression couplings are designed for 450 psi liquid and contain rubber gaskets that generate a friction seal between tube and coupling. The aluminum restraining blocks are similarly constructed as the rigid end aluminum block assembly except that two blocks

are used on each coupling connected by threaded steel rods. The coupling assembly is shown in Figure 3-5.

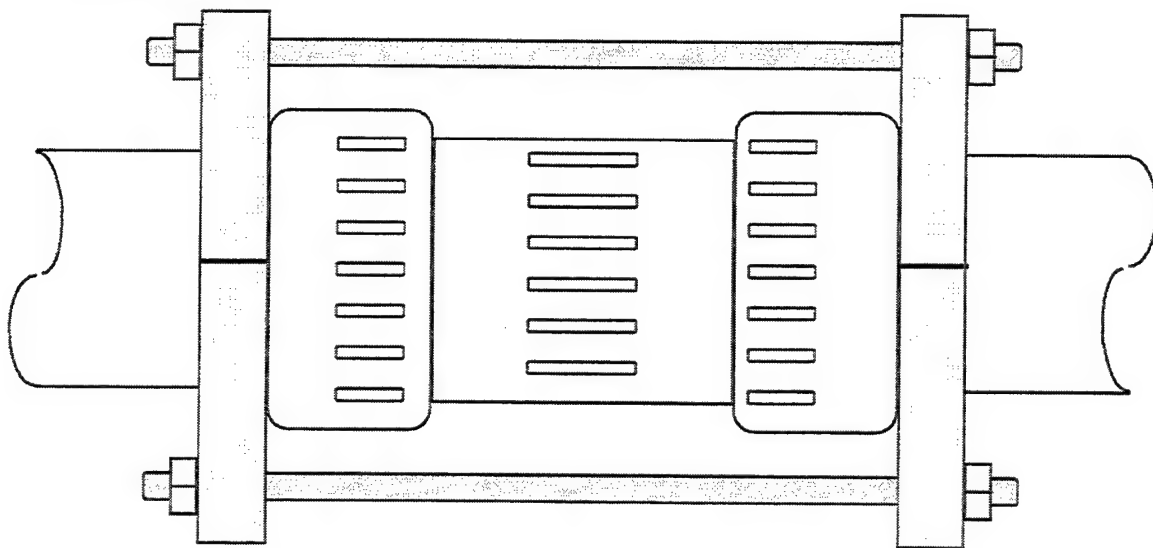


Figure 3-5. Resonator tube compression coupling and aluminum restraining block assembly.

2. Stack

As seen in Figure 3-6, the stack, is made up of five Type 304 Stainless Steel plates, 69.55 mm long, 51.4 mm wide, and 0.277 mm thick. Four 5/16 inch 0.18 tpi bolts and nuts are used to maintain the stack with plastic washers to establish a 2.46 mm separation between plates. This separation was predetermined to account for 2-4 thermal penetration depths between plates using various gases at varying pressure parameters. Thermocouples were attached on the top face of center plate. This face is coated with an acrylic spray to electrically isolate the plate from the thermocouples. Nine type E, chromel-constantan thermocouples were situated and secured to the plate with a clear laminate. An actual photograph of the stack can be seen in Image 3-1.

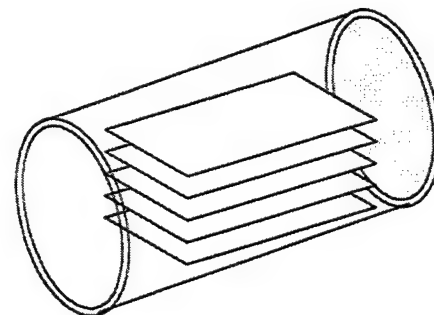
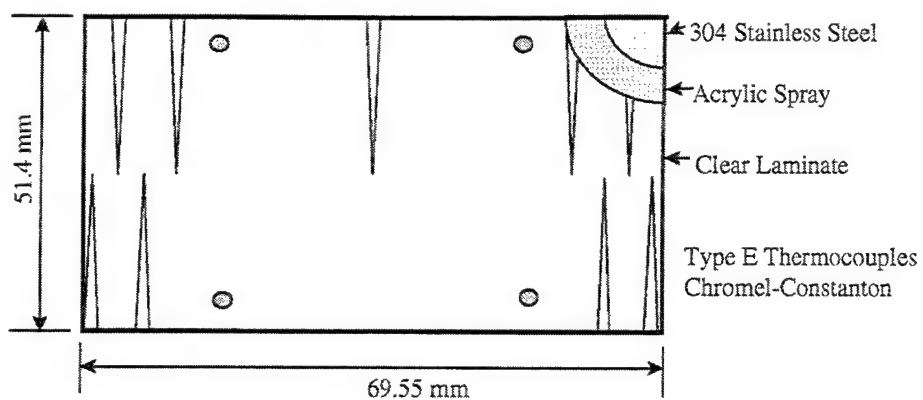


Figure 3-6. Stack geometry and thermocouple placement.

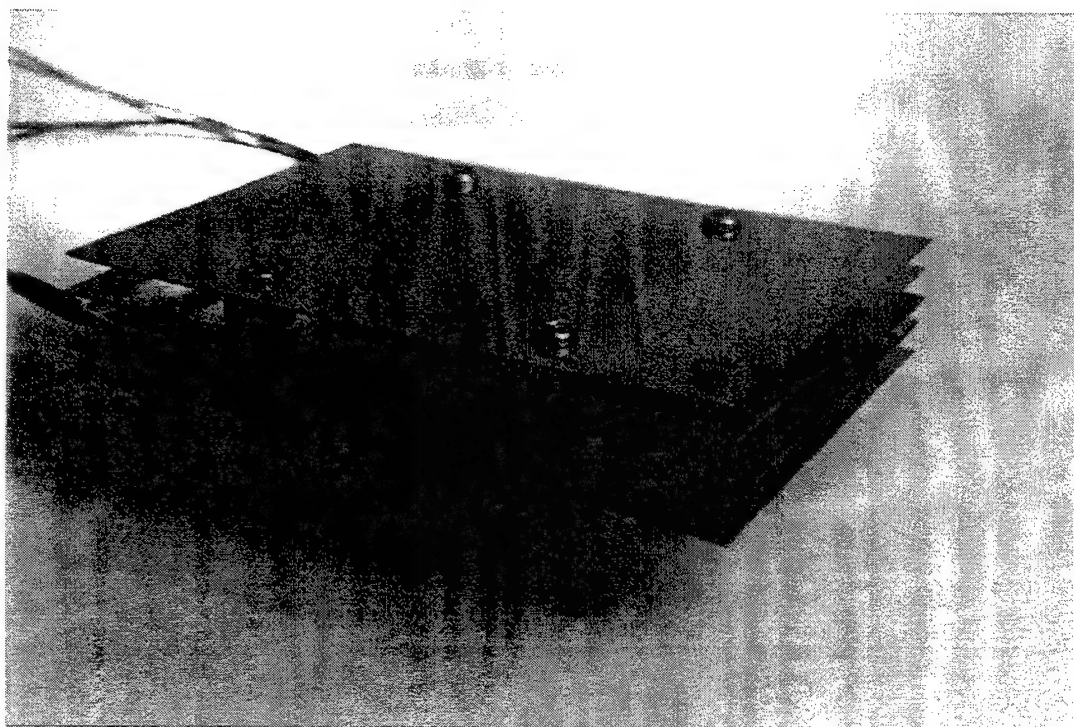


Image 3-1. Photo of Stack

3. Thermocouple Assembly

Omega type E chromel-constantan 0.002 inch diameter thermocouples (catalog number CHCO-002) are used to sense plate temperature. The basis of thermocouple operation relies on the voltage generated when two dissimilar metals are placed in contact with each other. This voltage is linearly proportional to the temperature over a modest temperature range and is sensed directly at the tip of the junction. The tips of all thermocouples are positioned along the plate's centerline. The conversion factor which relates this generated voltage to temperature is known as the Seebeck coefficient. For type E thermocouples at room temperature, the Seebeck coefficient is approximately 58.5 $\mu\text{V}/^\circ\text{C}$ [Ref. 10]. This coefficient is obtained from the reference tables of the *Omega Complete Temperature Measurement Handbook and Encyclopedia* (see appendix A for complete explanation of source for this constant). Type E was chosen over other types since they provide the greatest sensitivity (in $\text{V}/^\circ\text{C}$).

Image 3-2 is a photograph of the center plate. As seen in both Figure 3-6 and Image 3-2, four thermocouples were placed at either end of the center plate with a ninth thermocouple to sense the center temperature. Thermocouples at the ends were spaced 3 mm apart. This spacing corresponds to an acoustic displacement amplitude for atmospheric pressure air at a drive ratio of 1 percent. Thus, with four thermocouples placed at the ends, any acoustic displacement amplitude dependent effects could be monitored up to a drive ratio of 3 percent. Table 1 shows the locations of each thermocouple measured from the edge of the plate.

Thermocouple	Position (mm)
1	1.08
2	4.71
3	8.52
4	11.61
5	34.37
6	59.54

7	62.68
8	65.97
9	68.40

Table 1. Thermocouple position along plate centerline.

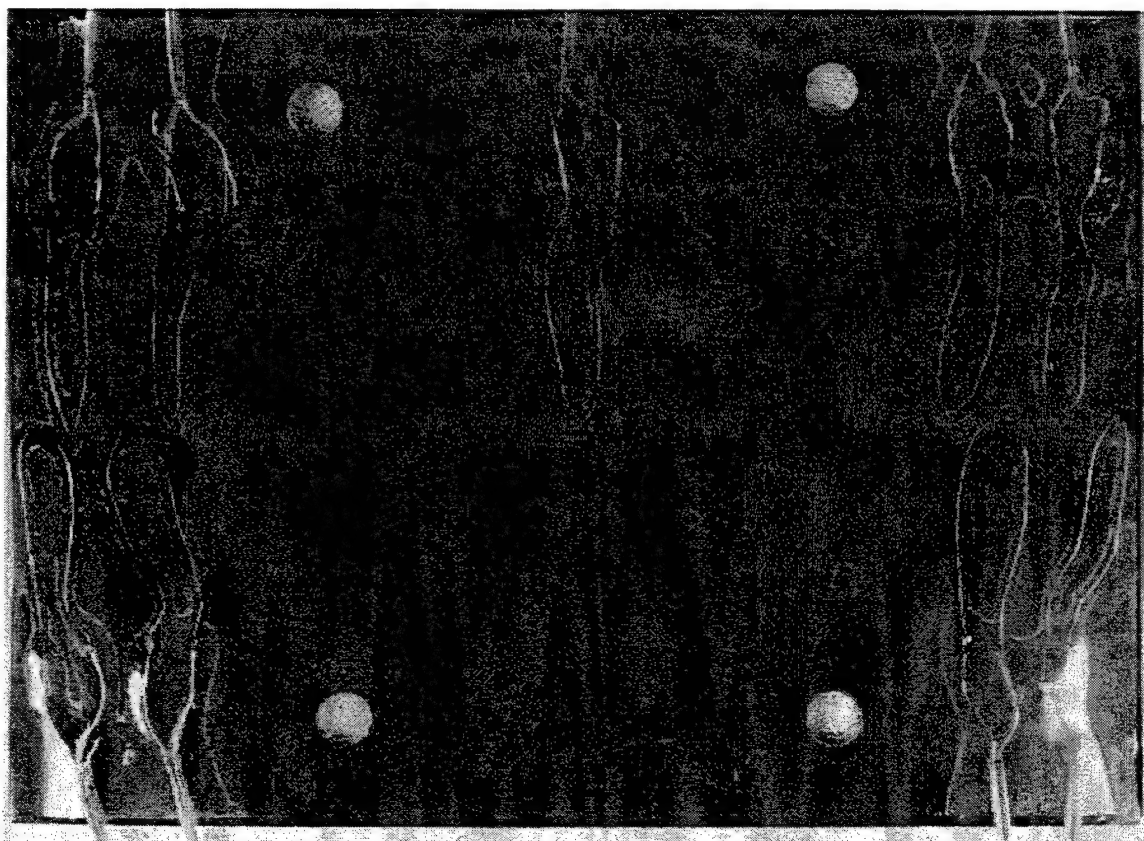


Image 3-2. Thermocouple placement on the center plate

Along with the nine thermocouples placed on the plate, three other type E thermocouples were attached to the resonator wall. Two were attached at the points on the wall corresponding to the forward and aft edge of the stack. The last one was fixed to the wall at the center of the stack. The center thermocouple was monitored using a hand held Omega type E thermocouple thermometer, and was used to provide an indication of resonator temperature (T_{wall}). The other two were monitored with the nine bare thermocouples on the plate as described below.

The nine bare thermocouple leads were run to the edge of the plate as shown in Image 3-2. The leads were then soldered to insulated 0.005 inch type E duplex thermocouple wires to provide a stronger transition as the wires leave the plate. These wires were routed along the plate edge and individually threaded through small holes in the resonator wall immediately adjacent the stack end. These holes were sealed using epoxy to ensure pressure integrity could be maintained within the resonator. The ends of these thermocouple wires and the two from the resonator wall were fitted with type E subminiature connectors that interfaced with an isothermal block.

The isothermal block assembly is displayed in Figure 3-7. This assembly consists of a 2.5 inch by 4.5 inch aluminum block, 0.75 inches thick. The block is housed within an aluminum box. The thermocouple wires are soldered to stranded copper wires. The soldered junctions are placed in thermal contact with the aluminum block. Thin laminate between the soldered junctions and the block prevented electrical contact. The isothermal block serves to hold all the junctions at the same temperature preventing the creation of secondary thermoelectric voltages. The temperature of the isothermal block can be monitored using a thermocouple attached thermally to the block with a hand held Omega 450 AET Type E Thermocouple Thermometer. The copper wires are bundled and routed to a 37-pin ribbon cable connector. The aluminum casing is secured and filled with polyester fiber to provide additional thermal insulation.

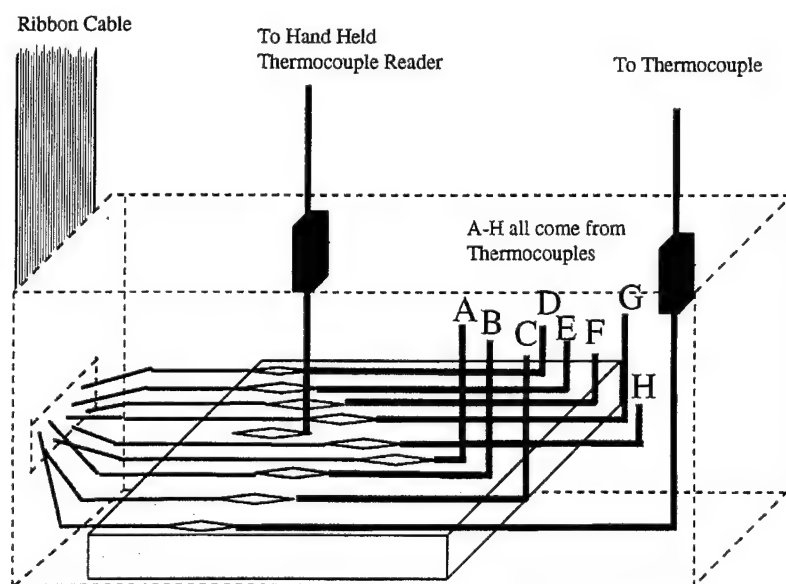


Figure 3-7. Isothermal Block Assembly

4. Signal Generation, Microphone, and Electronic Instrumentation

Figure 3-8 is a block diagram of the electronic instrumentation used during measurements. A Hewlett Packard 33120A, 15 MHz Function/Arbitrary Waveform Generator is used to generate a sinusoidal signal that is amplified by a Techron 7520 power supply amplifier and provided as the input signal to the driver. The amplified signal level is monitored with a Hewlett Packard 3478A multimeter to prevent exceeding power rating of the driver. The function generator signal is monitored on a Tektronics 2336 Oscilloscope.

Both static and dynamic pressure within the resonator are monitored with an ENDEVCO piezoresistive pressure transducer (Model # 8510C-50, Serial # 10019), or microphone. The sensitivity of the microphone is 3.12 millivolt per psi at 10V excitation with a linear range of 50 psi. Static and dynamic pressure is thus sensed in the form of DC and AC voltages which are amplified with a custom made amplifier. Once amplified, the microphone signal is monitored on the oscilloscope and a second multimeter. A Hewlett Packard 33665A Dynamic Signal Analyzer, which is discussed more in the Experimental Procedure section, was used to determine the resonant frequency and quality factors of the resonator.

The thermocouples are routed to the computer via the Isothermal Block assembly, a 37 pin ribbon cable, an I/O block assembly, and finally a 50-pin shielded ribbon cable leading to the data acquisition boards within the computer. The I/O connector block assembly is an aluminum housing containing two I/O connector blocks each containing 50 screw terminals. Specific leads from the 37-pin cable were separately secured to a screw terminal to allow a differential input to the data acquisition board. Thus each thermocouple utilized two leads that provided one channel of temperature information. Each I/O connector block had eight channels available for temperature data, thus 16 channels were available. Since nine thermocouples are used for sensing plate temperature, and two thermocouples are used for wall temperatures, only eleven channels

are needed. Two 50-pin shielded ribbon cables are needed to connect from the I/O block assemblies to two data acquisition boards.

The data acquisition (DAQ) boards acquire thermocouple voltages and record them for use with various software packages. The two DAQ boards used were the National Instruments NB-MIO-16X and the NB-MIO-16XL boards, both for use with Macintosh NuBus equipped computers. The NB-MIO-16X and XL boards are high performance multifunction, digital and analog, input/output boards. They can handle up to 16 single ended voltage inputs or 8 differential voltage inputs. The 16 bit analog/digital converter (ADC) sampling rate is 55 kS/s with programmable gains of 1, 10, 100, or 500. The onboard voltage reference can be set at 5 or 10 volts. Throughout the experiment, a gain of 100 and voltage reference of 10V was used. This gave an overall precision of $3.05 \mu\text{V}$, meaning the value of the least significant bit of the 16 bit ADC is $3.05 \mu\text{V}$. Since the Seebeck coefficient is $58.5 \mu\text{V}/^\circ\text{C}$, the precision in degrees amounts to approximately 0.05°C . The data acquisition software and procedure will be discussed in more detail in the following section.

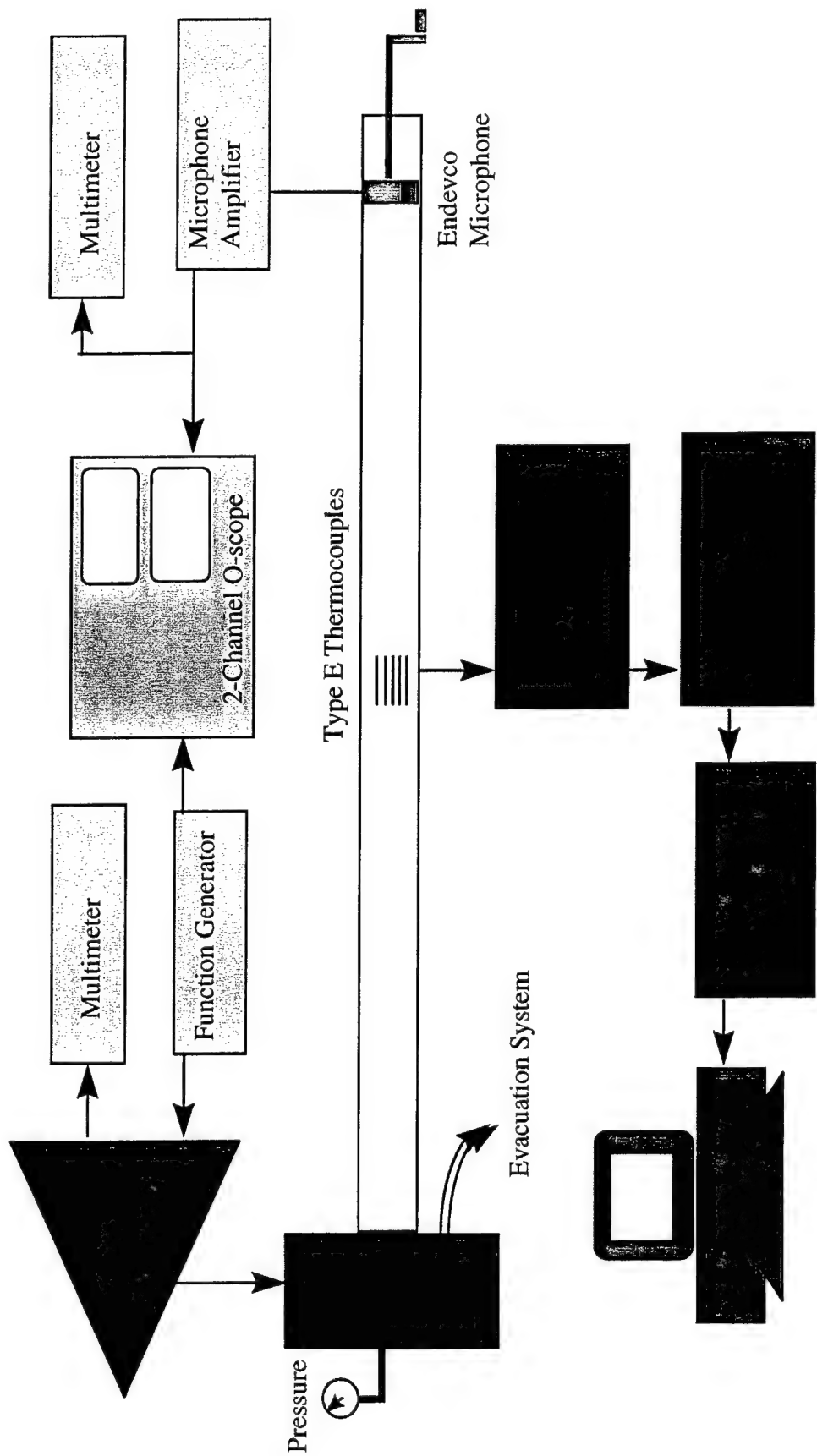


Figure 3-8. Block Diagram of Instrumentation Setup

5. Gas Pressurization and Evacuation System

Figure 3-9 depicts the pressurization system and evacuation system used to change gases and vary mean pressure within the driver housing and resonator tube. Pressure evacuation, is accomplished with a Duo-Seal Vacuum Pump. Pressurized gas cylinders with pressure regulators are used to fill and pressurize the system. Flow into the resonator housing is controlled by throttling one of two valves between the regulator and driver housing. Once pressure is established, all valves are closed and pressure is maintained by a two-valve isolation as well as the pressure integrity of the driver housing and resonator tube. Within the driver housing, pressure or vacuum was equalized on both sides of the speaker face by open screw holes in the mounting rim. No attempts are made to regulate the pressure automatically during data recording. The gas cylinders are interchangeable allowing the use of Argon, Helium, Nitrogen and other gases.

Gas leak rates were measured using a program called Pressure_Measure.VI. This program measured and recorded the mean pressure within the resonator as sensed by the Endevco microphone. Leak rates were measured over 20 minute intervals to ensure mean pressure would remain constant throughout length of any individual data run. The measured leak rate of Helium gas averaged over many 20 minute spans was approximately 0.004 psi lost per minute at 45 psia mean pressure.

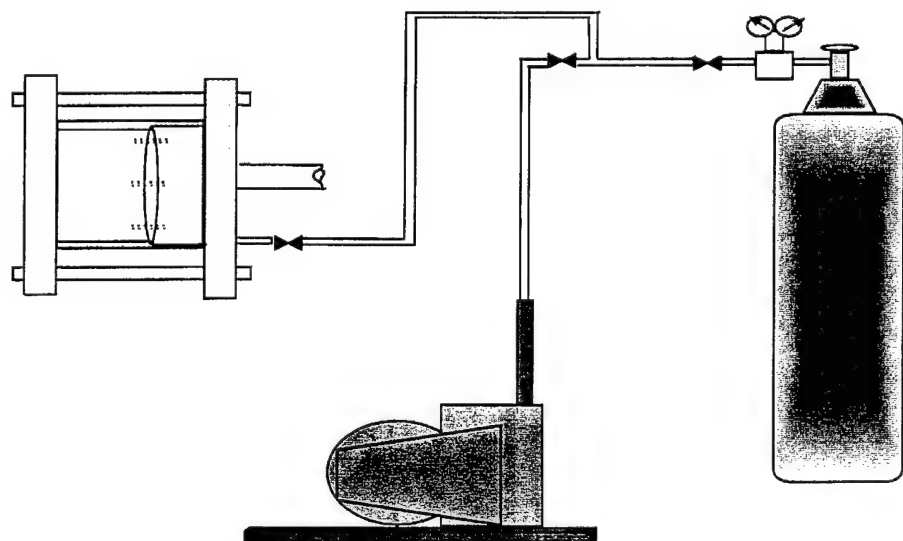


Figure 3-9. Gas Pressurization and Evacuation System

C. EXPERIMENTAL PROCEDURE

1. Resonator Setup

Prior to any data acquisition, the acoustic resonator was assembled to fix the stack position to the desired location. Three predetermined locations, as described above, include the pressure node, pressure antinode, and a position between. With the stack positioned, couplings are tightened and secured with the restraining block assemblies. The system is then pressurized to 3 atmospheres pressure to verify system integrity. During this verification, helium was used.

2. Evacuation and Fill System

During the data acquisition, various gases are utilized. The evacuation and fill system is used to achieve gas purity within the resonator. This was accomplished by a series of evacuations and pressurizations. The system is brought to as strong of a vacuum as the attached Duo-Seal vacuum could pull, approximately 0.05 psia, followed by an immediate pressurization to three atmospheres. This procedure is repeated three times and then brought to desired pressure. Once completed, the estimated purity of the gas is greater than 99% pure. From the frequency spectrum, the resonant frequency modes for the gases used fully supported a pure gas concentration. The pressure inside the resonator is monitored using the custom amplifier, which was DC coupled with a open loop gain of 10.

3. Determining Resonator Characteristics

The Hewlett Packard 35665A Dynamic Signal Analyzer is used to characterize the resonator. The Swept Sine mode of the analyzer provides a sine wave signal to the system at a given range of frequencies. The frequency response of the system is used to determine the resonance frequency and quality factor of several modes of the resonator.

The Curve Fit mode is used to determine the quality factors or Q's for each peak. These measurements are performed for each gas type and each stack position.

4. Data Collection

Data collection is performed in sets where gas type, stack position, and mean pressure are held constant while the drive ratio varies. Figure 3-10 shows the *Procedure for Transient Temperature Gradient Data and Pressure Characterization Collection* form used during data acquisition.

Before data collection, the system is verified to be in thermal equilibrium by ensuring no temperature gradients were present on the stack. When this condition is achieved, steps 1 through 3 are recorded on the data collection form. DC offset, the microphone offset at atmospheric pressure, is predetermined and assumed to be constant throughout each data set. The temperatures T_{ref} and T_{wall} represent the temperatures of the isothermal block and the resonator wall. The desired mean pressure is recorded and converted to a voltage to verify actual pressure settings. Actual pressure settings in psi and millivolts are recorded as P_{mean} . Resonant frequency f_0 is located and recorded. The final parameter calculated is the drive voltage required for the desired drive ratio. This calculation provided a convenient means for setting amplifier gain required at the start of each data run. Actual data runs are commenced with the system equilibrated and initial conditions recorded.

A data run is commenced first by activating the data acquisition software, LabVIEW, and allowing the computer to record ambient conditions for approximately ten seconds. With the computer still recording, the gain on the amplifier is immediately raised to the required drive ratio to drive the speaker. The drive ratio is monitored using the Endevco microphone which at this point is being amplified with an AC coupling and a gain of 100. The actual drive ratio voltage applied is then recorded on the data collection form. When being driven at high amplitude, the microphone output typically decreased slightly over the duration of the run. However this change in level was typically less than 0.3%. Driving the speaker begins the evolution of the temperature gradient within the stack. The speaker remains amplified for several minutes to ensure

that steady state conditions are achieved. The driver is then turned off and LabVIEW continues to record data during system equilibration. After several more minutes, LabVIEW is deactivated and the data is saved.

Procedure for Transient Temperature Gradient Data and Pressure Characterization Collection

Date: _____

Time: _____

Stack at: a. Pressure Node b. Velocity Node c. 1/2 way in between

1) Record DC Offset: _____ Argon Helium Nitrogen Air Other

Record T_{ref} : _____ T_{wall} : _____

Record Desired Mean Pressure: _____ psia Drive Ratio: _____

Calculations:

Record needed voltage for pressure: _____,

2) Record P_{mean} : _____ mVDC _____ Psig on local pressure gauge

3) Locate and record f_0 : _____ Hz, Let equilibrate. Calculate drive ratio voltage (3114.3 pa/.1vrms)

Record drive voltage needed per percent: _____ Mark drive ratios on amplifier.

4) Take measurements and save data.

Record time/point: _____ Actual Drive ratio: Begin _____ End _____

Data file Name: _____ Record on/off time: _____

5) Rerecord P_{mean} : _____ mV ΔT : _____

6) Resonant Frequencies: _____ File: _____

f_0					
Q					
poles					
file name					

Figure 3-10. Data collection form for temperature gradient and pressure characterization

IV. OBSERVATIONS, RESULTS, AND DISCUSSION

A. RESONATOR TUBE CHARACTERISTICS

The frequency response of the resonator was determined for the various conditions and are listed in Table 2.

Condition	f_0	Q_0	f_1	Q_1	f_2	Q_2	f_3	Q_3	f_4	Q_4
Argon (e)	33.2	23.0	80.1	30.0	131.7	61.8	183.6	54.7	234.5	41.8
Argon (1/2)	33.1	22.3	81.1	30.0	131.7	38.2	183.5	62.3	235.2	66.7
Argon (p)	32.6	21.2	79.2	32.9	129.4	43.0	179.8	48.1	229.8	43.3
Argon (v)	32.6	22.3	80.0	34.5	130.2	48.1	181.0	53.0	231.9	39.2
Helium (e)	102.5	12.4	250.4	20.1	402.6	21.0	564.0	4.56	753.5	35.9
Helium (1/2)	99.3	9.3	246.2	22.9	397.2	23.4	565.3	21.9	735.3	35.8
Air (e)	35.8	22.5	86.8	32.6	141.5	43.4	197.0	52.3	251.3	29.2
Air (1/2)	36.0	20.7	88.4	28.2	143.8	34.6	200.4	81.6	256.8	51.2

Table 2. Frequency and quality factor for the first five modes of various gases with the following stack positions: $1/2$ - halfway between pressure node and velocity node; p - pressure node; v - velocity node; and e - no stack. Mean pressure for these runs was 1 ATM. Mean temp was 22 °C.

The frequency response allowed determination of approximate resonance frequency modes for subsequent data runs. The mode labeled f_1 was selected to ensure that the stack was positioned in the proper location. Measurements were also taken for an empty resonator to quantify any differences that the presence of the stack created. As listed in the table above, the differences between whether or not the stack was installed are negligible.

Figure 4-1 is a plot of the frequency response for Argon with the stack located halfway between pressure node and velocity node. It shows the lowest five modes. As discussed above, the second mode, f_1 , was used for most of the measurements. The corresponding wavelength is approximately 4m.

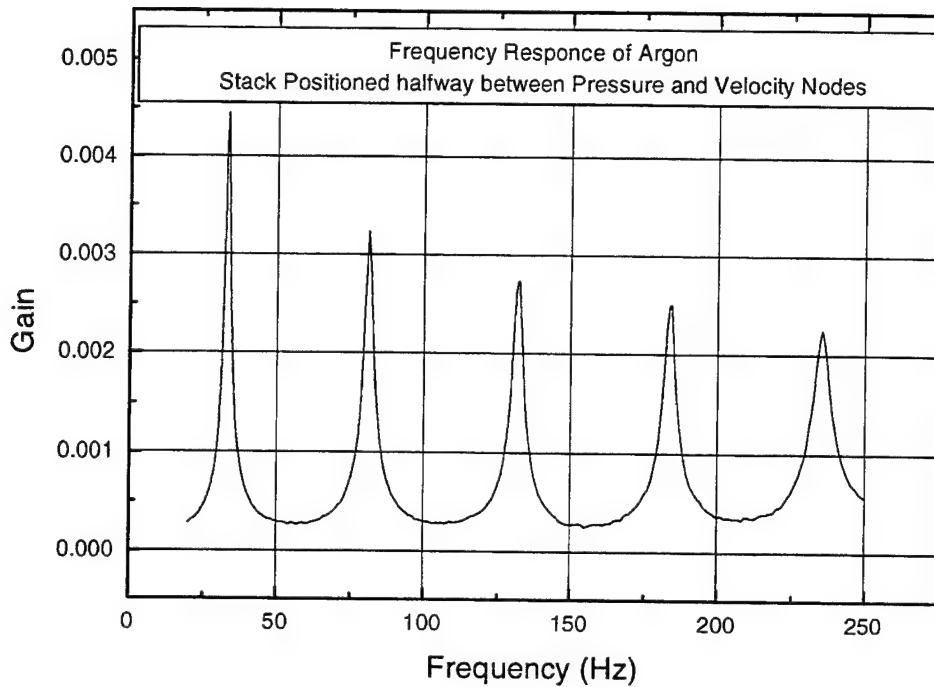


Figure 4-1. Frequency response of Argon at 1 ATM, with stack positioned halfway between pressure node and velocity node.

B. RESULTS AND DISCUSSION

1. Comparison of Low and High Drive Ratio

A typical experimental result for a low value of the drive ratio is presented in Figure 4-2 and depicts the evolution of the temperature gradient over time. Nine curves are displayed representing the nine thermocouples on the center plate showing their change in temperature with time. The red curves represent thermocouples 1 and 9, those thermocouples closest to the plate edge. The yellow curves represent thermocouples 2 and 8, green curves represent thermocouples 3 and 7, blue curves represent thermocouples 4 and 6, and the cyan curve represents the center or thermocouple 5. Notice that the first ten seconds depict an equilibrated system with all temperatures equal.

After approximately 10 seconds, the driver is turned on and the temperatures change. For this particular result, Argon gas was used at 10 psia mean pressure with a 2 percent drive ratio. The stack was positioned 149 cm (approximately $3\lambda/8$) from the rigid end with thermocouples 1 through 4 being closer to the pressure antinode. Similarly, thermocouples 6-9 were closer to the pressure node. The driver was driven at a frequency of 80.3 Hz with the resonator temperature at 26.4 °C, as measured by the hand-held monitored, wall mounted thermocouple. The corresponding wavelength in Argon is 4 m. As expected, thermocouples 1 through 4 increased above mean temperature while thermocouples 6 through 9 decreased below mean temperature. Thermocouple 5, the center thermocouple shows a slight increase in temperature due to both viscous and thermal heating. The maximum ΔT , difference between thermocouples 1 and 9, is approximately 3 degrees. At approximately time 210 seconds, when steady state conditions seemed apparent, the driver was secured. The remaining time graphed depicts the temperature decays during system equilibration.

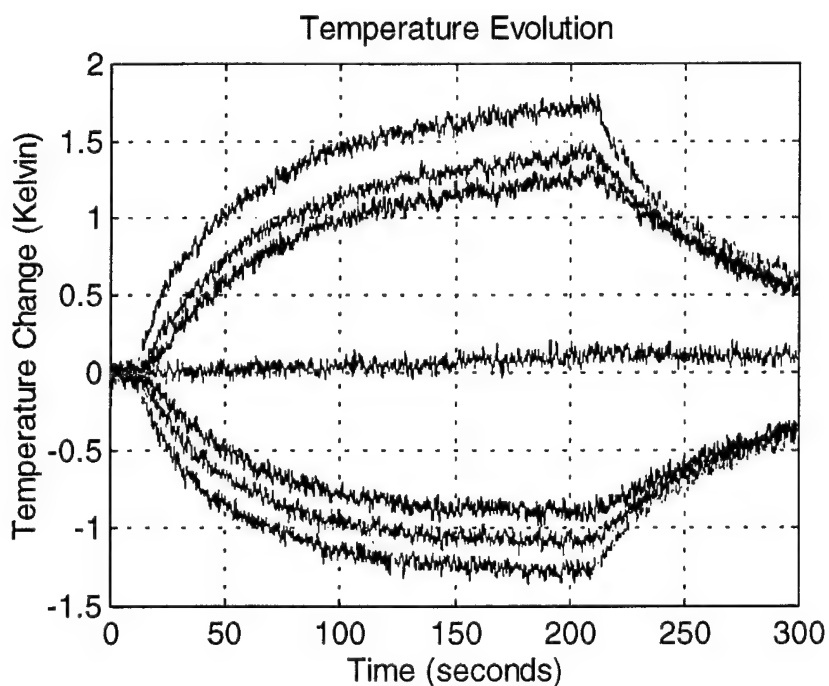


Figure 4-2. Temperature evolution for typical low drive ratio result. Argon gas was used at 10 psia mean pressure with a drive ratio of 2%. The stack is positioned between a node and antinode.

Figure 4-3 is an experimental result for a higher drive ratio, specifically 5%, for the same gas, Argon, at the same mean pressure. The resonator tube temperature was 25.4°C and the driver was again driven at 80.3 Hz. With this higher ratio, the general trends of the temperature evolution curves remain similar as those of 2%. There are, however a few differences. First, the overall ΔT has increased to about 8 degrees, which is expected for the higher drive ratio. And secondly, the effects of thermal and viscous heating are about a factor of 10 greater. One noticeable difference is the time to reach steady state temperatures. In this case, steady state was reached at about 90 seconds, much quicker than the 2% case at 210 seconds.

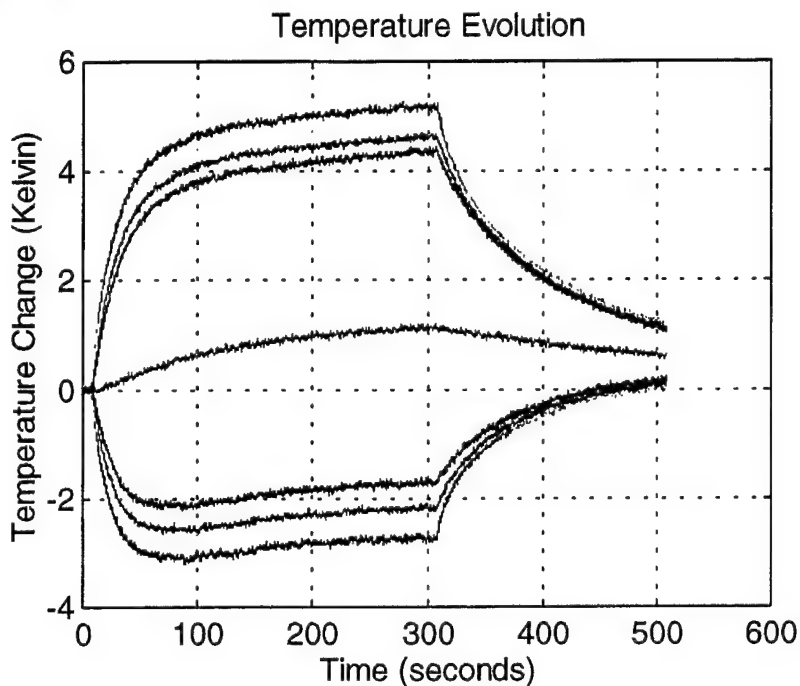


Figure 4-3. Temperature evolution for typical high drive ratio result. Argon gas was used at 10 psia with a drive ratio of 5%. The stack is positioned between a node and antinode.

In order to understand the differences in the transition to steady state conditions, an analysis of temperature gradients was made. Temperature gradients are defined to be differences in thermocouple temperatures divided by the distance between those thermocouples. For both cases, plots of temperature gradients versus time were developed to determine actual steady state conditions. Figure 4-4 shows the temperature gradient evolution for the 2% drive ratio. Four curves are displayed in the figure. The red curve represents the gradient formed by thermocouples 1 and 9, the yellow curve for

thermocouples 2 and 8, green curve for thermocouples 3 and 7, and the blue curve for thermocouples 4 and 6. As expected the gradients for the edge most thermocouples, the red curve, develops first and increases in magnitude more so than the other three curves. However, as time progresses, the gradients come together as they approach steady state. The steady state temperature gradient was approximately 45 K/m. Again, at time 210 sec., as the driver is secured, a decay in gradient is apparent.

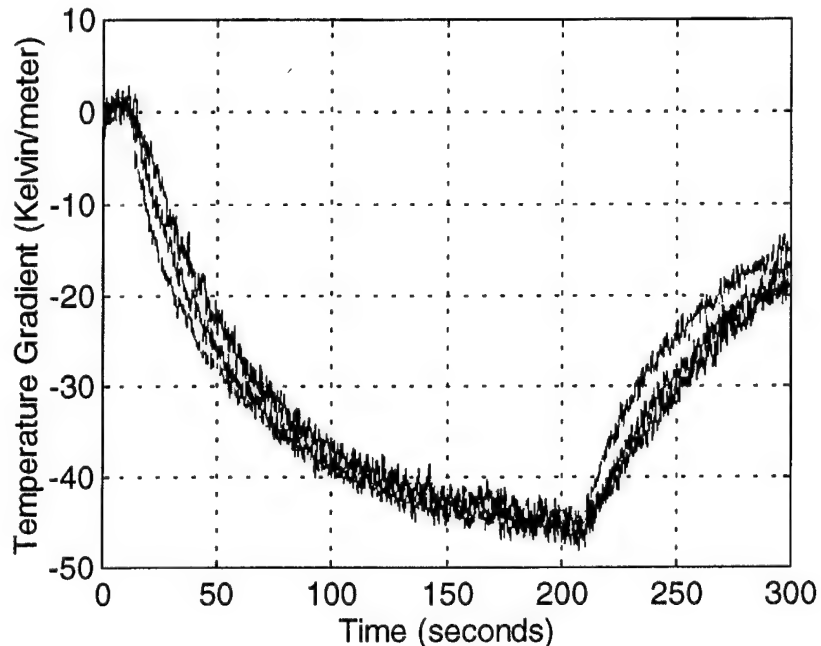


Figure 4-4. Temperature evolution for typical low drive ratio result. In the case argon gas was used at 10 psia with a drive ratio of 2%. The stack is positioned between a node and antinode.

The temperature gradient evolution for the 5% drive ratio shows noticeable differences as seen in Figure 4-5. This experimental result proved to be typical of higher drive ratios. Most apparent is the rapid development of the gradients and the shorter time to reach steady state conditions. Notice that steady state conditions were reached at a time of 100 seconds and that the maximum gradient was observed to be 130 K/m. Another major difference is the evolution of the gradients over time. As expected the gradients for the edge-most thermocouples developed first as seen in the 2% case. However, these gradients did not come together as they approached steady state. Instead, at this higher drive ratio, the inner thermocouple pairs, the green and blue curve, began to form larger gradients than the outer thermocouple pairs. This phenomena was observed

at about 30 seconds. These gradients remained larger throughout the course of the run and appeared to have grouped into two sets at steady state conditions. Initially, an assessment of the groupings was based on the differences in displacement amplitudes for different drive ratios. An attempt to validate this theory can be seen in Figures 4-6 and 4-7.

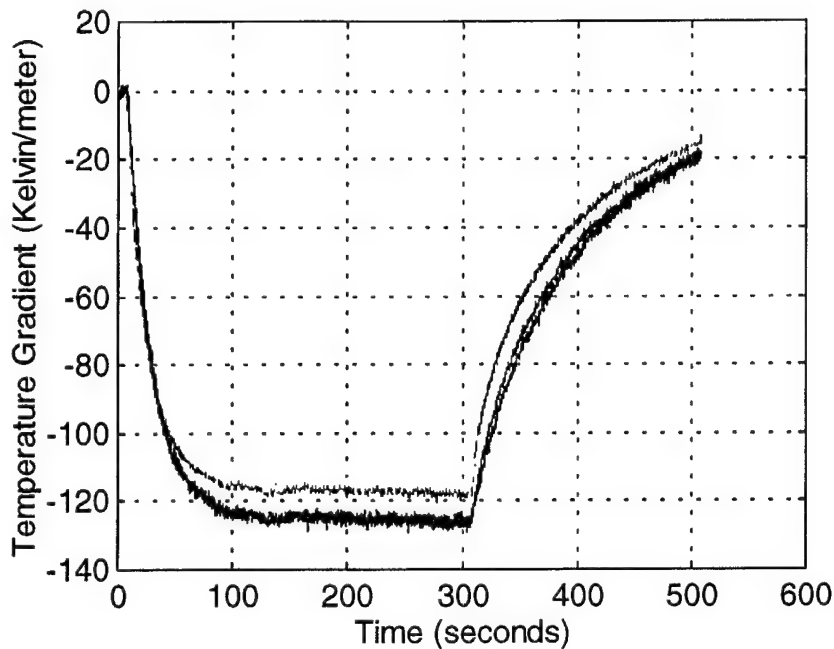


Figure 4-5. Temperature evolution for typical low drive ratio result. In the case argon gas was used at 10 psia with a drive ratio of 2%. The stack is positioned between a node and antinode.

Figure 4-6 is a plot of steady state temperature gradient versus drive ratio. For a given mean pressure, multiple drive ratios were examined and the resulting gradients are plotted against each ratio. As seen on the plot, the grouping of thermocouple pairs appear to begin at just below a 2% drive ratio. This grouping consist of two groups of two gradients and are consistent at higher drive ratios.

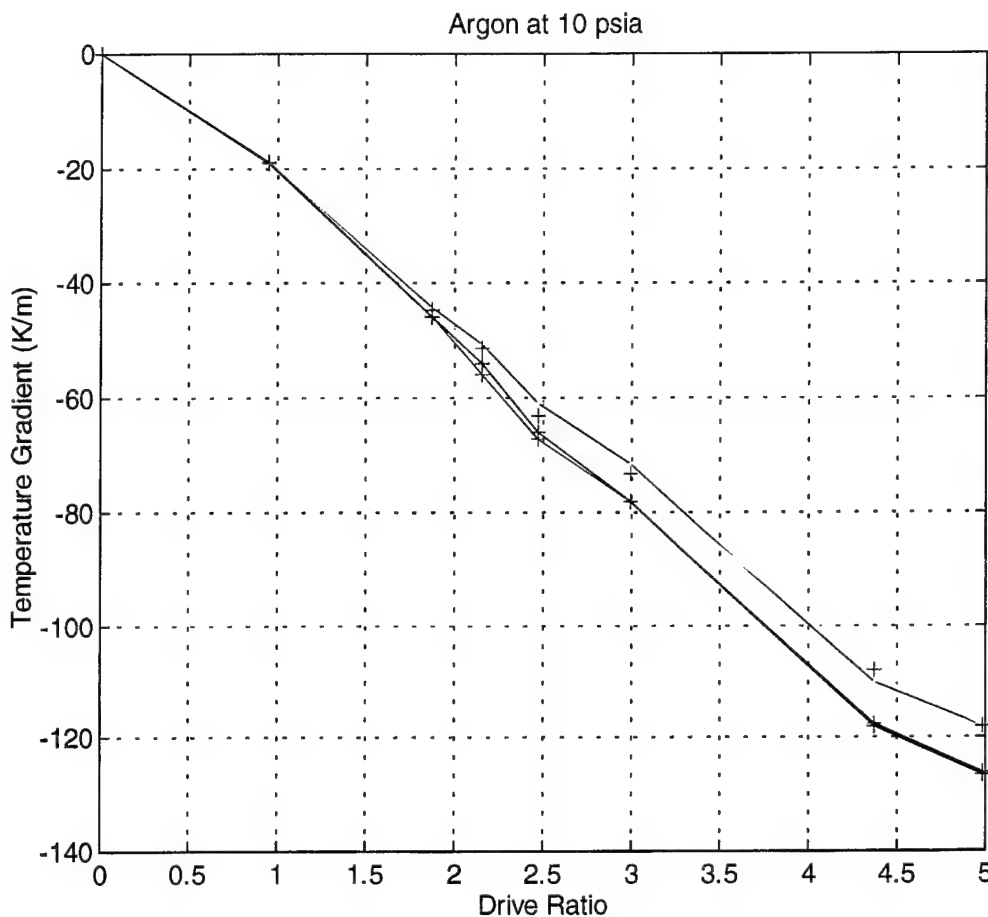


Figure 4-6. Plot of steady state temperature gradient versus drive ratio. The stack is positioned between a node and antinode.

In order to better understand the gradient development along the length of the plate, a more convenient parameter to examine is acoustic displacement amplitude. Acoustic displacement amplitude is the distance a gas parcel is displaced during one half an acoustic oscillation. In Figure 4-7, the peak-to-peak displacement amplitudes were determined for each drive ratio and then normalized by dividing the amplitude by the length of the plate. Therefore, for a 0.5 normalized displacement amplitude, the peak-to-peak oscillation spanned one half the length of the plate. Since displacement amplitude is proportional to the drive ratio, the general shape and location of the points in Figure 4-6 correlate well with those of Figure 4-7. The green vertical lines represent the average locations of each thermocouple pair with respect to the edge of the plate. For example, the first green line represents the average distance of thermocouples 1 and 9 from their closest plate edge. Thus, at a drive ratio of 2.5%, the corresponding normalized

displacement amplitude is about 0.2 or 20% of the plate length. 20% of the plate will easily span the four adjacent thermocouples near the edge. Therefore, one might assume that as the displacement amplitude increases, the effects of grouping the gradients would also increase. That is, when the normalized displacement amplitude spans three thermocouples, then three gradients might consolidate. As seen in the figure, this is not the case and thus, our previous speculation that the grouping was based on amplitudes, becomes invalid. This grouping of gradients in pairs is consistent at higher drive ratios and appears independent of gas, mean pressure, and frequency.

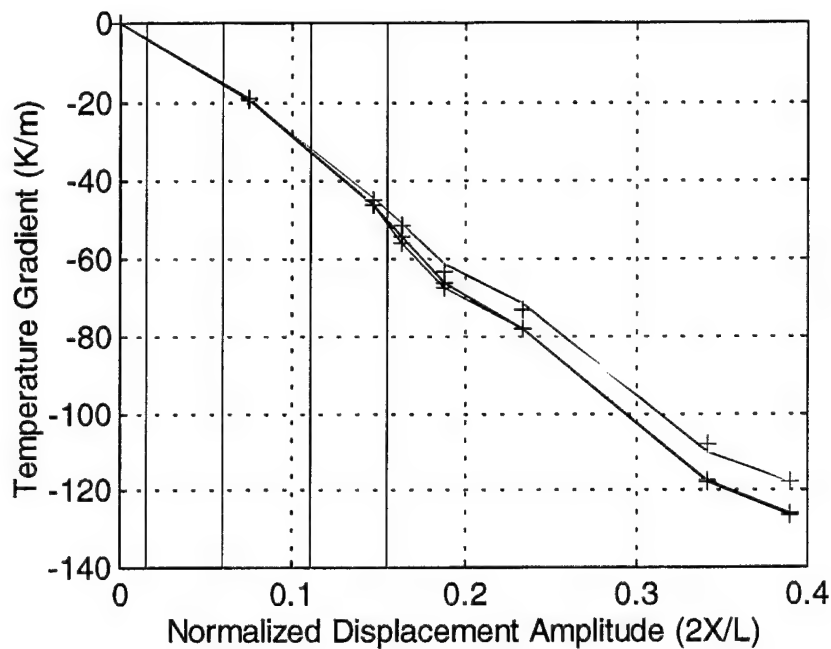


Figure 4-7. Plot of steady state temperature gradient normalized displacement amplitude. The stack is positioned between a node and antinode.

2. Comparison at Different Mean Pressures

Similar data sets were obtained for Argon at different mean pressures. Besides 10 psia, data runs were performed at 3 psia, 5 psia, and 18 psia. Figure 4-8 summarizes the findings for each pressure. The figure depicts four curves for each of the pressures with the same color coding that was utilized for the 10 psia graph. Additionally, specific points are plotted to show actual location of data points. The green vertical lines again

represent the average locations of each thermocouple pair with respect to the edge of the plate.

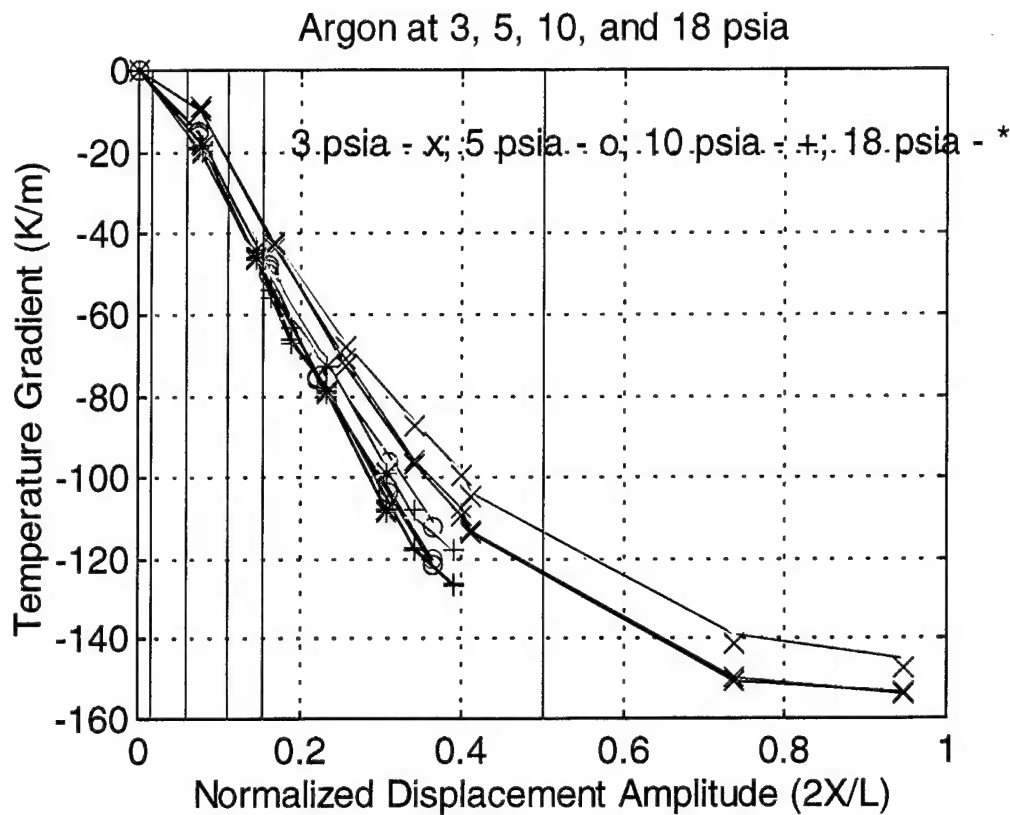


Figure 4-8. Plot of steady state temperature gradient versus normalized displacement amplitudes for mean pressures at 3, 5, 10, and 18 psia.

As seen in the figure, the gradients for each pressure have the same general trend in behavior. Note, however, that as mean pressure is increased, the gradients become larger. Also, the grouping of gradients that were apparent with the 10 psia data exists with these pressures as well. It is interesting to note, however, that the groupings remain in pairs even with normalized displacement amplitudes approaching the length of the plate. One might have expected, that as the displacement amplitudes increased, the grouping of gradients would tend to be in greater numbers, that is, all four gradients should have grouped together. This is not the case.

Another feature of Figure 4-8 of particular note, is how the gradients approach a limiting value. For the 3 psia case, the gradients seem to approach a value asymptotically. The critical gradient was calculated to be 350 K/m which is much greater in magnitude than what is seen. A more in-depth study of this asymptotic behavior,

determined this asymptotic value to be about one half the critical gradient [Ref. 1]. As depicted, this hypothesis is valid with the 3 psia data.

3. Comparison with Helium

Figure 4-9 is a plot of steady state gradient versus normalized displacement amplitude for both argon and helium gases. Again, the position of the stack is between a pressure node and antinode and the driver is driven at different drive ratios. In the case of helium, a maximum ratio of 1.5% was measured. As seen in the figure, much higher gradients are achieved for helium gas at a lower ratio.

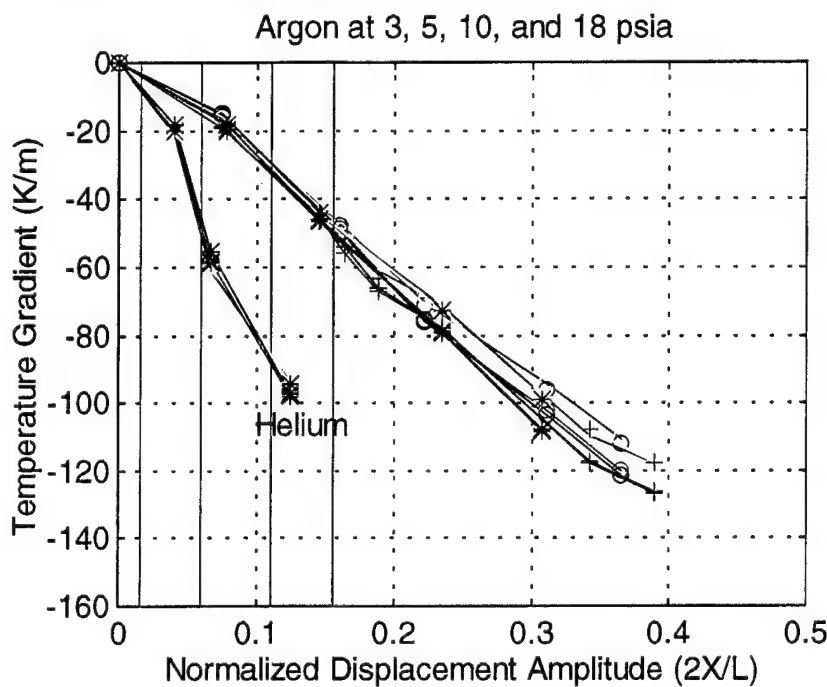


Figure 4-9. Comparison of argon with helium. Helium gas data taken at 15 psia.

4. Measurements at Pressure Node and Pressure Antinode

Measurements of the evolution of a temperature gradient were performed in the vicinity of a pressure node and a pressure antinode to observe the effects of both thermal and viscous heating. In both cases the node was within one centimeter of the center thermocouple (Thermocouple 5). Measurements were conducted at various mean

pressures and drive ratios using argon gas. A plot of temperature and temperature gradient versus time for the case of argon gas driven at a 6% drive ratio, can be seen in Figures 4-10 through 4-13.

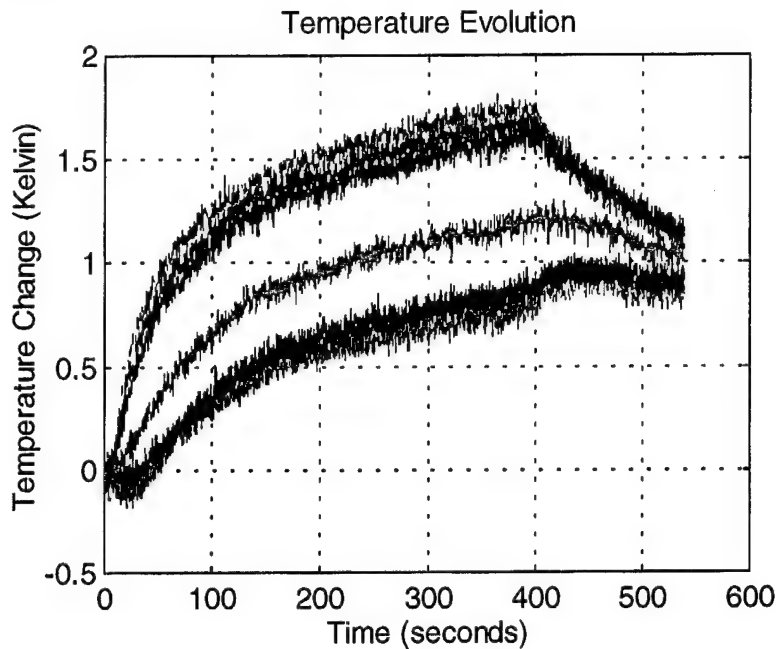


Figure 4-10. Temperature evolution for argon gas at 10 psia with a drive ratio of 6%. The stack is positioned at a pressure node.

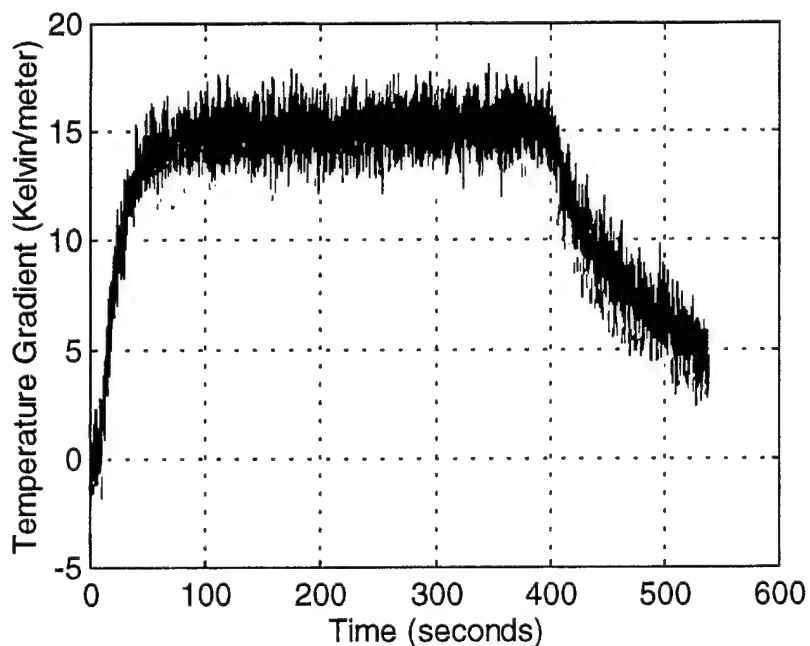


Figure 4-11. Plot of steady state temperature gradient versus drive ratio. The stack is positioned at a pressure node.

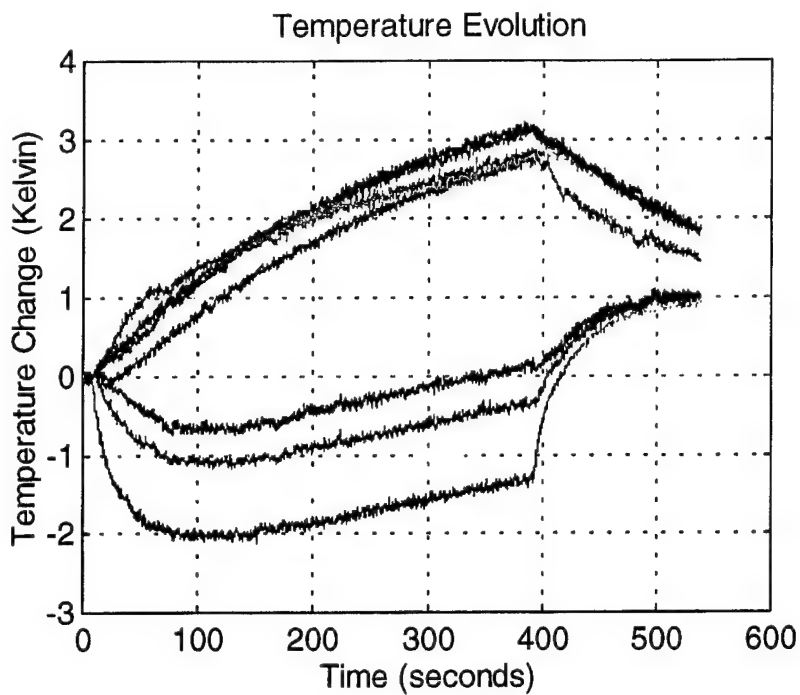


Figure 4-12. Temperature evolution for argon gas at 10 psia with a drive ratio of 6%. The stack is positioned at a pressure antinode.

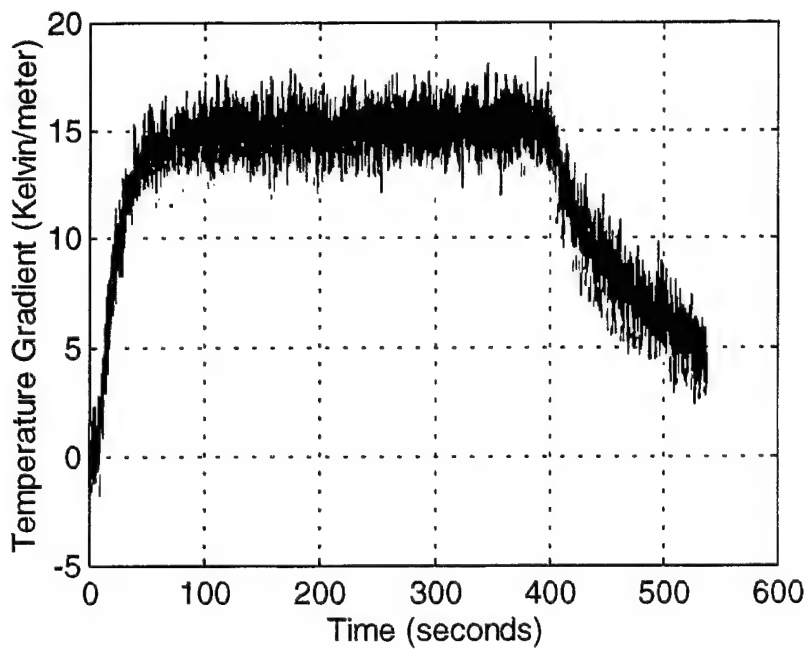


Figure 4-13. Plot of steady state temperature gradient versus drive ratio. The stack is positioned at a pressure antinode.

No careful analysis was conducted on the measurements with the stack positioned within vicinity of either the pressure node or pressure antinode. Interpretation of this data is left

as a challenge to new models.

V. CONCLUSIONS AND FUTURE WORK

A. CONCLUSIONS

The purpose of this thesis was to acquire data on the time evolution of the temperature profile in a simple thermoacoustic stack. This data is intended to be used by people developing nonlinear, time dependent models for thermoacoustics.

The evolution of the temperature profile in a parallel plate stack was measured for various gases at different stack positions, mean pressures, and drive ratios. The resulting profiles were then used to determine the evolution of temperature gradients, both in transient and in steady state conditions. Though most of the data collected is for argon gas with the stack positioned between a pressure node and pressure antinode, several conclusions can be drawn from this work.

As these gradients approach steady state, they settle at nearly the same constant gradient value. At higher drive ratios, however, beginning at just less than 2%, there appears to be two distinct differences in gradient behavior. The first difference is the crossover of temperature gradients during gradient evolution. As one may expect, the edge gradient formed quicker than the inner gradients, at a time from 25 to 50 seconds, the inner gradients overtake the edge gradients in magnitude. This behavior is a deviation from linear theory. The second distinct difference in higher drive ratios is the grouping of gradient pairs. It was seen that above about 1.5% drive ratio, the steady state gradients formed into two groups of gradient pairs: one group of the thermocouple pairs closest to the edge, the other group consisting of the inner thermocouple pairs. This behavior is apparent for all gas types, mean pressures, and stack positions, and seemed to be independent of the drive ratio or acoustic displacement amplitude.

Another conclusion can be drawn when comparing the trends of steady state gradients against drive ratio or acoustic displacement amplitude. Higher mean pressures yielded higher temperature gradients, though the general trend and grouping of gradients remained similar. In addition, the peak-to-peak displacement amplitudes were

approaching the plate length at the higher drive ratios and did not significantly alter gradient behavior.

Finally, measurements of the evolution of the temperature profile were made with the stack in the vicinity of a pressure node and a pressure antinode. These measurements were collected at varying mean pressures and displacement amplitudes yielding results for later analysis. Interpretation of this data is left for theoreticians and future study. The results of this thesis represents the most complete set of data of this kind.

B. FUTURE WORK

For future work, the results of this thesis can be extended into other gas types as well as improving the instrumentation of the stack. More thermocouples can be used along the plates entirety to monitor the temperature and gradient evolution over the entire length. Additionally, monitoring of the plate temperature in the transverse direction could show any irregularities from centerline.

Another area recommended for future study is the measurement of the evolution of the temperature profile of the gas between the plates of the stack.

Finally, the procurement of a much stronger driver may allow achieving much higher drive ratios thus taking the measurements further into the nonlinear regime.

APPENDIX A. LABVIEW

A. LABVIEW: OVERVIEW AND SETUP

Data was converted from the analog voltages produced by the thermocouples, to digital signals understandable by the computer using two Data Acquisition (DAC) boards. These boards were the NB-MIO-16X and the NB-MIO-16XE high resolution Multifunction I/O boards manufactured by National Instruments. These boards are controlled by the a graphical programming language LabVIEW. Although many of the particulars about these boards will be discussed elsewhere, the controlling language and the programs used will be discussed here.

LabVIEW is a graphical program language used to create “virtual instruments” that control data acquisition and instrumentation. Based upon a graphical programming language called *G*, it creates programs in a modular block diagram form. These modular blocks form functions that can be combined in various ways to meet various needs. The blocks are connected by “wires” that conduct information from one block to another. Thus programing is reduced to placing function blocks in the proper order and then connecting them with wires to transmit variables as needed [Ref. 11].

The interface between the operator and the program is called the “front panel”. These virtual front panels serve the same the purpose of an actual instrument front panel which they are meant to simulate. Necessary parameters can be inputed by the operator as well as well as output data displayed. The front panel turns the operator’s inputs into variables used by the LabVIEW program [Ref. 11].

A sample front panel is displayed in Figure A-1:

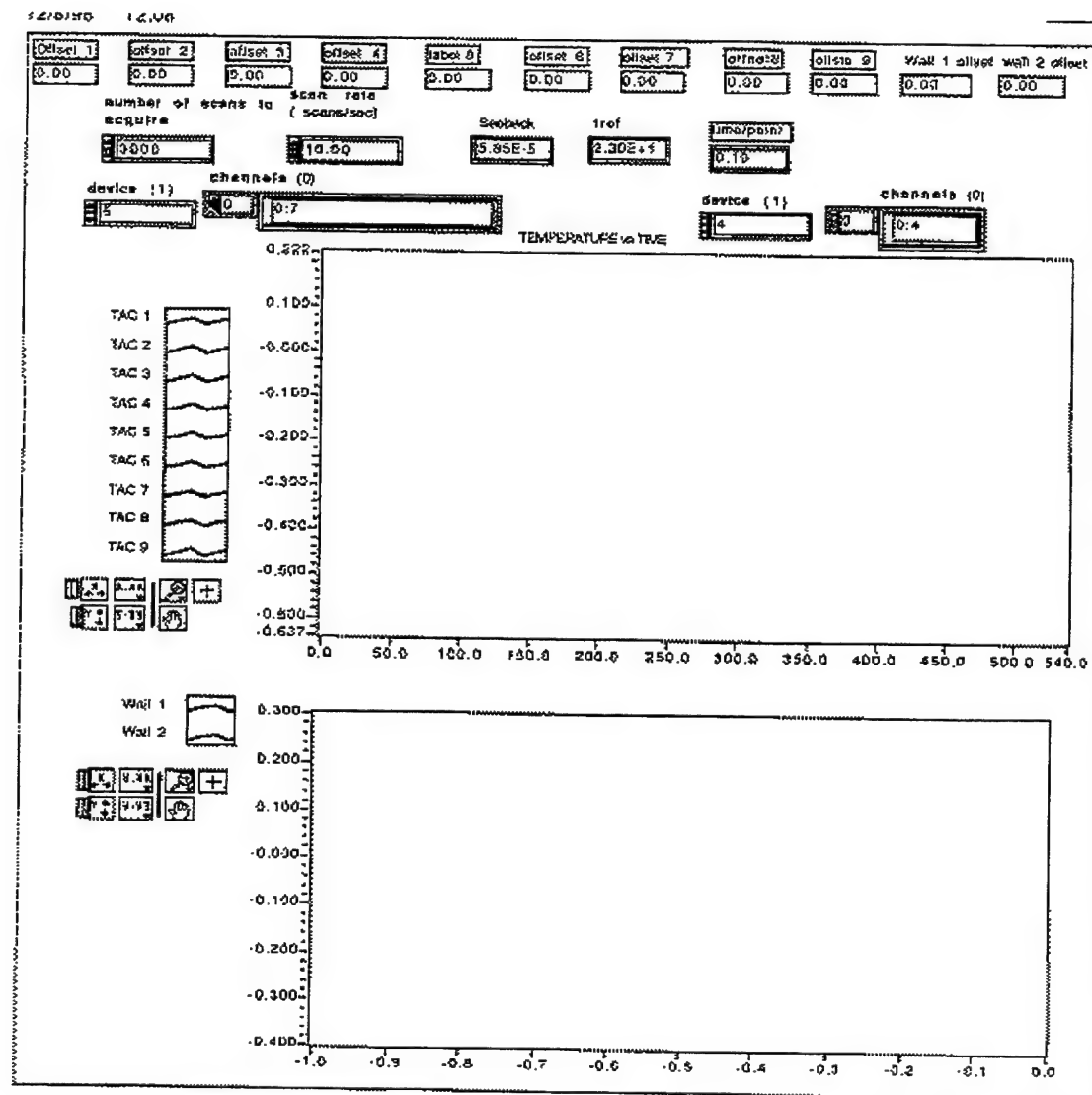


Figure A-1. Sample of a front panel used to control a VI

1. Program Pressure_Measure

Program Pressure_Measure.VI was used to monitor and record the Pressure inside the tube using inputs from the Endevco microphone. The other program, Plate_Measure.VI, recorded and plotted the data received from the various thermocouples. The suffix .VI indicates a virtual instrument program and is added to all LabVIEW programs. Both programs provide commands and control to properly operate the DAQ boards.

The basis for both programs was the sample program "Getting_Started_Analog_Input.VI" provided by National Instruments with the LabVIEW software [Ref. 11]. It is the most basic of analog-to-digital conversion programs, yet contains every item needed to gather analog data. It was made up of five separate VI's that were linked together to gather data from one DAQ board and display the results on a single graph.

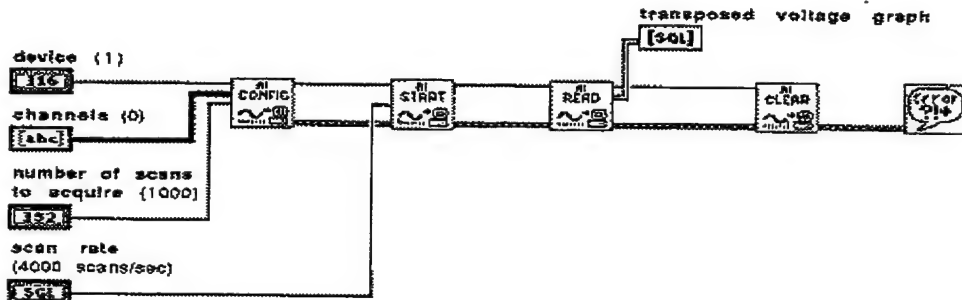


Figure A-2. Getting started Analog Input VI, the backbone of all the other VI's

The Components of this program, shown in Figure A-2, included the following VI's: AICONFIG.VI, AISTART.VI, AIREAD.VI and AICLEAR.VI, as well as an error function VI. AICONFIG's purpose is to configure whatever DAQ board the operator wants to use for whatever channels are needed. AISTART determines the length of time to collect data and commences gathering that data based upon the channels passed to it by AICONFIG. AISTART places the DATA in a FIFO (first in- first out) buffer and the results are passed on to AIREAD. AIREAD takes the data from the buffer and organises it into a usable memory addressable format. It is at this point the data can be saved or used for such things as graphs or further analysis. The AICLEAR empties the FIFO buffer, resetting it for the next round of data.

Each of these functions requires input from the function before it. AICONFIG is the first to output an error line, while all the others need an error line as an input and add any errors messages they produce on to it and pass it on to the next function. After AICLEAR, an error function VI inputs this error line and reads the errors that occur, taking appropriate action for each. This usually amounts to printing a error message to the screen for the operator. AICONFIG also needs a device input, channel input, and number of scans to aquire input. The device number corresponds to which DAQ device

is to be used, while the channels specify how many channels of data will be acquired for that board. The “number of scans” input determines how many points of data will be acquired for each channel. All three of these inputs have to be entered by the user on the front panel. Note how Figure A-1, the front panel used for Plate_Measure, has places for all those inputs to be typed in. AISTART needs this data as well, and also a scan rate. The scan rate is also a panel inputted parameter while the rest is wired in from AICONFIG. AISTART will output the data it takes which becomes the input for AIREAD.

Pressure_Measure uses this backbone but adds a more complete graphical package and the option to save data acquired to the computer. The graph (pressure vs time) was accomplished by routing the data outputed by the AIREAD to a bundle where it was correlated with the inverse of the scan rate. This gives a correlation scaled to seconds since the scan rate is user defined as scans/second. The result is outputed to a graph for display purposes instead of the chart used in the Getting_Started_AI_Input.VI. The reason for this change is that the graph function allows more display options than the chart function does. This program is shown in Figure A-3.

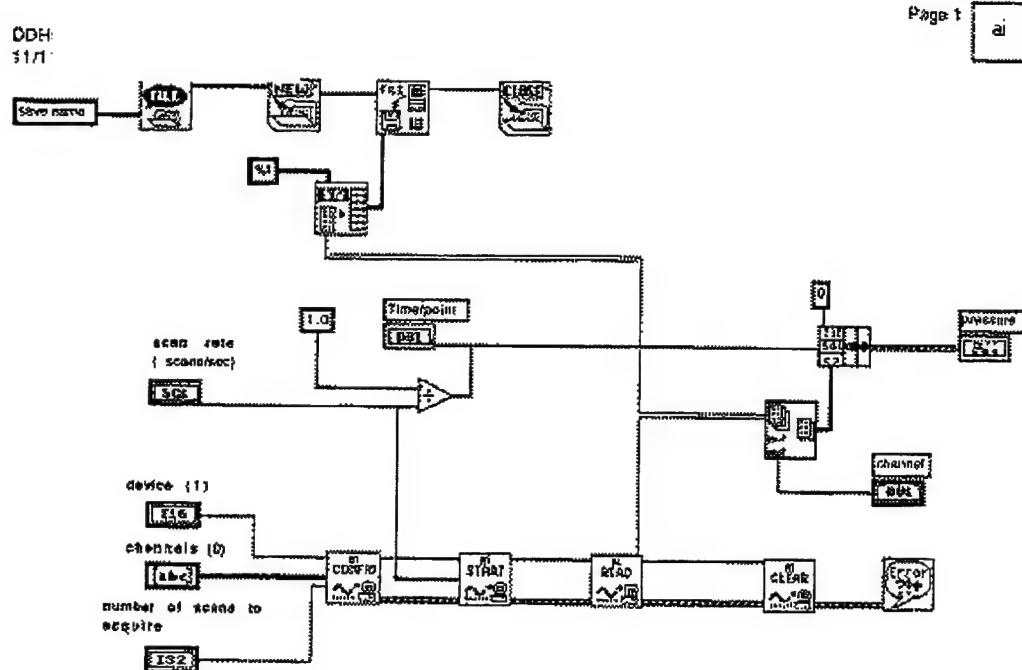


Figure A-3. Pressure_Measure VI program

2. Program Plate Measure

The Plate_Measure program is much more complicated as it required the near simultaneous use of both DAQ board's. The board's default setup allows them to run in a serial manner, i.e., the second board does not commence data acquisition until the first board is complete. Because the data's time dependency is critical, this is inappropriate for this experiment and was changed. This change is accomplished with a combination of hardware and software modifications.

The hardware change consisted of the connection of the RTSI bus to both data acquisition boards. The RTSI (Real Time System Integration) bus is a 50 pin ribbon cable that is used to send trigger and timing signals from one board to another. It is software driven as explained below [Ref. 12].

The software that controls the RTSI bus is programmed into the TAC_Measure VI. This requires that one board be designated the master board and the other the slave. The

master provides the clock signal, via the RTSI bus, that the slave uses to time its acquisition. The other critical factor is that the slave board must receive the signal to scan before the master. This is accomplished using a technique called data dependency.

The master board is selected by using the RTSI CONTROL function included in the LabVIEW VI library. This function controls which signal goes to the RTSI bus and when it occurs. As shown in Figure A-4, the RTSI CONTROL function (labeled as Cntrl in Figure (A-4)) is placed after the AICONFIG function but before the AISTART. The position is critical as the determination of which board is master or slave must be made before data is acquired during the AISTART function. This can not be done until the AICONFIG functions have determined which devices are active. Only one RTSI CONTROL needs to be placed in the program even though an AICONFIG needs to be present for each device used. This is because once the master assignment has been made, all other boards attached to the RTSI bus automatically become slaves.

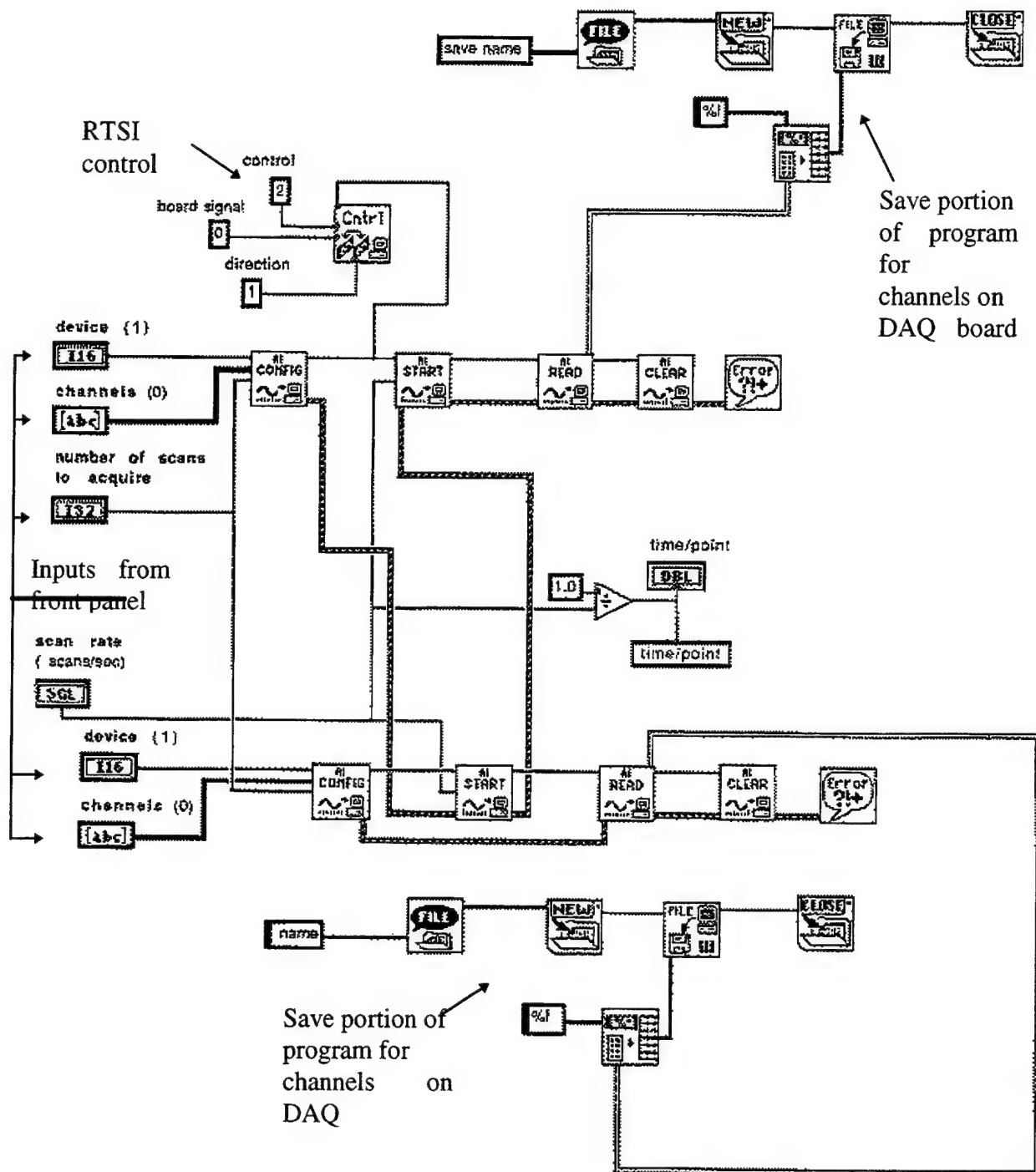


Figure A-4. Control portion of Plate_Measure VI.

The RTSI Control needs various inputs to function correctly. It requires a direction signal that will tell it if the AICONFIG it is attached to is the master or the slave. In the program Plate_Measure, it was wired to the master board and therefore a 1

was entered to reflect signals would be transmitted to the RTSI bus. An input for control and board signal also are required. The control code is used to override other inputs if necessary. This is not necessary in most cases however and therefore a 0, which denotes “do not change any control setting”, is entered as this input. The number 2 is inputed as the board signal, which determines which wire on the RTSI bus is used to convey the clock signal [Ref. 12].

Once the Control is in place a data dependency needs to be established to ensure the proper order of the AISTART functions. The slave needs to be activated first and this is accomplished by manipulating the inputs to the functions. LabVIEW will not execute a function until all required inputs are available [Ref. 11]. One of the required inputs is an error line. Normally this comes from the AICONFIG, however it can come from anywhere as long as it is in fact an error line. In Plate_Measure the error line from the master AICONFIG is not routed to the corresponding AISTART but in fact is routed to the slave AISTART. The error line output from the slave AISTART is then routed back up to the master AISTART as its input. Therefore the master AISTART never receives all its inputs until after the slave does. To complete the slave’s error sequence the error output of the slave AICONFIG is routed to the slave AIREAD. As long as the program is error free, rerouting of the error lines creates no ill effects for the overall program.

Once all the data is taken in a near simultaneous manner, all nine channels need to be plotted with the correct scales on the same graph. To accomplished this, each AIREAD VI creates an array of all the data acquired by the corresponding DAQ board. This array is routed along a pipeline, from which individual channels of data (columns of the array) can be pulled off. This happens with an “index array function” which has two inputs. One being the array of data, the other being the column of data desired. The function’s output is that column only. The proper channel is determined using an user defined input from the front panel. Figure(A-5) shows the array pipeline traveling down the left side of the page and where the index array functions pull off columns worth of data. In our program thermocouples 2 through 8 were recorded using the master DAQ board, while thermocouples 1 and 9 were recorded on DAQ board nr 2. The second DAQ board also recorded thermocouples 10 and 11 which were the resonator wall temp at the forward and aft edge of the stack.

Since the output only consists of one channels worth of data, it can then be routed to a bundle just as it was in the Pressure_Measure, and from the bundle to a graph. The only difference is that the data needs to be scaled to temperature and not as a voltage as the pressure was plotted. To scale appropriately, the voltage data is divided by a user defined variable called the Seebeck coefficient using the LabVIEW divide function. For our application, we used the constant value $5.85\mu\text{V}/^\circ\text{C}$ as our Seebeck coefficient. This number was derived from table III of Reference 10. Table III is a table of thermoelectric voltages corresponding to temperature for a type E thermocouple. The average voltage difference between each degree between 20°C and 30°C was $5.85\mu\text{V}/^\circ\text{C}$. Then another user defined variable called T_{ref} is added to the result of the previous division, using the LabVIEW addition function. We used a value of 0 for T_{ref} , so that we could plot the difference each thermocouple had with time. However the program was written so that the plates actual temperature could be inputed here. This would have given the actual temp of each thermocouple with time. The result is a collection of data with units in degrees Celsius. The x-axis scaling is accomplished just as it was for Pressure_Measure, with the results plotted in seconds. Channels 1 through 9 are plotted together on one graph, with the results published in appendixes C through J. Channels 10 and 11 were plotted on a second graph. The results showed no correlation to plate results and therefore are not included here.

The accuracy of the LabVIEW values of temperature changes was verified by taking a typical data run and during the run disconnecting the thermocouples and recording their actual value as sensed by a calibrated hand held Omega thermocouple thermometer. The run used was data run 9 of Appendix E, 3% drive ratio run for Argon at 10psia positioned halfway between the pressure node and antinode. A comparison between the ΔT as sensed by LabVIEW and as sensed by the Omega Thermometer is shown in Table A-1. This table shows adequate correlation to accurately depict temperature changes.

	LabVIEW 1 st record	Omega 1 st record	LabVIEW 2 nd record	Omega 2 nd record
ΔT of couples 1and 9	4.25	4.2	4.25	4.5
ΔT of couples 2and 8	4.05	3.8	4.25	4.2
ΔT of couples 3and 7	4.0	3.9	4.05	4.1
ΔT of couples 4and 6	3.6	3.6	3.6	3.7

Table A-1. Comparison of LabVIEW measurements with Omega Measurements.

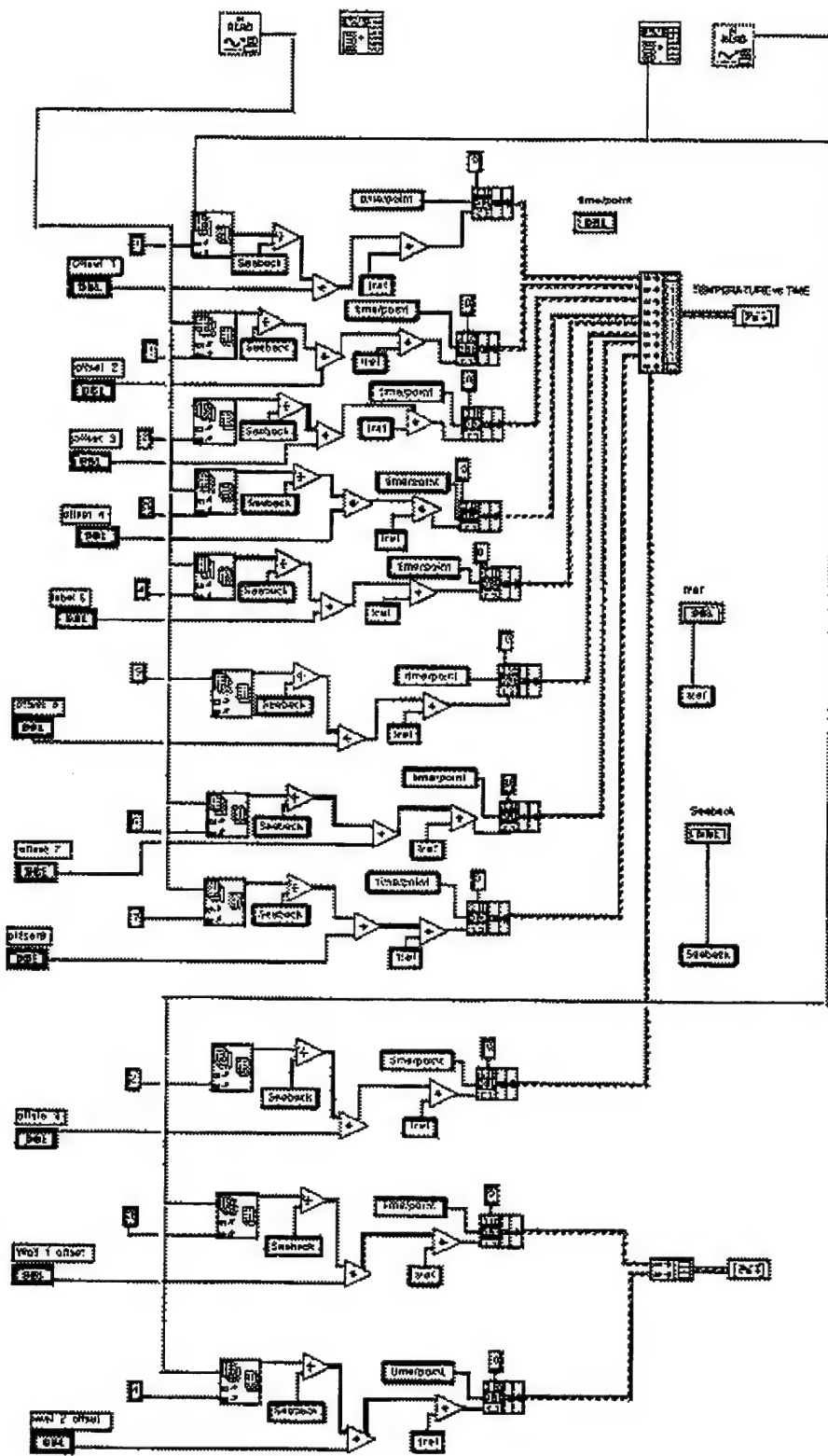
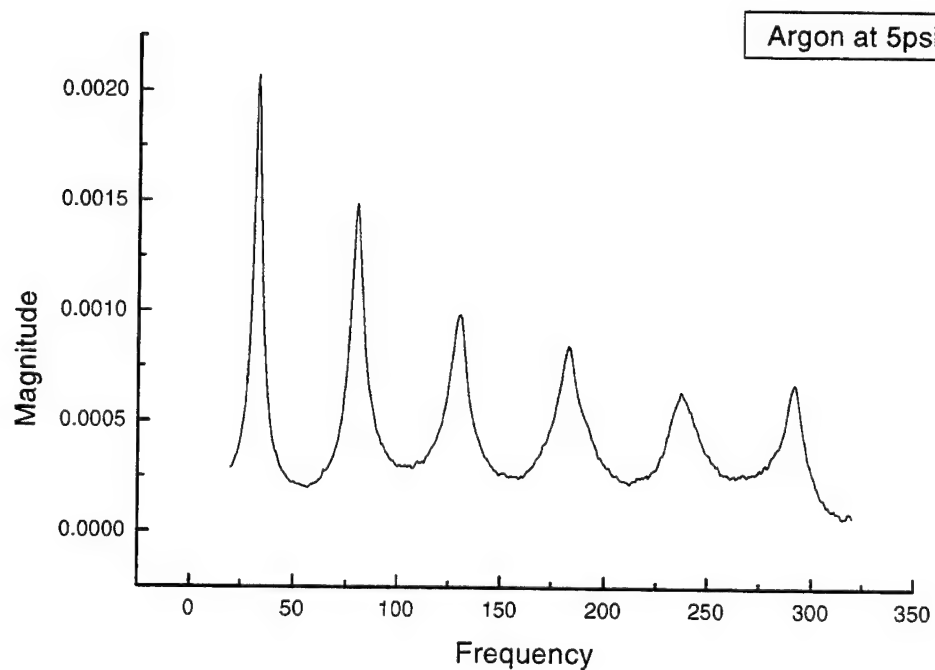
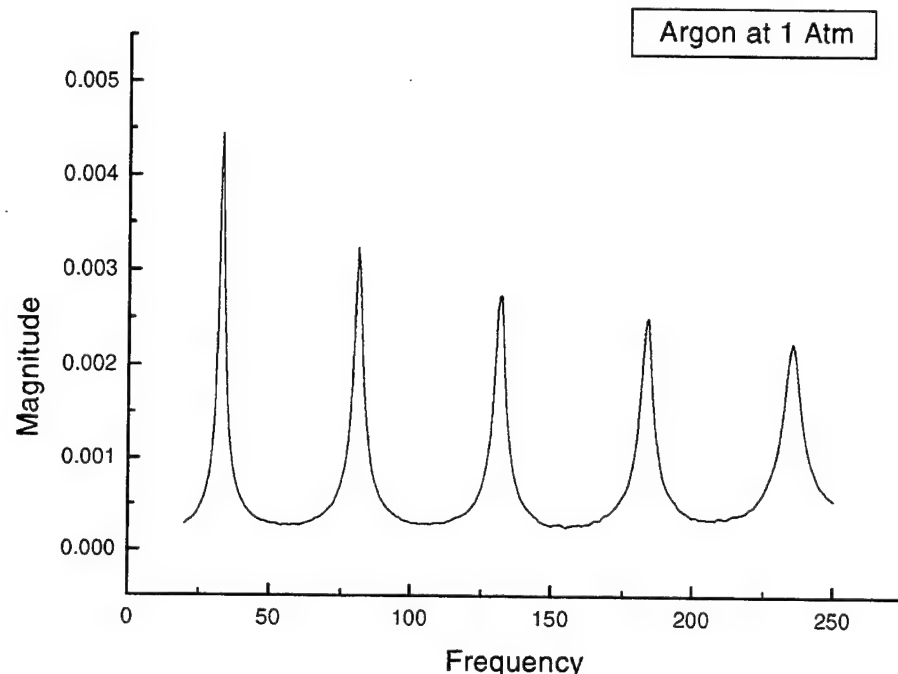
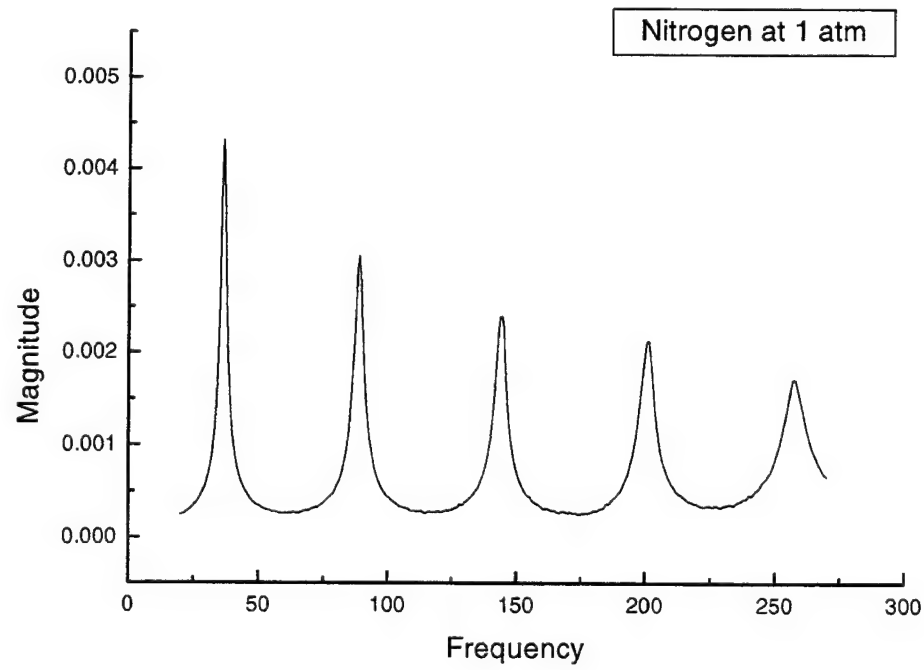
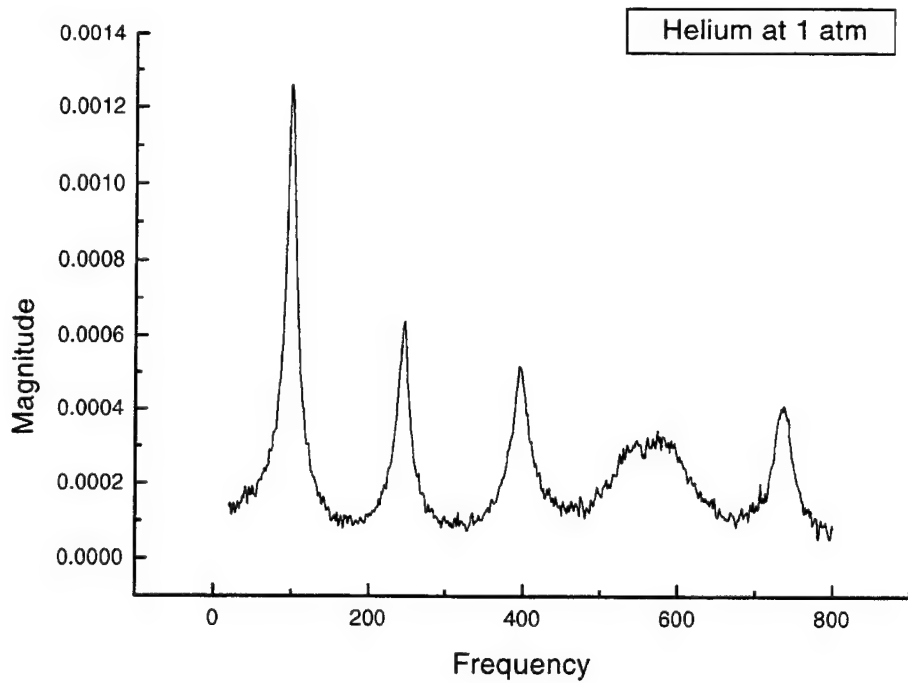
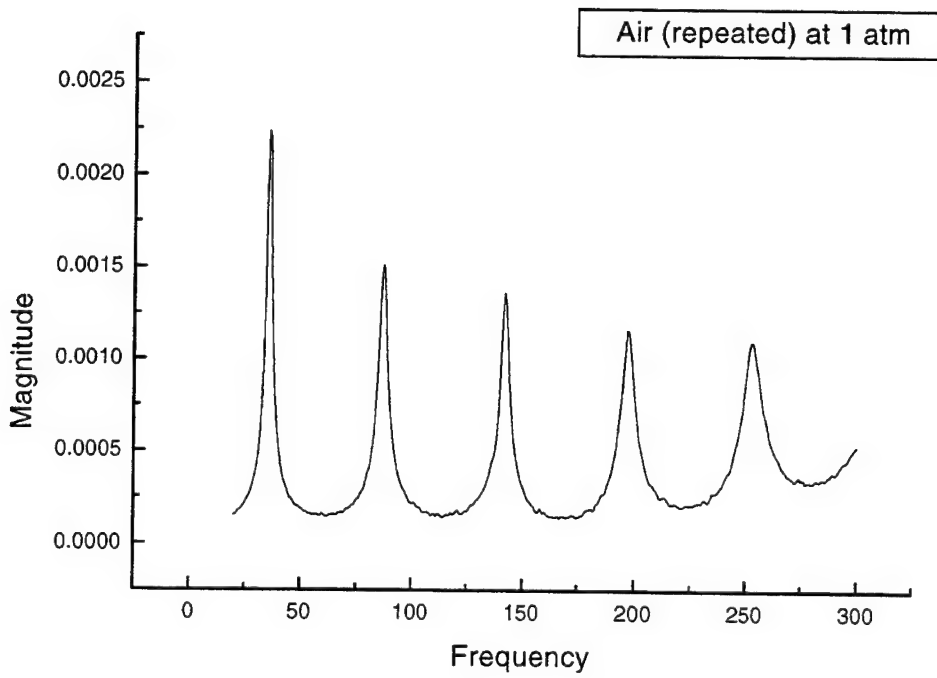
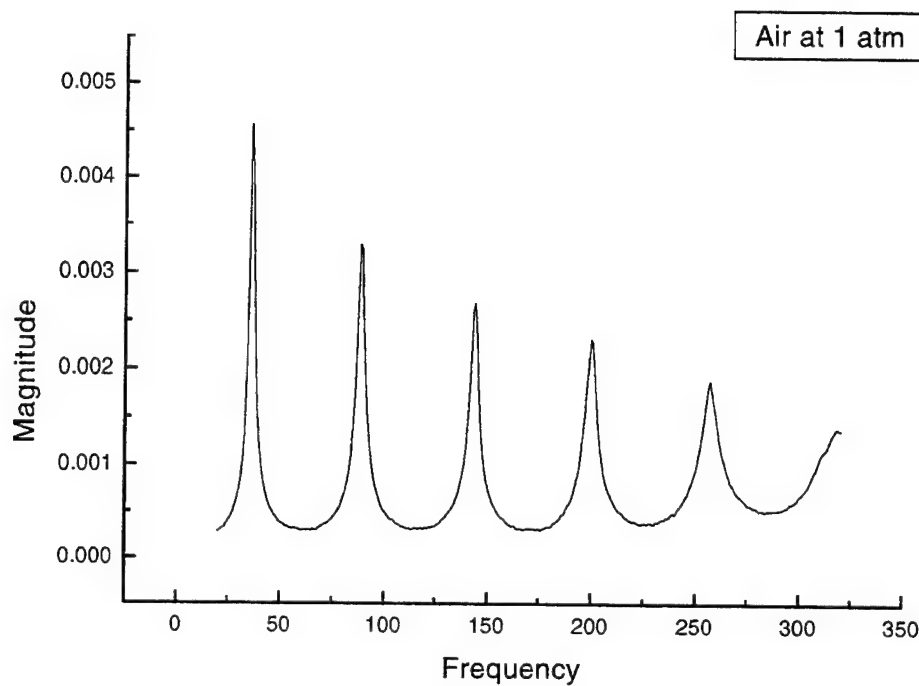


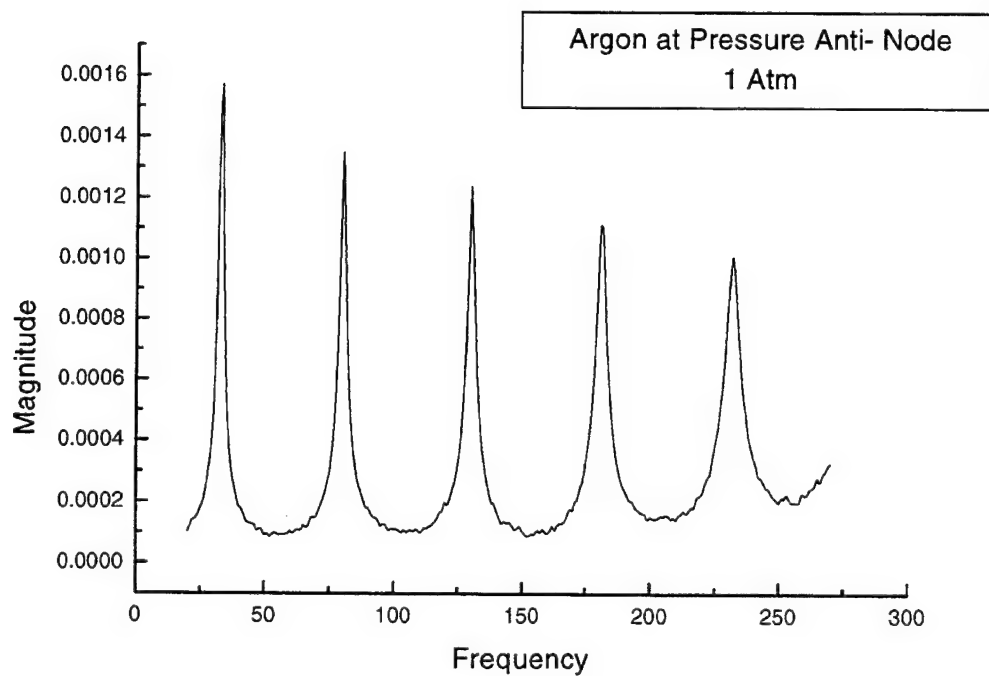
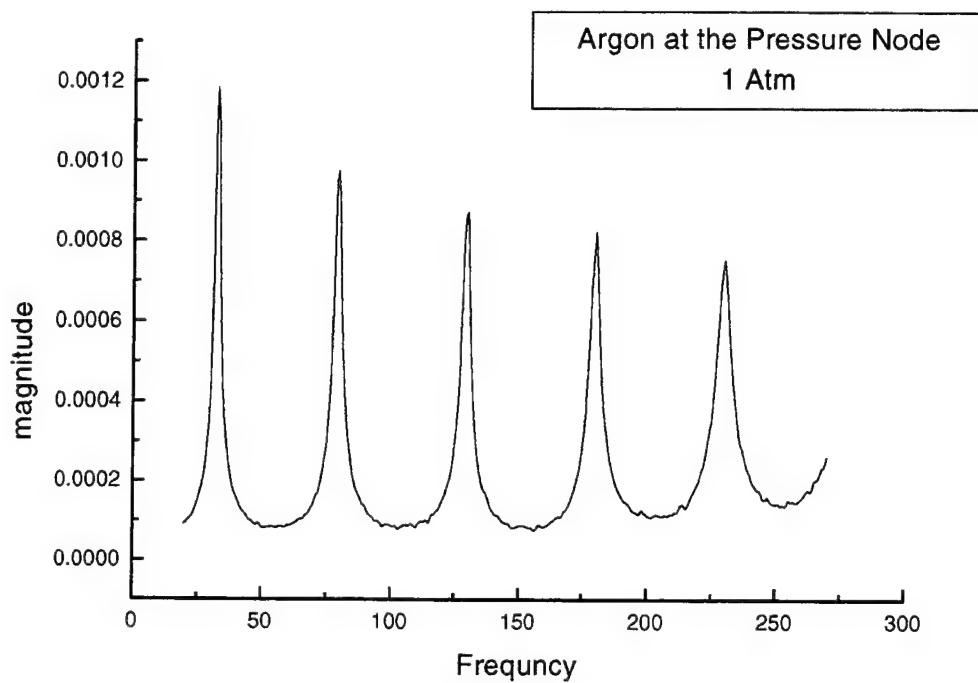
Figure A-5. The scaling and plotting portion of Plate_measure VI

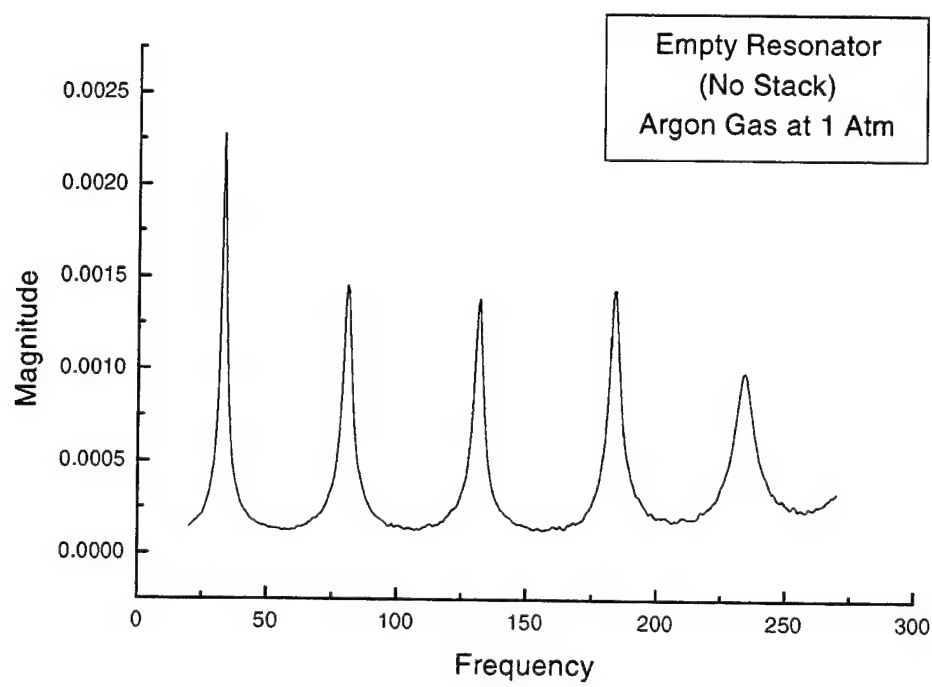
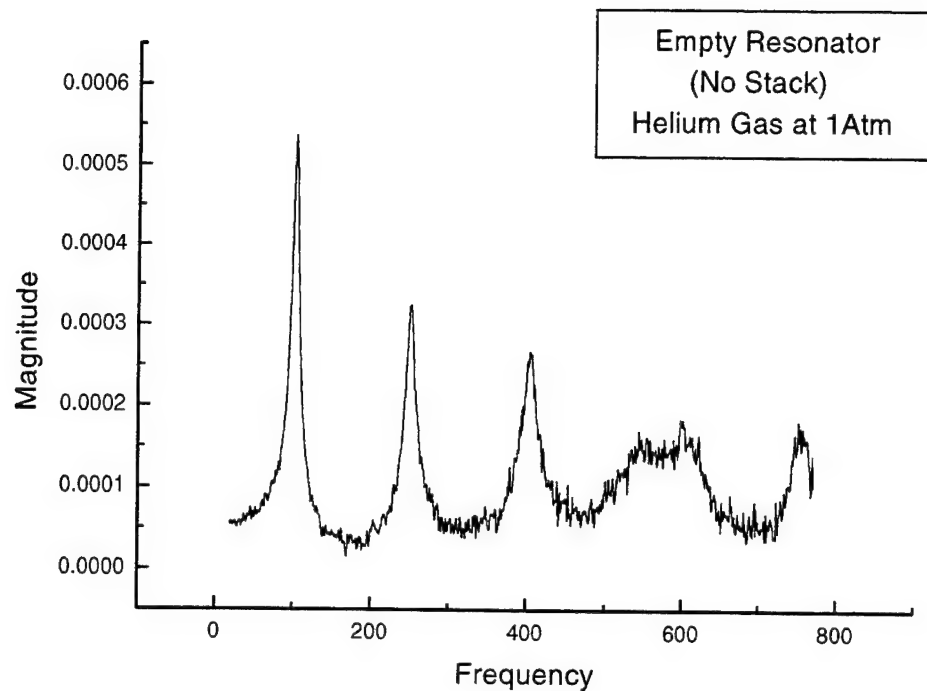
APPENDIX B. GRAPHS OF FREQUENCY ANALYSIS OF RESONATOR FOR DIFFERENT GASES AND PRESSURES

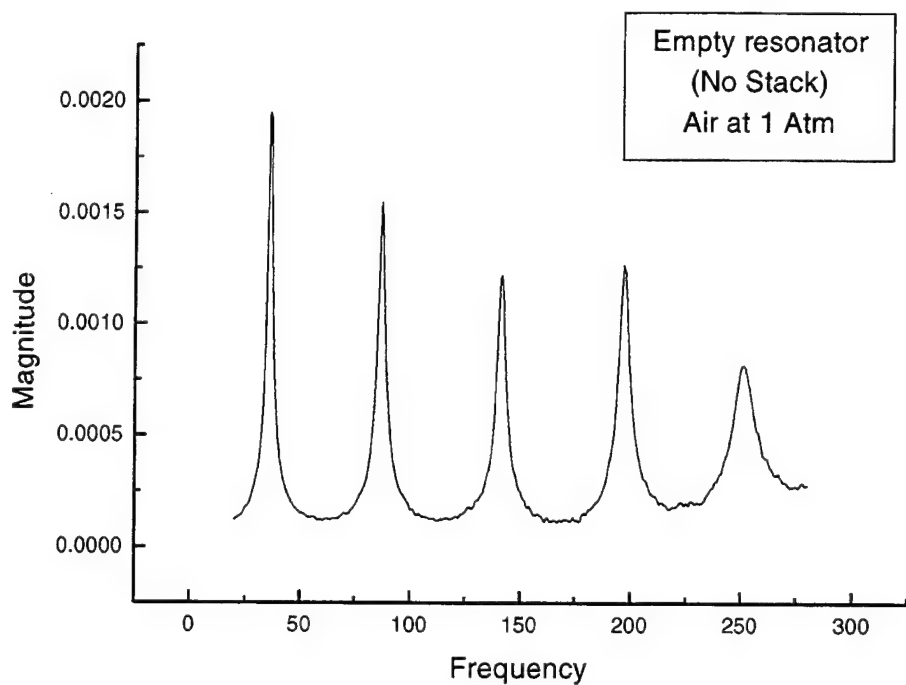








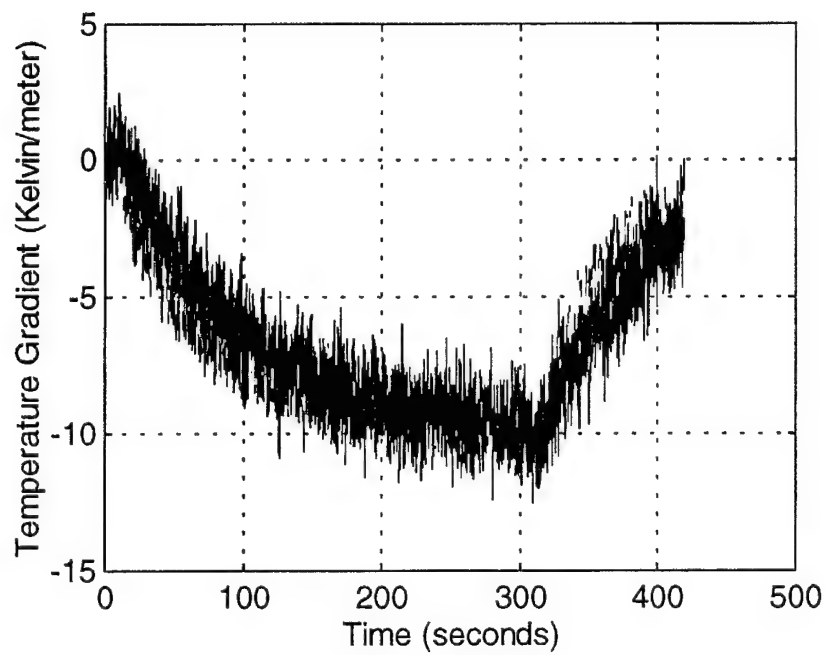
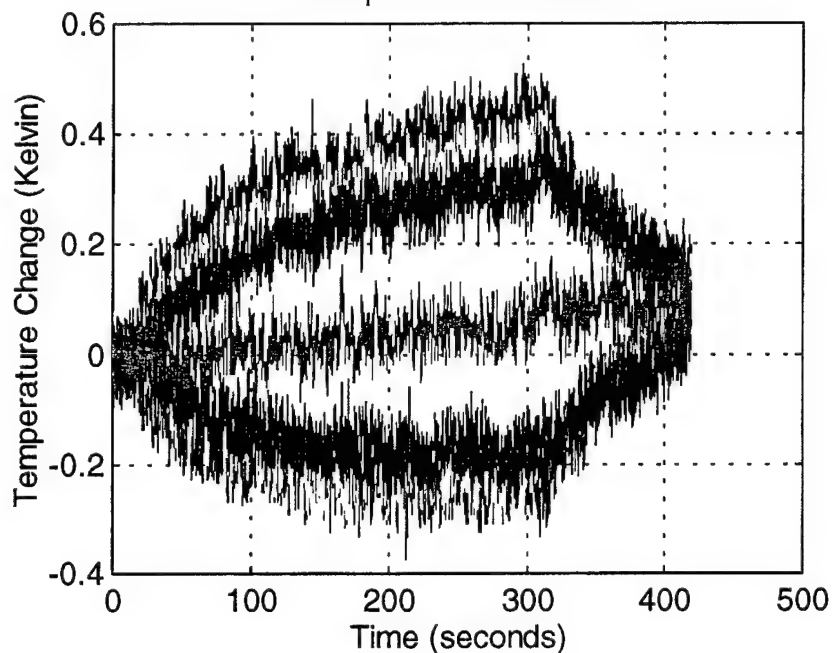




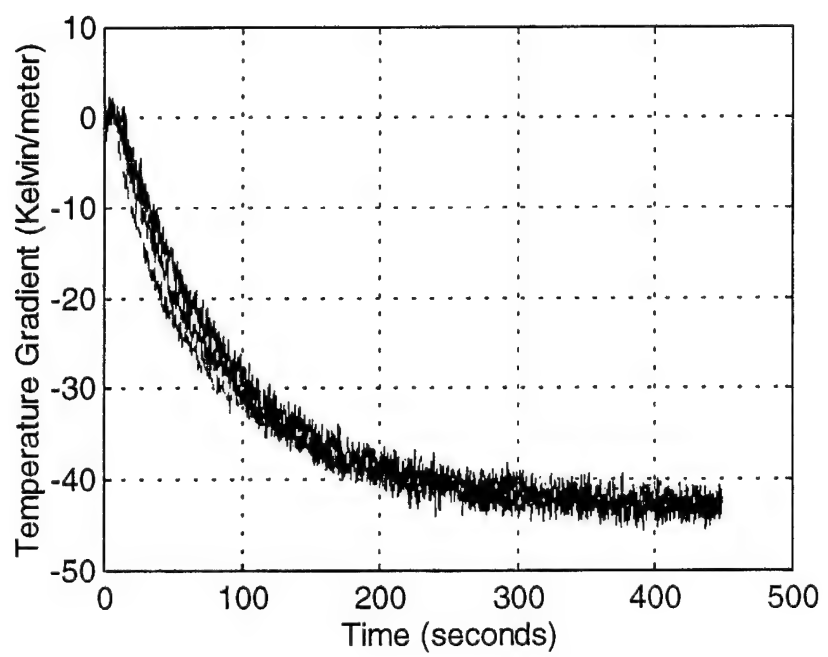
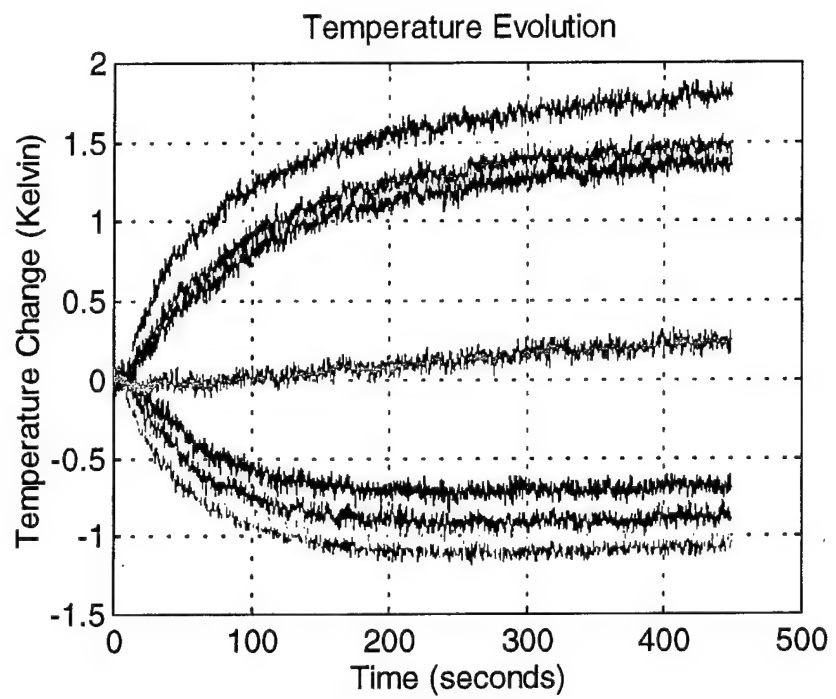
**APPENDIX C: ARGON GAS, 3 PSIA POSITIONED HALFWAY BETWEEN
PRESSURE AND VELOCITY NODES**

Run 1 1% drive ratio

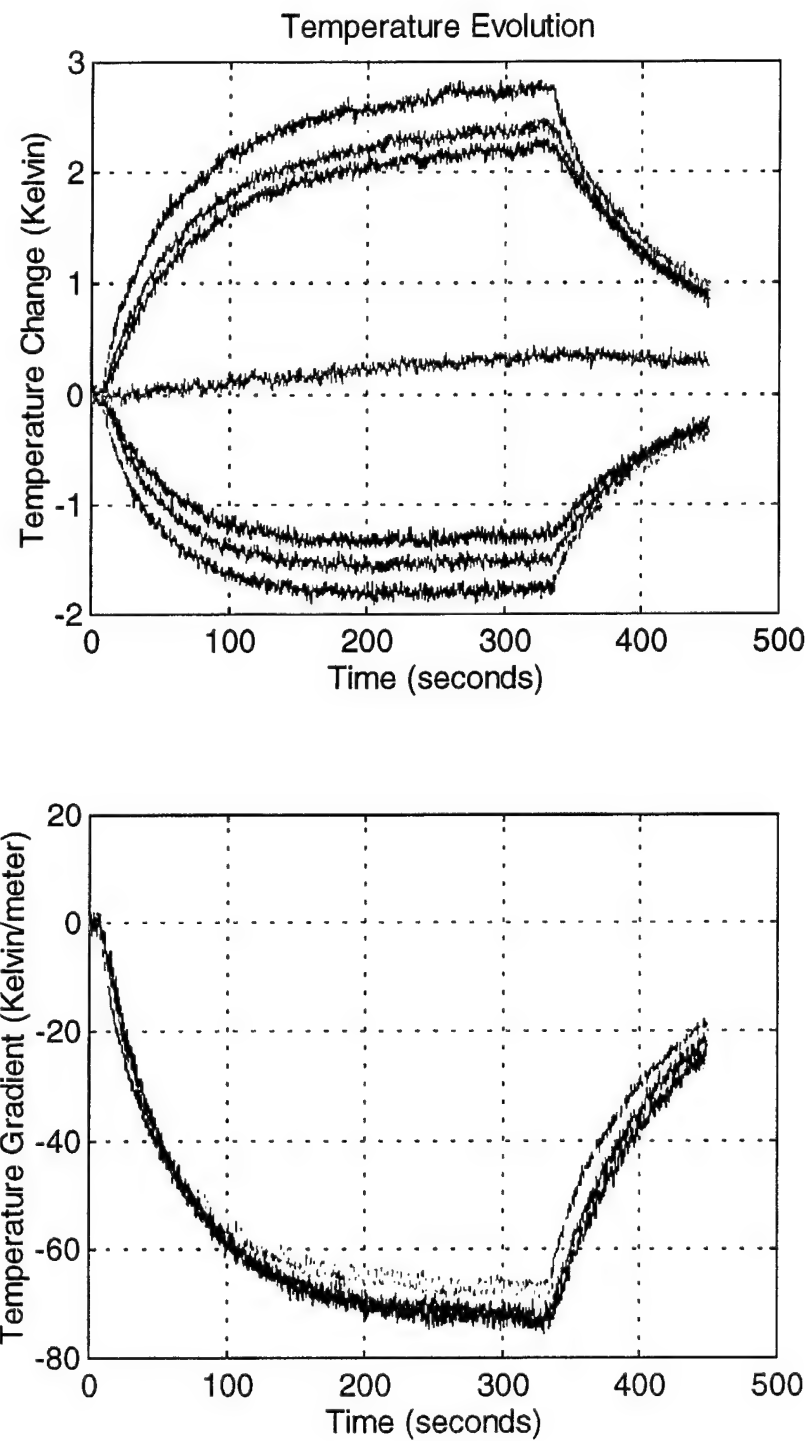
Temperature Evolution



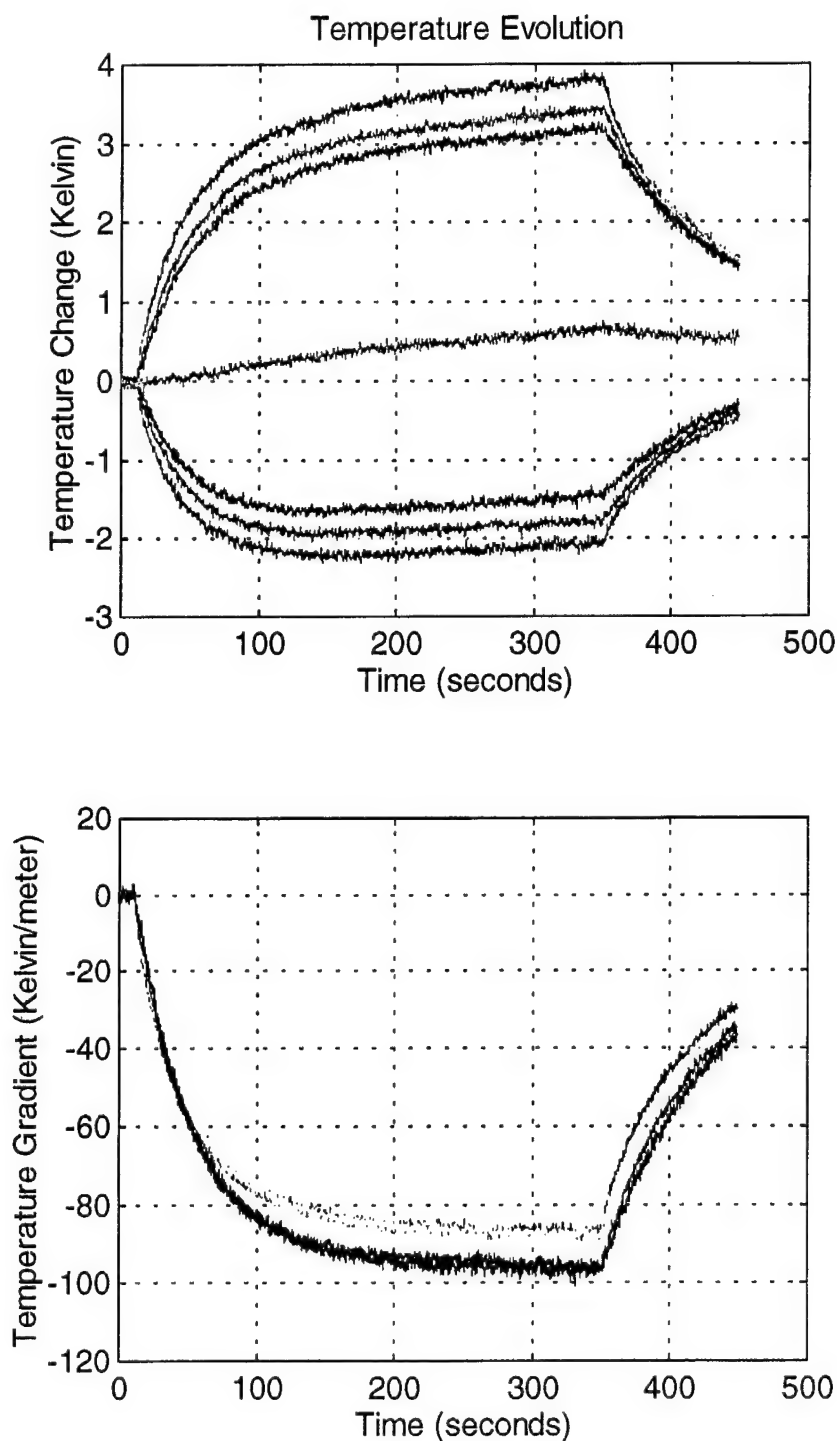
Run 2 2% drive ratio



Run 3 3% drive ratio

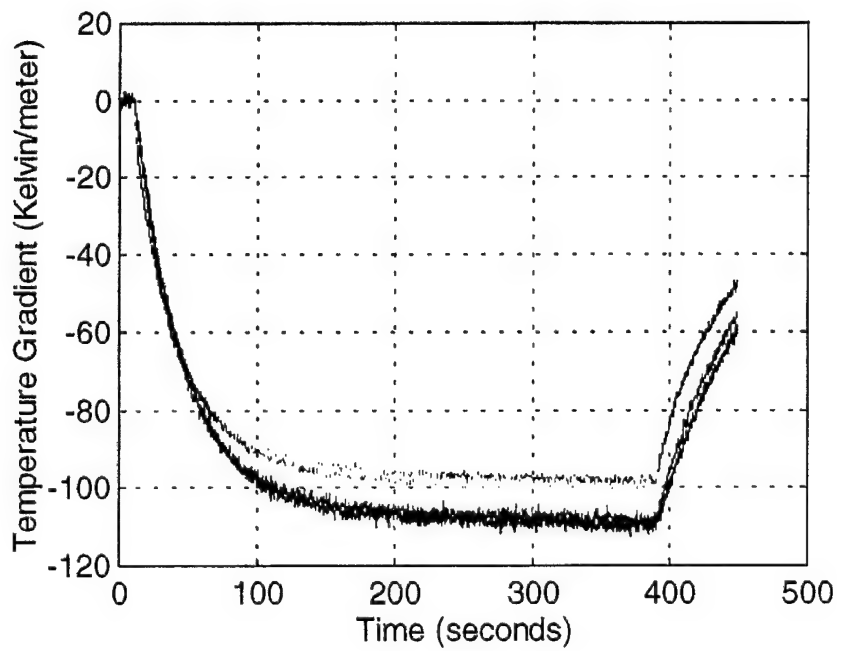
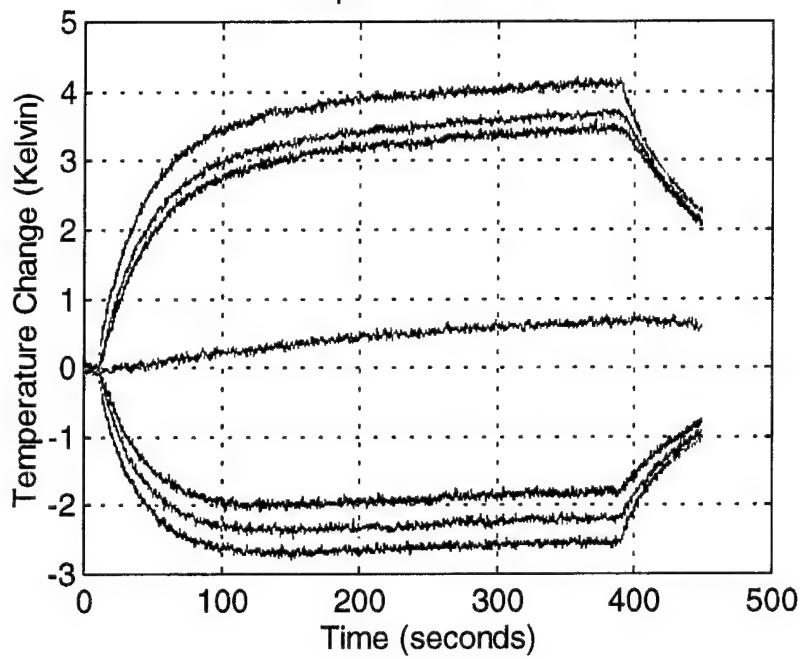


Run 4 4% drive ratio

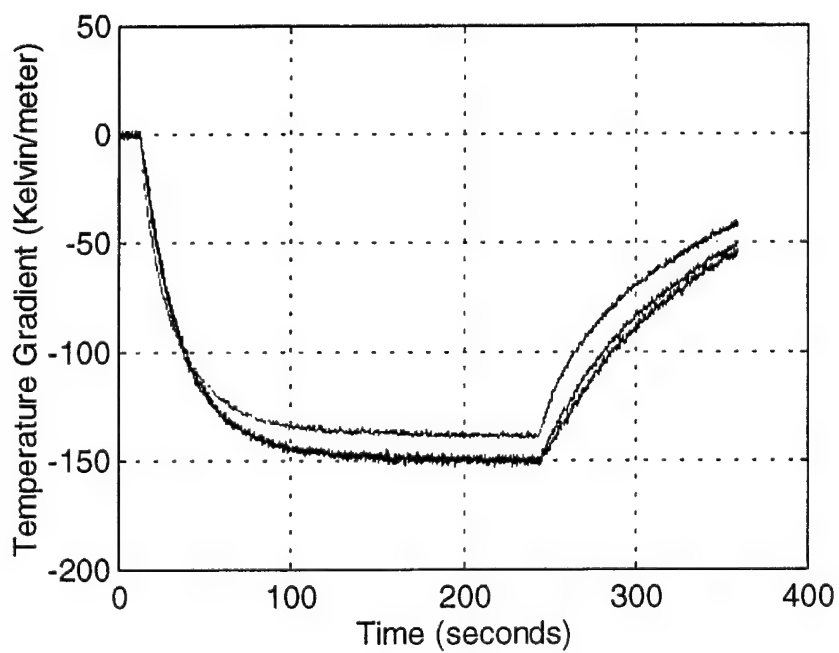
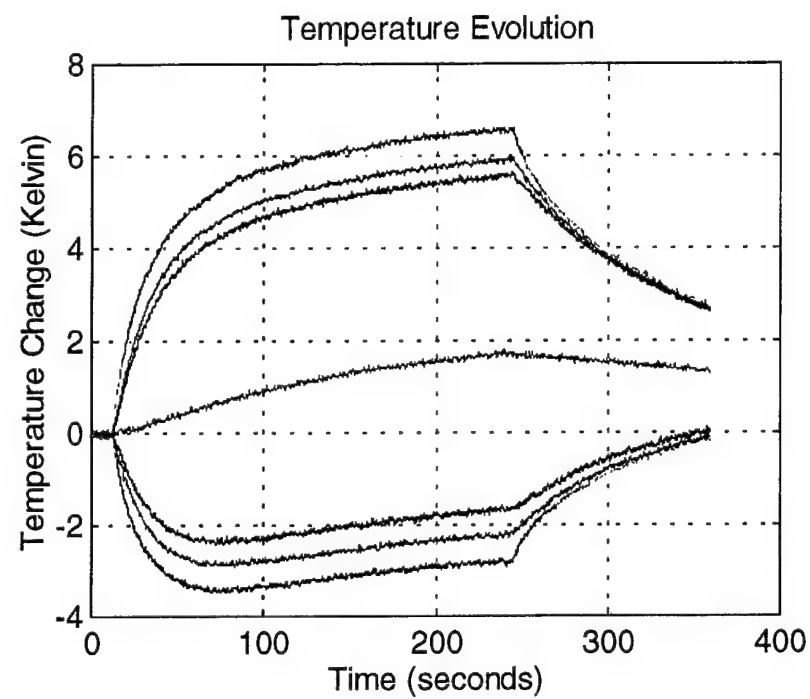


Run 5 5% drive ratio

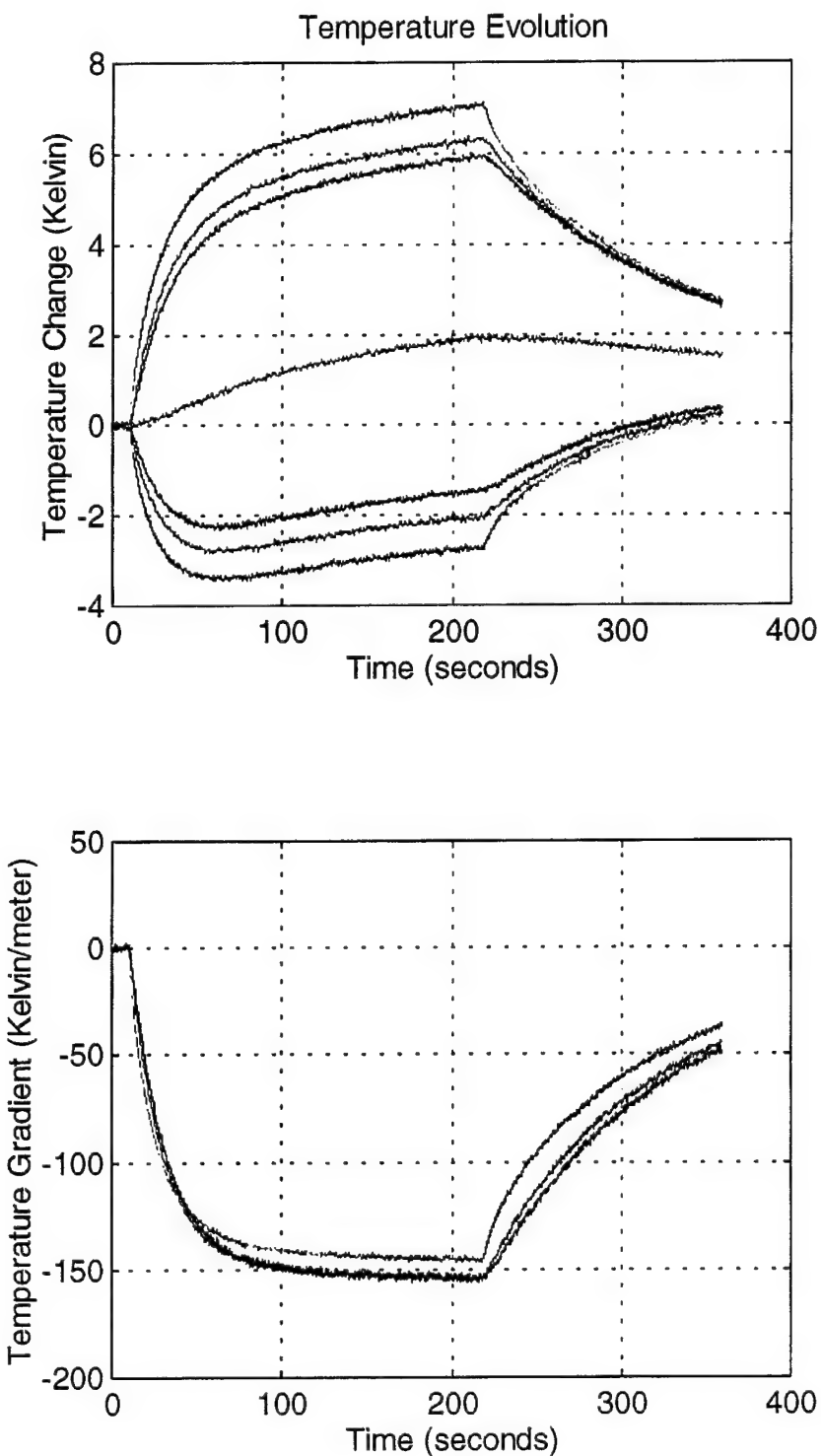
Temperature Evolution



Run 6 7% drive ratio



Run 7 11% drive ratio



Data Run Parameters

	P _{mean} (Pa)	T _{ref} (°C)	T _{wall} (°C)	F _o (Hz)	time/ point (sec/ point)	Drive ratio (%)	δ _k (mm)	δ _v (mm)	Disp amp (mm)
run 1	20300	21.7	22.4	78.45	0.1	0.905	.6487	.5281	2.622
run 2	21293	21.7	23.2	78.45	0.1	2.019	.6329	.5151	5.845
run 3	21632	21.8	23.7	78.45	0.1	3.063	.6289	.5119	8.884
run 4	21850	21.8	24.0	78.45	0.1	4.103	.6263	.5098	11.90
run 5	22163	21.9	24.3	78.45	0.1	4.764	.6225	.5067	13.87
run 6	20577	24.5	24.3	79.2	0.1	8.63	.659	.536	25.6
run 7	20951	24.4	24.4	79.2	0.1	10.90	.659	.536	32.9

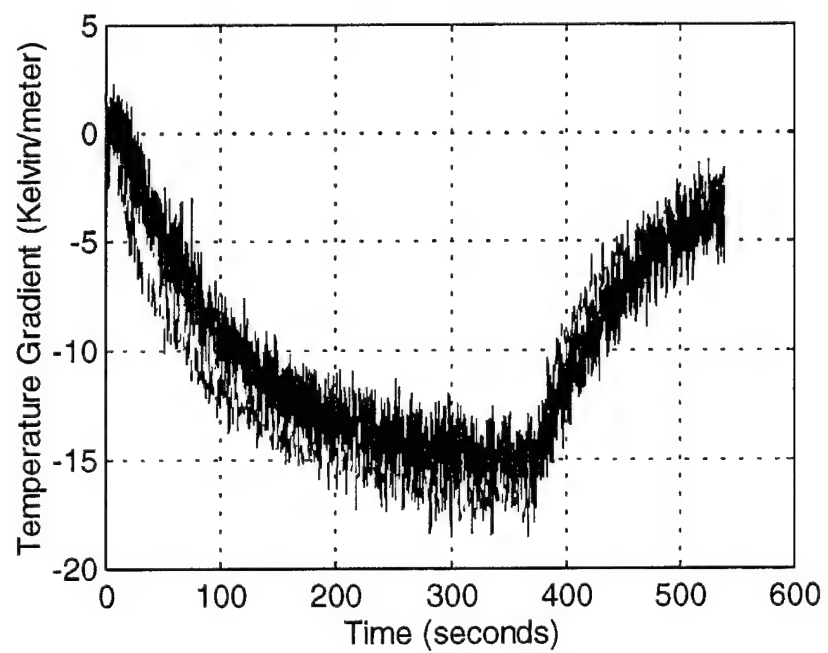
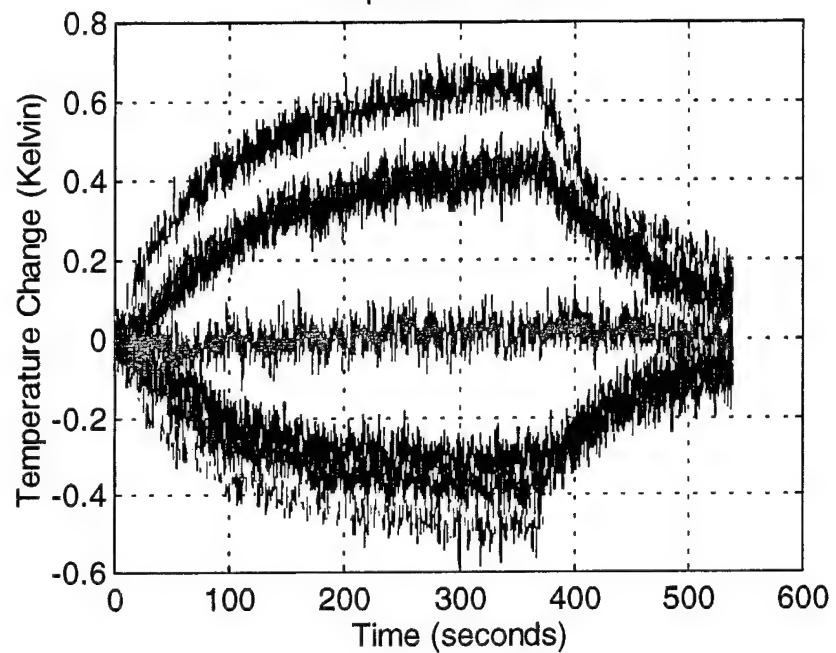
Temperature Gradient Steady State Values

	Red	error	Yellow	error	Green	error	Blue	error
run 1	-10.0	± 1.2	-9.0	± 1.5	-9.75	± 1.5	-10.0	± 2
run 2	-42.0	± 1.5	-42.0	± 1	-43.5	± 2	-42.5	± 2.25
run 3	-67.0	± 1	-68.0	± 1	-71.0	± 1.2	-72.5	± 1.2
run 4	-86.5	± 1.5	-87.5	± 1	-95.5	± 2	-96.5	± 2
run 5	-98.5	± 1	-99.5	± 1.5	-107.5	± 1	-109.5	± 1.5
run 6	-139.0	± 1.2	-141.2	± 1.2	-149.5	± 1.5	-150.5	± 1.5
run 7	-145.0	± 1.2	-147.5	± 1	-154.0	± 2	-153.5	± 2.5

APPENDIX D. ARGON AT 5PSI A POSITIONED HALFWAY BETWEEN PRESSURE AND VELOCITY NODES.

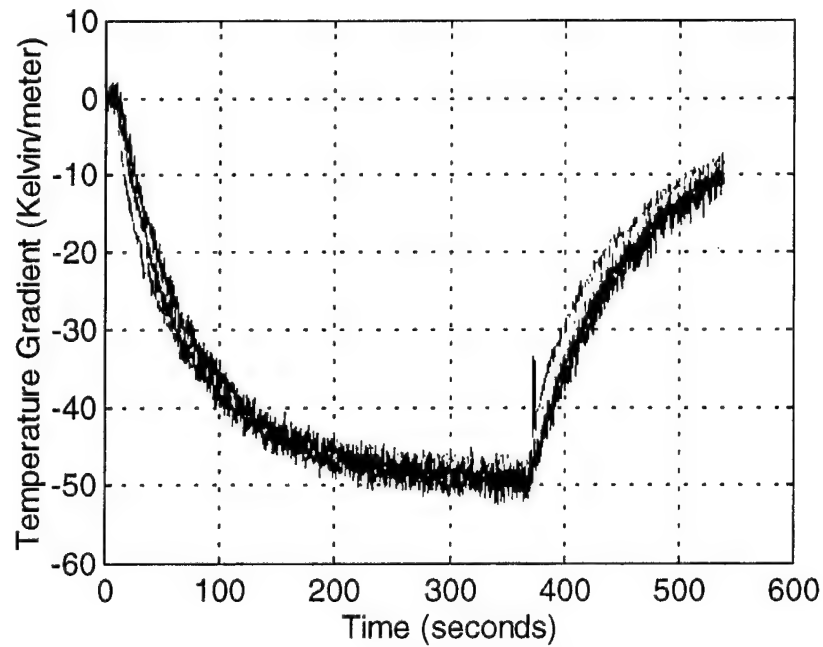
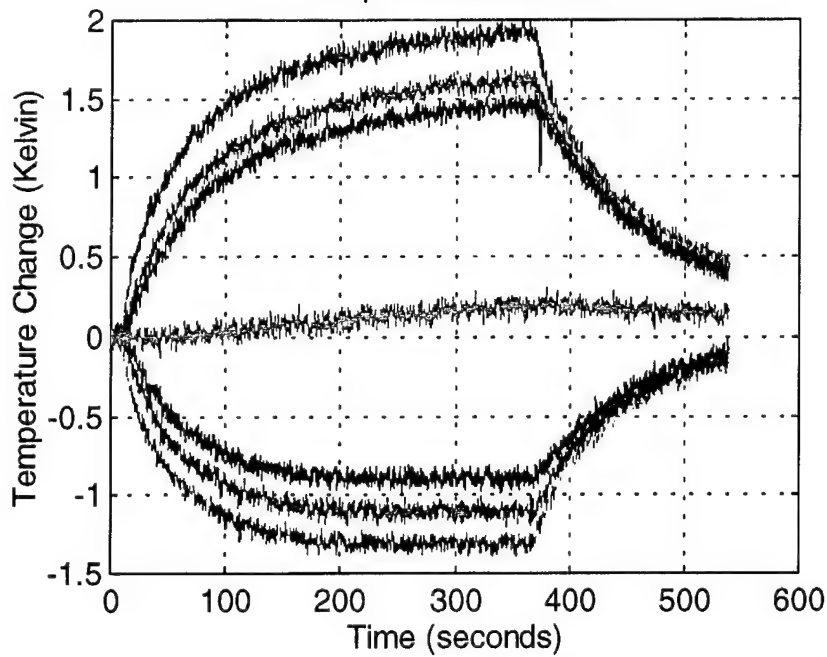
Run 1 1% drive ratio

Temperature Evolution



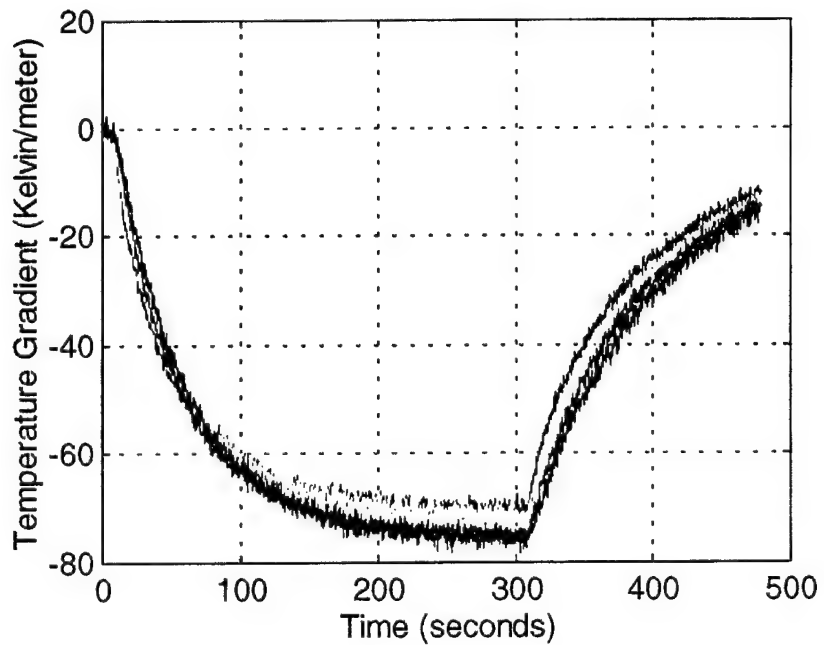
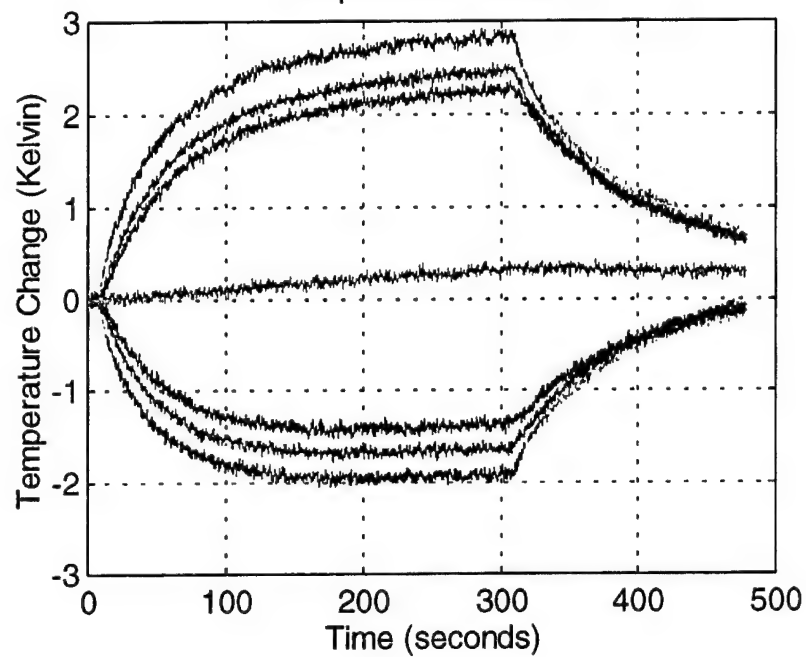
Run 2 2% drive ratio

Temperature Evolution



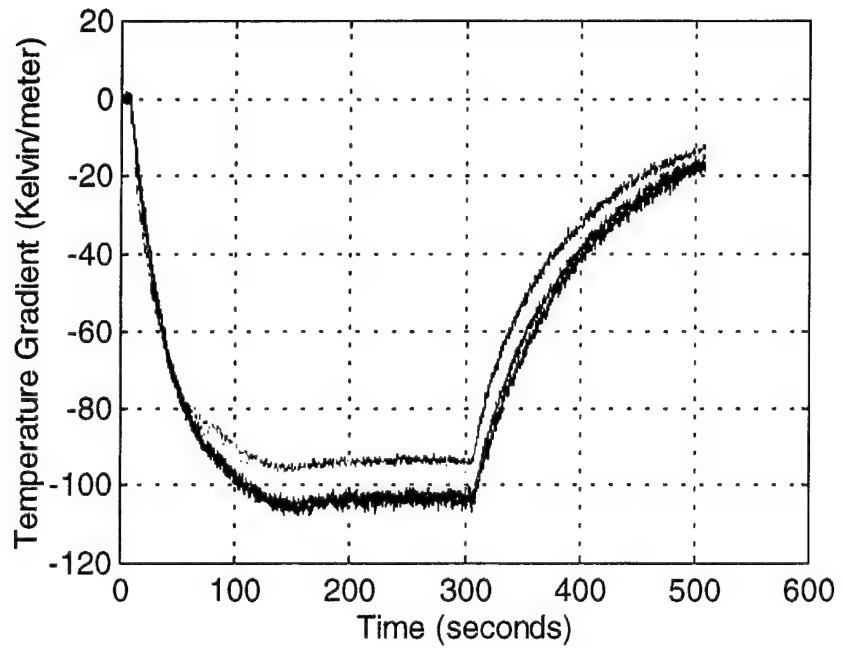
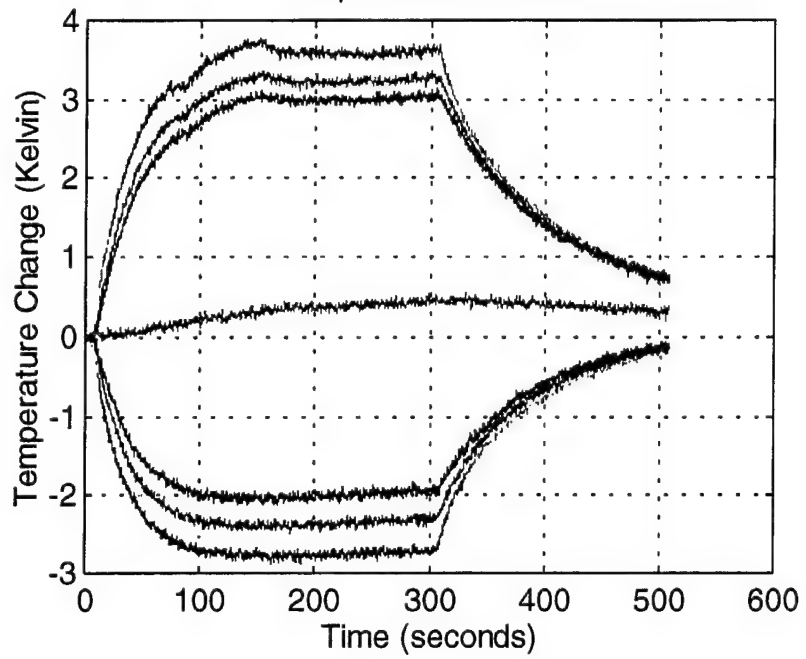
Run 3 3% drive ratio

Temperature Evolution

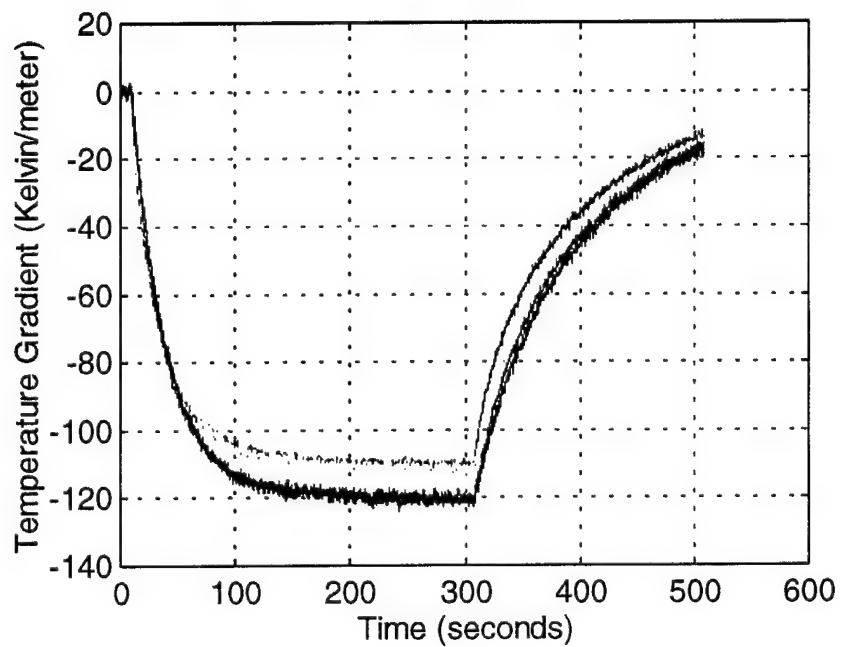
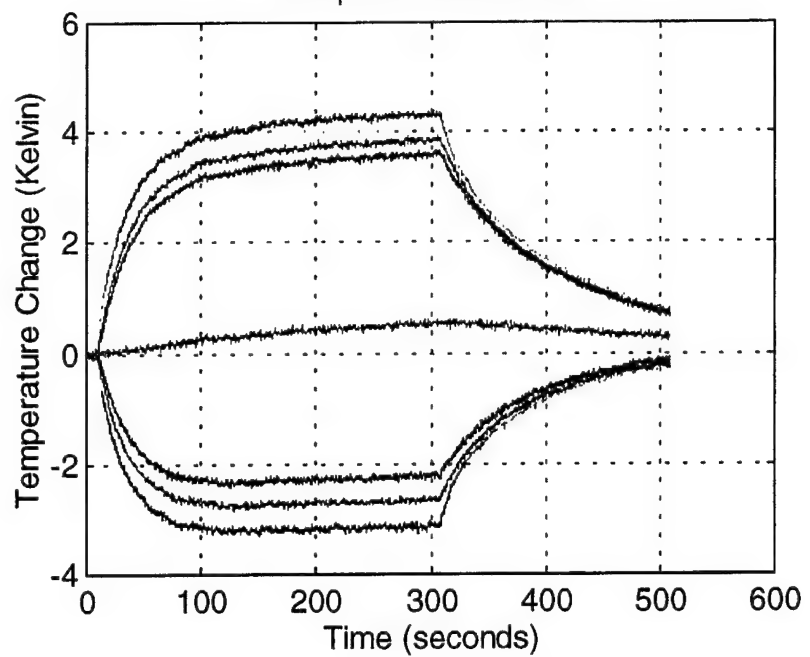


Run 4 4% drive ratio

Temperature Evolution



Run 5 5% Drive Ratio
Temperature Evolution



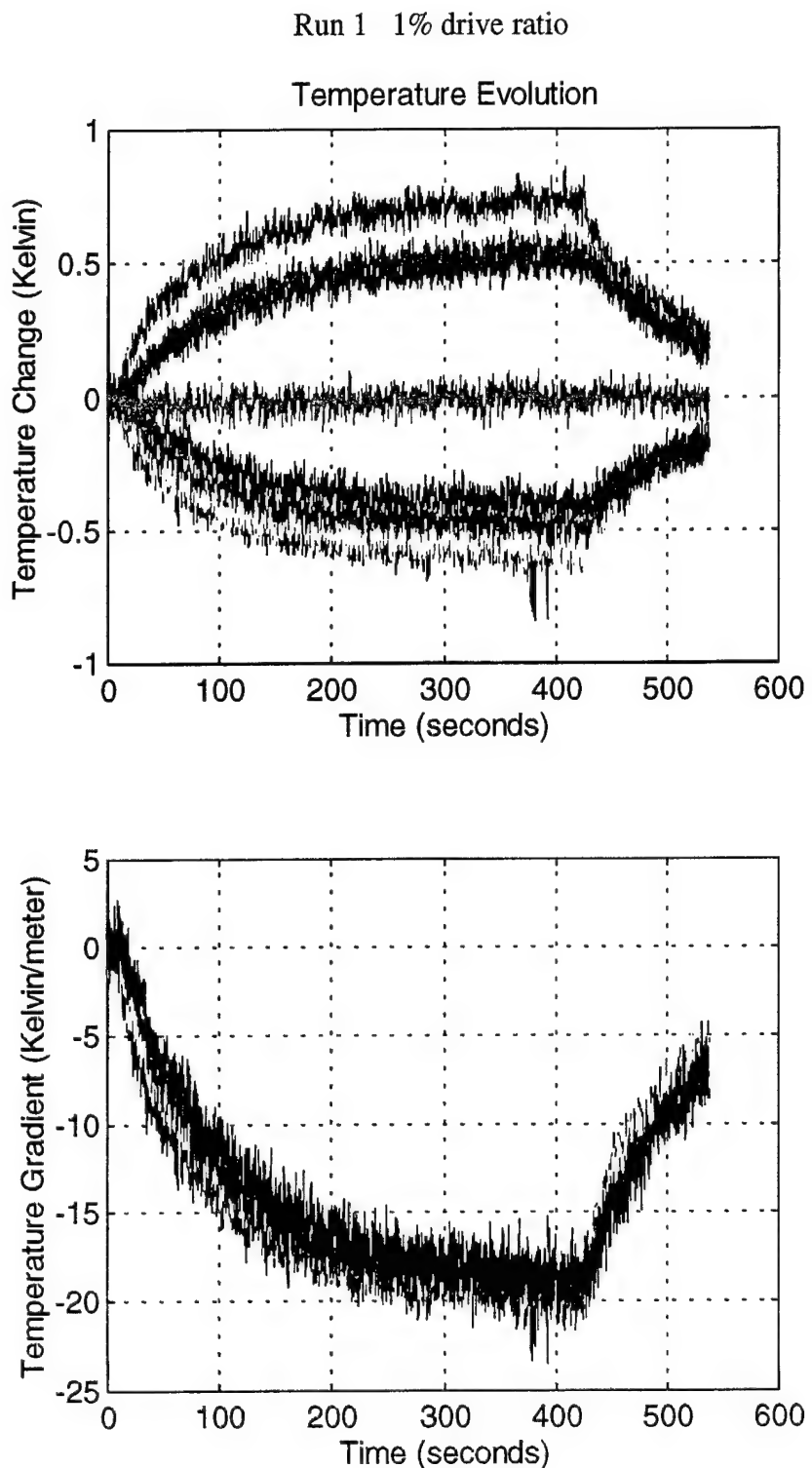
Data Run Parameters

	P _{mean} (Pa)	T _{ref} (°C)	T _{wall} (°C)	F _o (Hz)	time/ point (sec/ point)	δ _k (mm)	δ _v (mm)	Drive ratio (%)	Disp amp (mm)
run 1	39406	23.1	22.8	79.9	0.1	.460	.375	956	2.6
run 2	39714	23.0	24.0	79.9	0.1	.460	.375	2.05	5.6
run 3	36719	22.5	21.6	79.8	0.1	.476	.387	2.85	7.7
run 4	38282	25.8	26.5	80.29	0.1	.469	.381	3.99	10.8
run 5	38745	25.7	26.8	80.29	0.1	.466	.381	4.62	12.7

Temperature Gradient Steady State Values

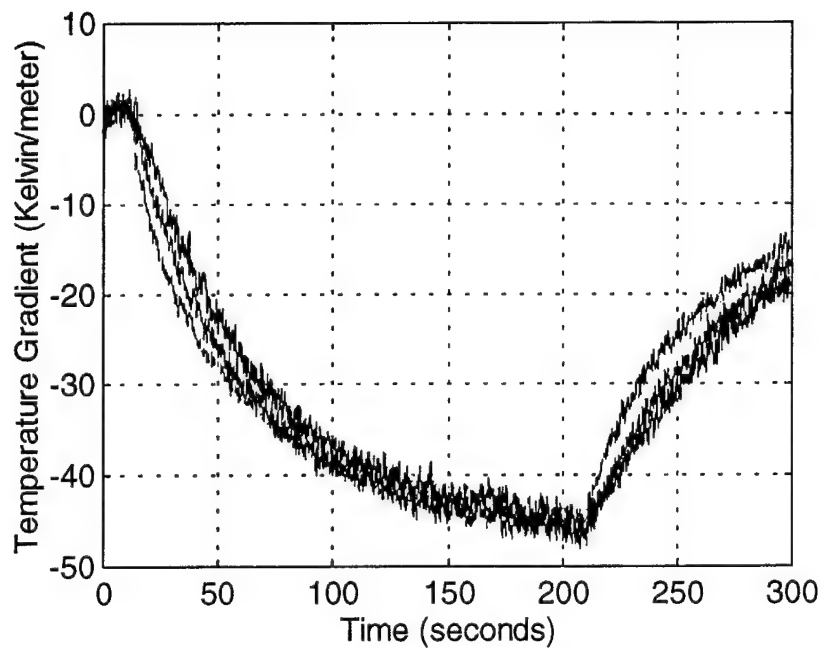
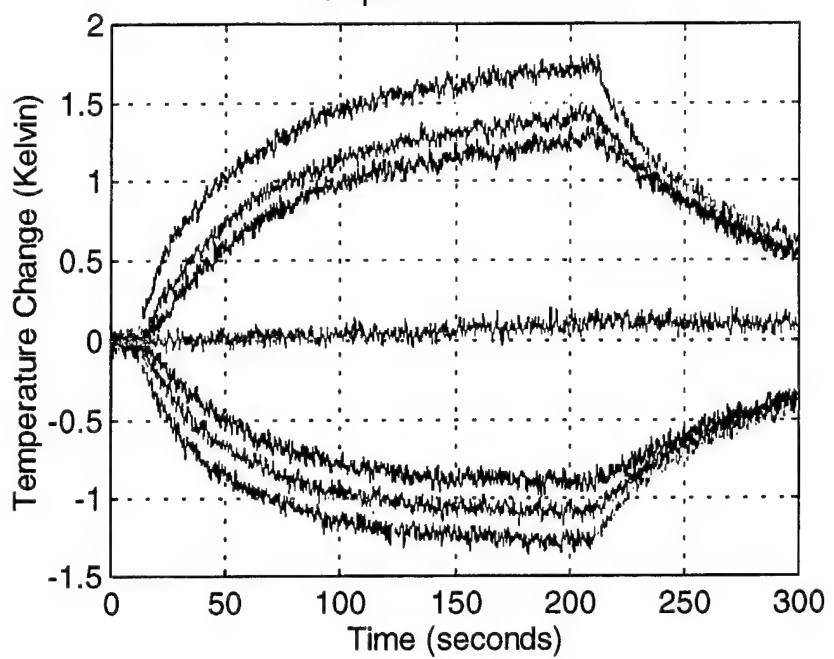
	Red	error	Yellow	error	Green	error	Blue	error
run 1	-16.6	± 0.6	-16.0	± 0.9	-15.5	± 0.5	-15.0	± 1.2
run 2	-47.5	± 1	-48.0	± 1.5	-49.0	± 1.8	-50.0	± 1.8
run 3	-70.5	± 1.5	-71.5	± 1	-76.0	± 2.5	-75.5	± 1
run 4	-94.5	± .5	-96.0	± 1.5	-102.5	± 2	-103.5	± 2.2
run 5	-110.5	± 0.75	-112.5	± 1.5	-120.0	± 1	-121.5	± 1.25

**APPENDIX E. ARGON AT 10 PSIA, POSITIONED HALFWAY BETWEEN
PRESSURE AND VELOCITY NODES**



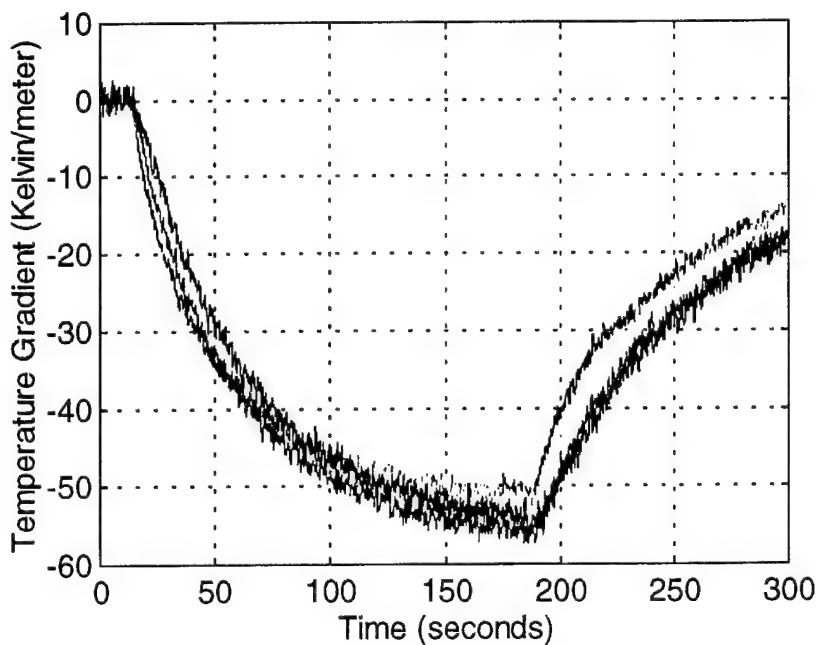
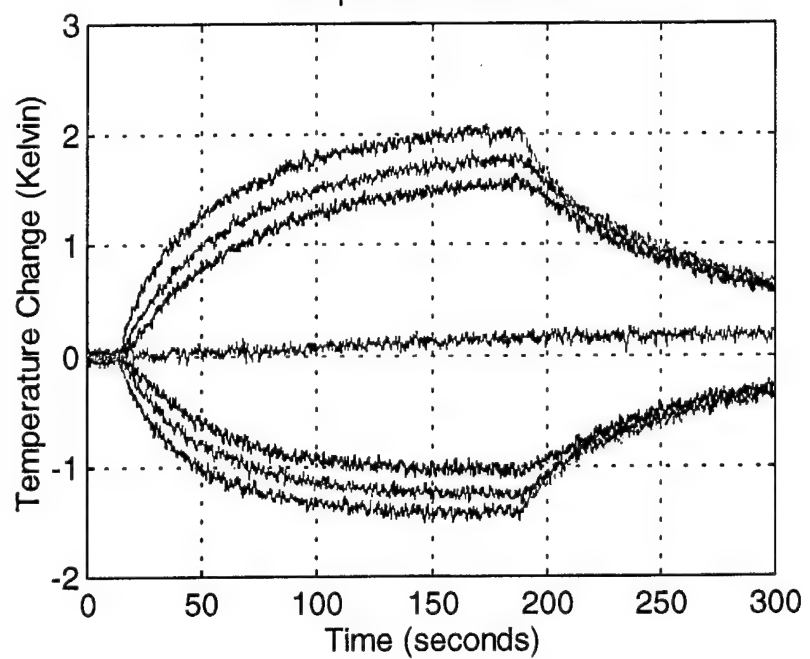
Run 2 2% drive ratio

Temperature Evolution



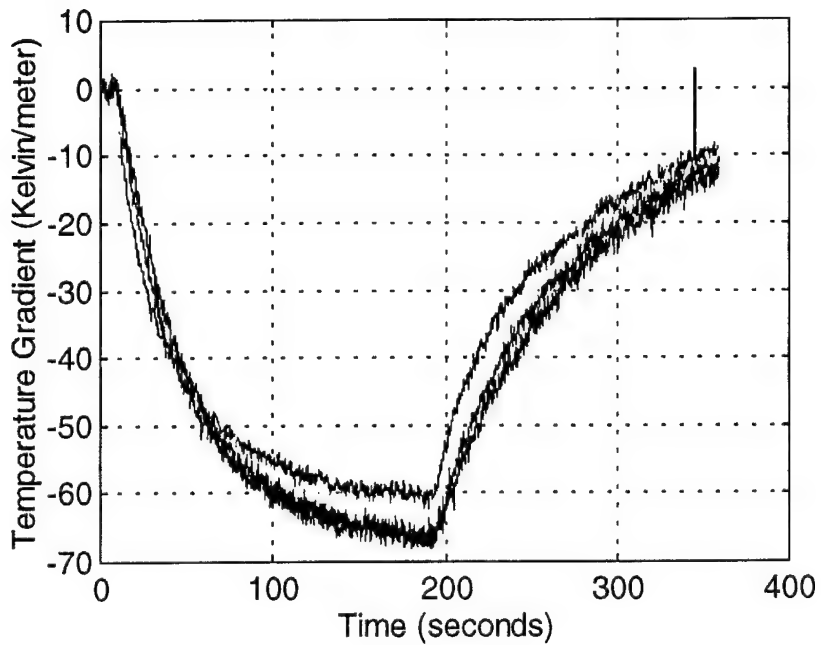
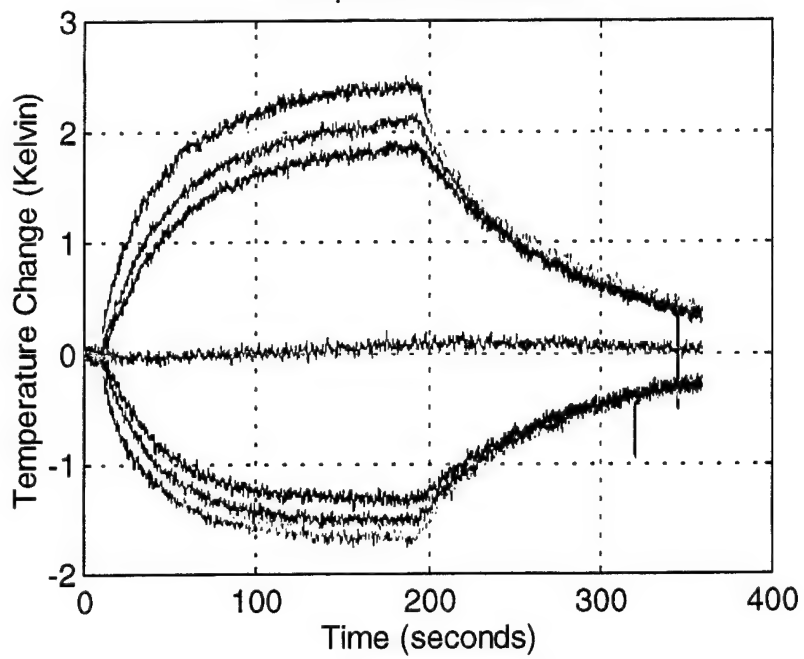
Run 3 2.3% drive ratio

Temperature Evolution

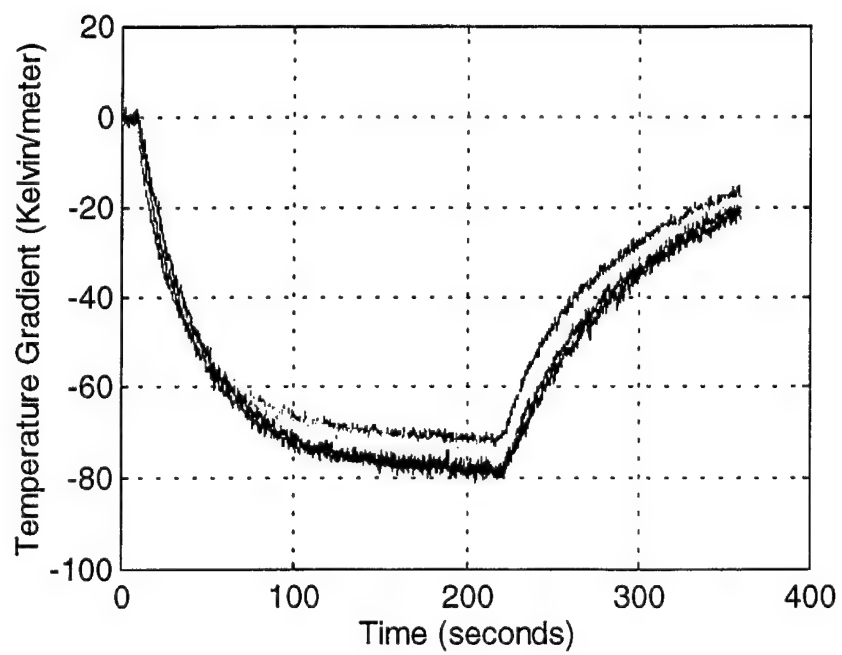
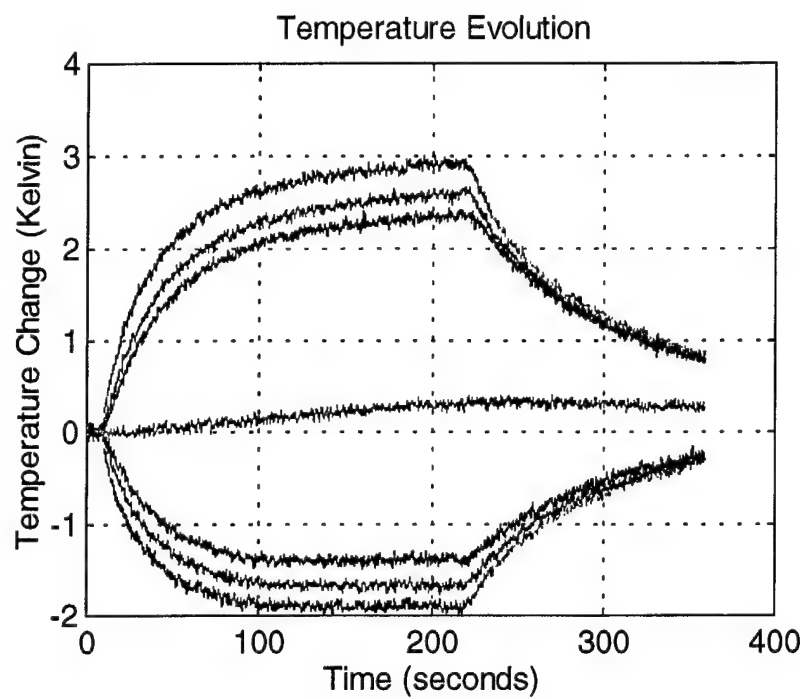


Run 4 2.5% drive ratio

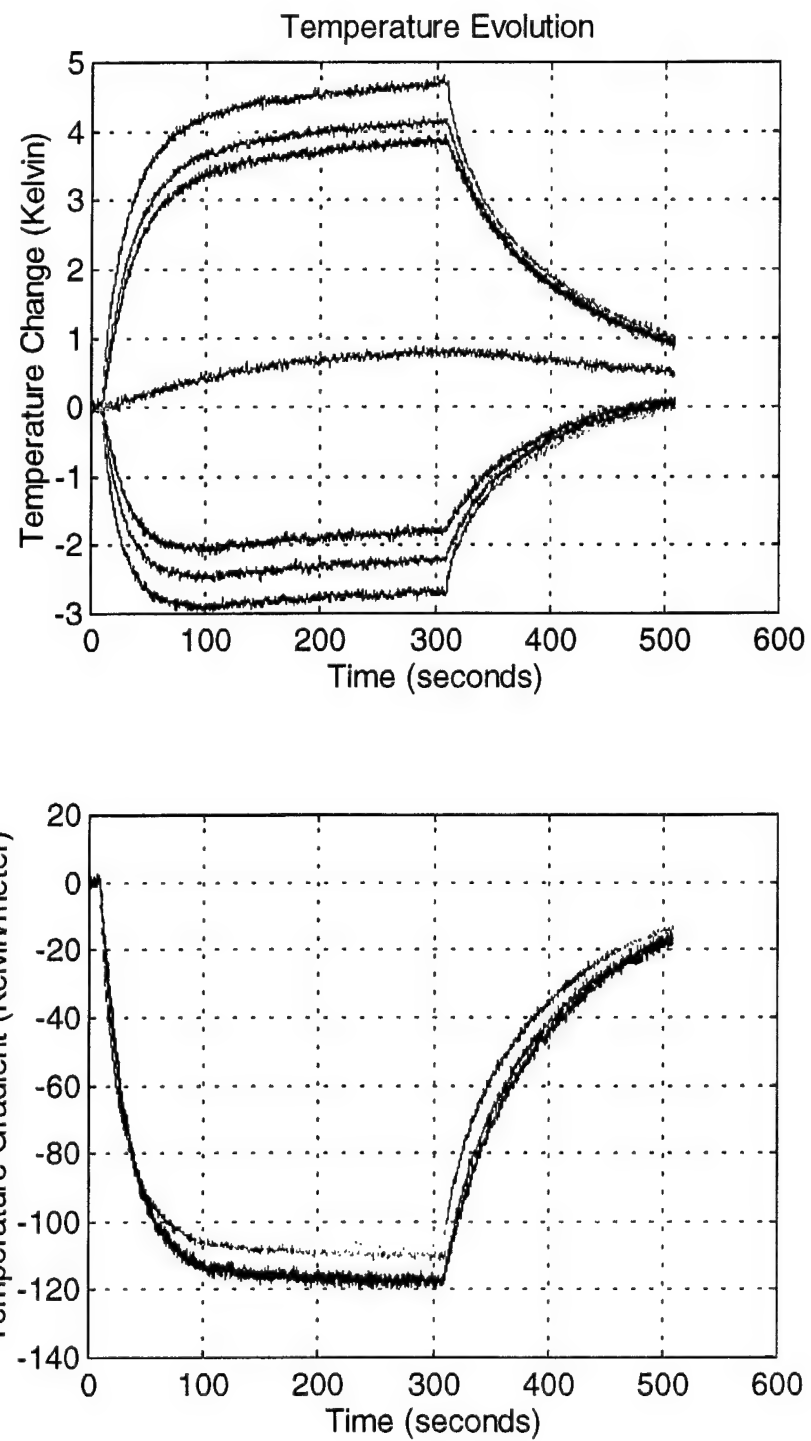
Temperature Evolution



Run 5 3% drive ratio

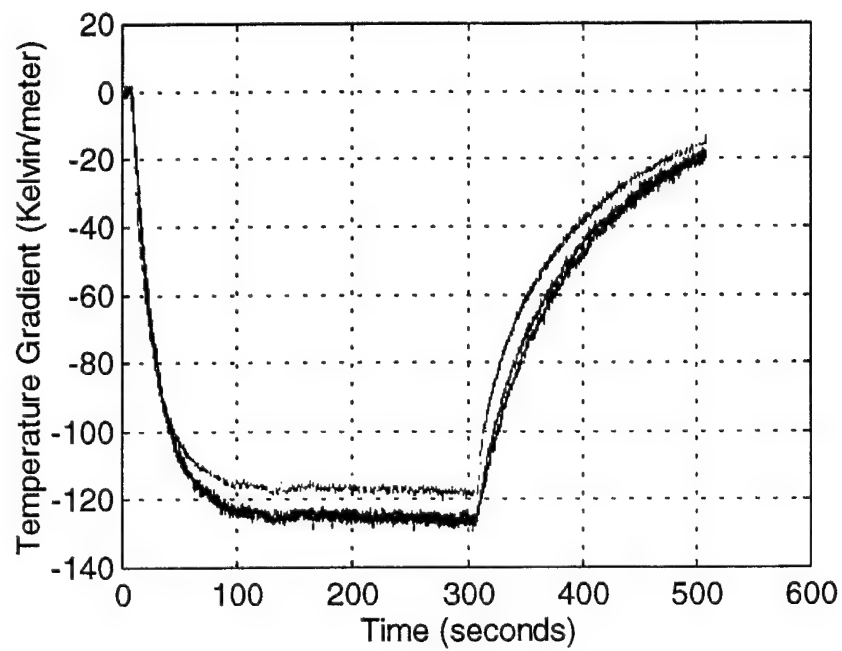
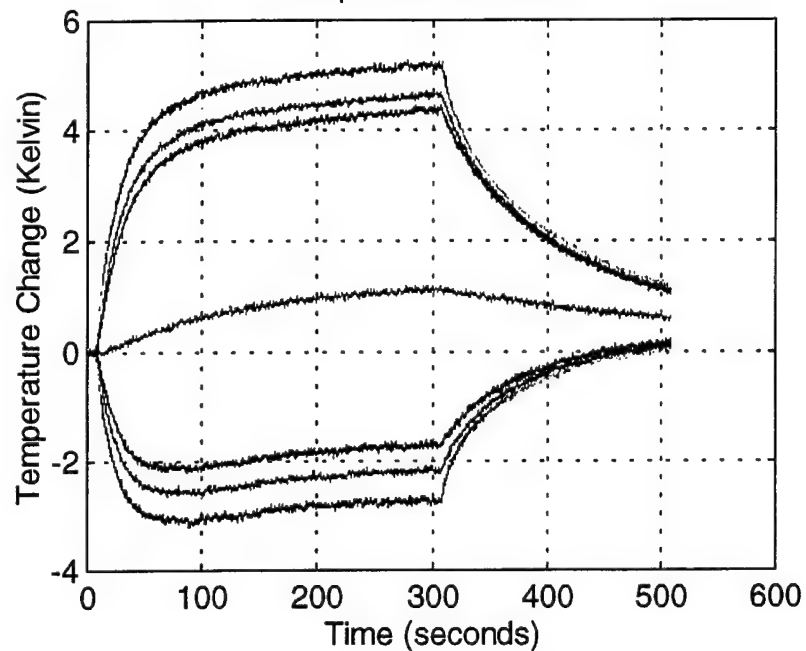


Run 6 4% drive ratio

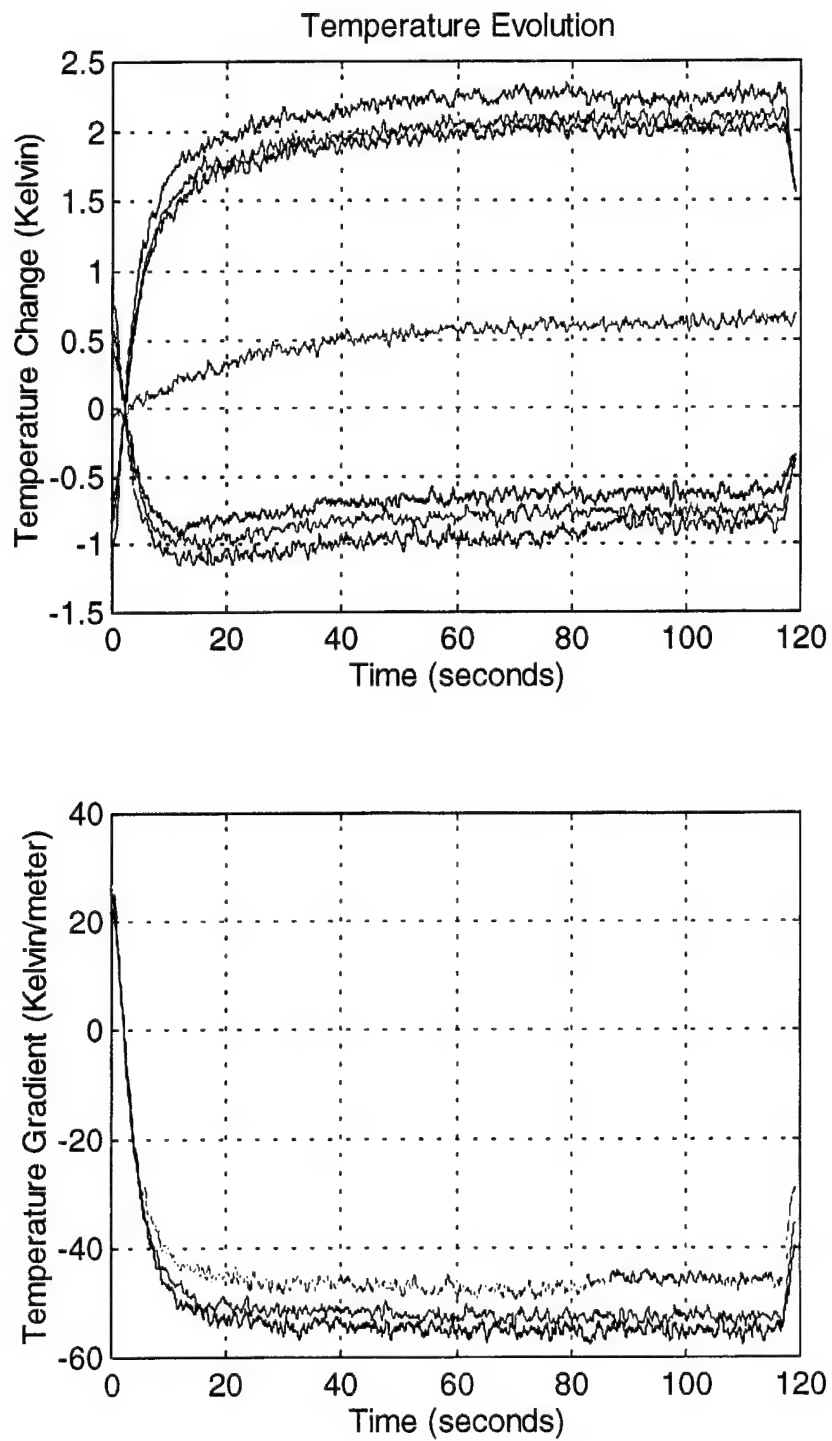


Run 7 5% Drive Ratio

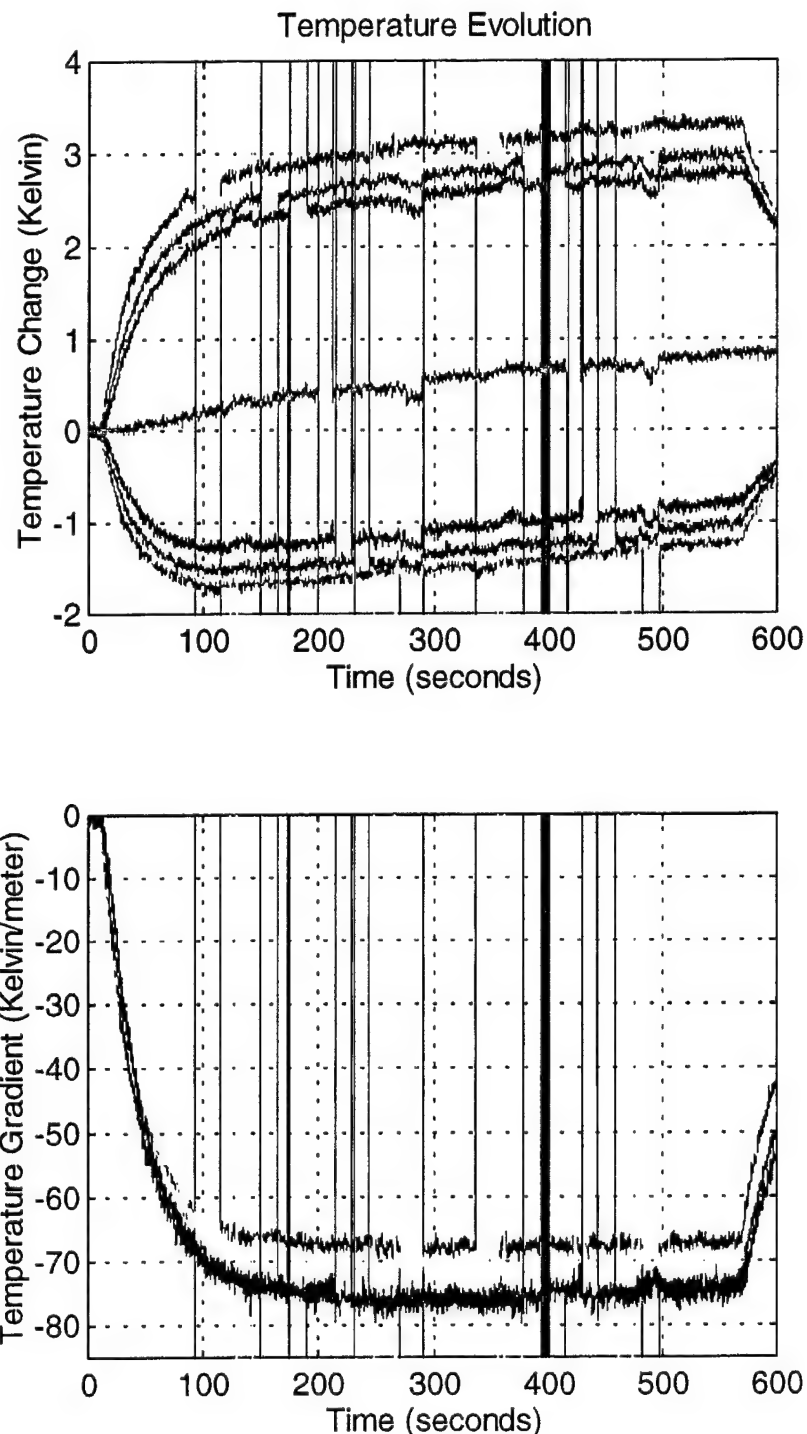
Temperature Evolution



Run 8 3% drive ratio, run for 20 min

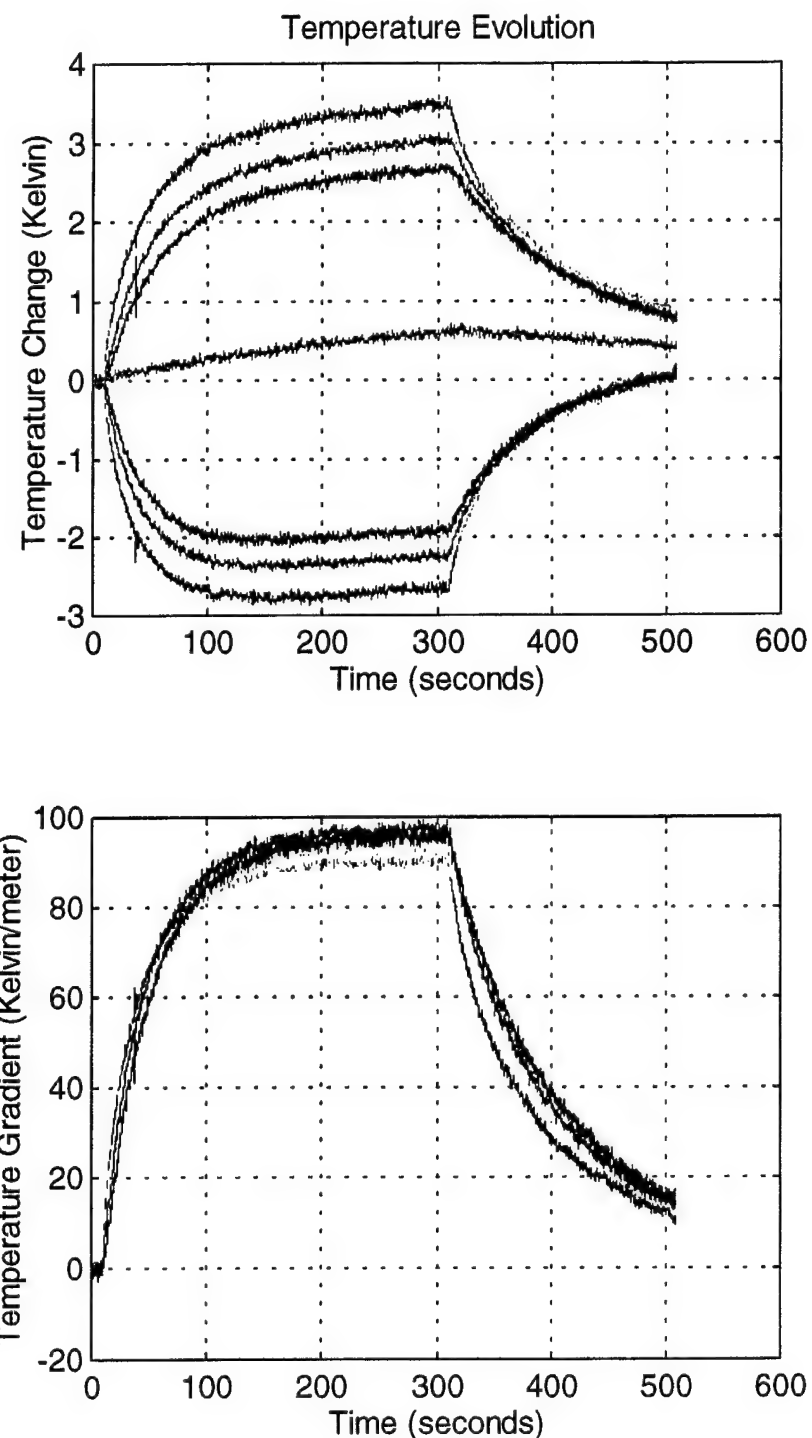


Run 9 3% drive ratio, True temps taken

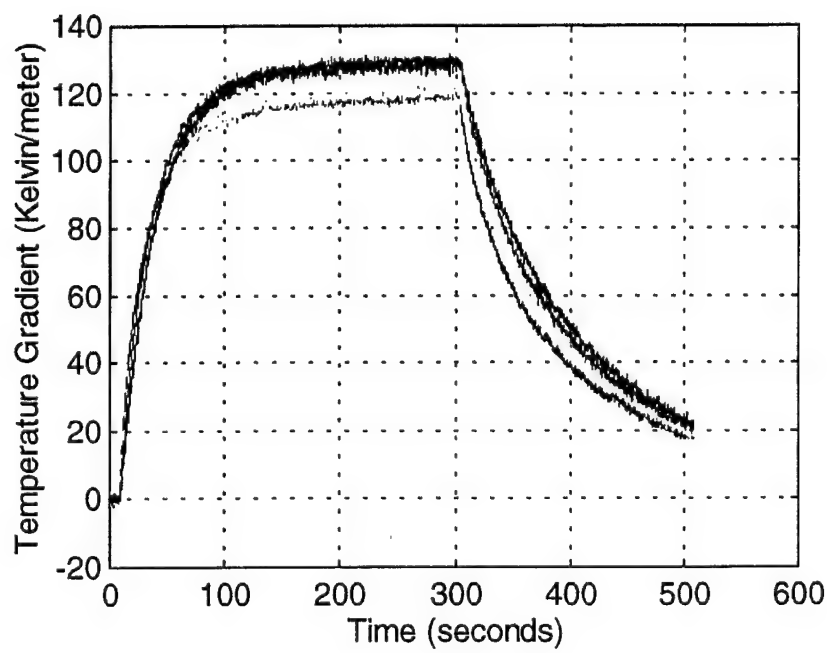
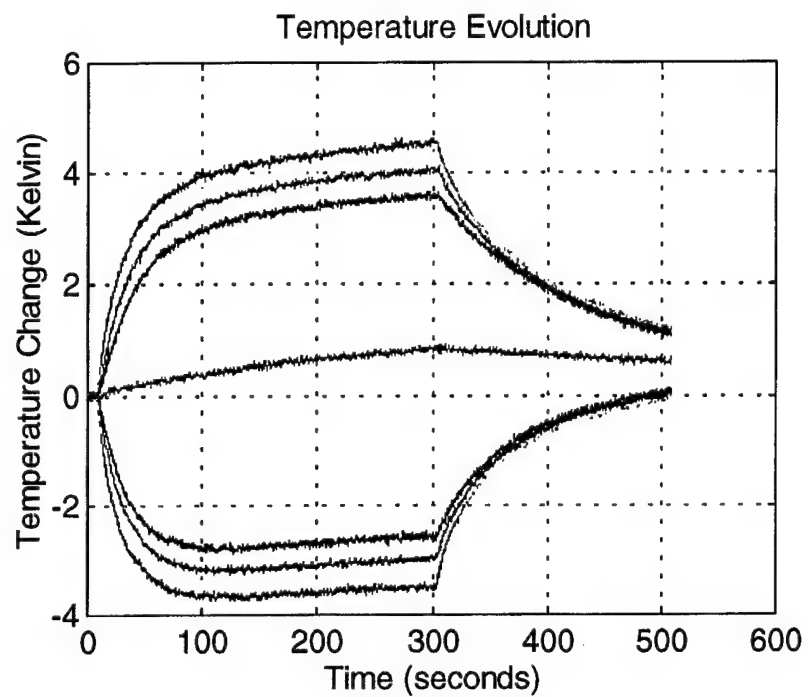


Note: Throughout this data run the thermocouples were disconnected from the computer briefly and measured with a hand held thermocouple thermometer. During the disconnect the values went to infinity.

Run 10 4% drive ratio, 3rd frequency mode



Run 11 5% drive ratio, 3rd frequency mode



Data Run Parameters

	P _{mean} (Pa)	T _{ref} (°C)	T _{wall} (°C)	F _o (Hz)	time/ point (sec/ point)	δ _k (mm)	δ _v (mm)	Drive ratio (%)	Disp amp (mm)
run 1	69751	24.2	24.3	79.8	0.1	.348	.283	.9445	2.6
run 2	69384	25.4	26.4	80.29	0.1	.350	.285	1.868	5.1
run 3	69839	24.3	24.6	80.79	0.1	.346	.282	2.148	5.7
run 4	69355	24.5	24.7	80.79	0.1	.347	.283	2.470	6.5
run 5	69540	26.4	25.4	80.29	0.1	.350	.285	2.994	8.1
run 6	69641	26.8	25.4	80.29	0.1	.349	.284	4.369	11.9
run 7	69817	26.6	25.4	80.29	0.1	.349	.283	4.983	13.5
run 8	68840	23.0	24.1	79.89	1.0	.350	.285	3.046	8.35
run 9	68741	23.5	24.2	79.9	0.1	.350	.285	2.99	8.2
run 10	68694	25.2	25.6	131.19	0.1	.274	.224	3.665	-5.5
run 11	69267	24.6	25.9	131.19	0.1	.274	.223	4.827	-7.3

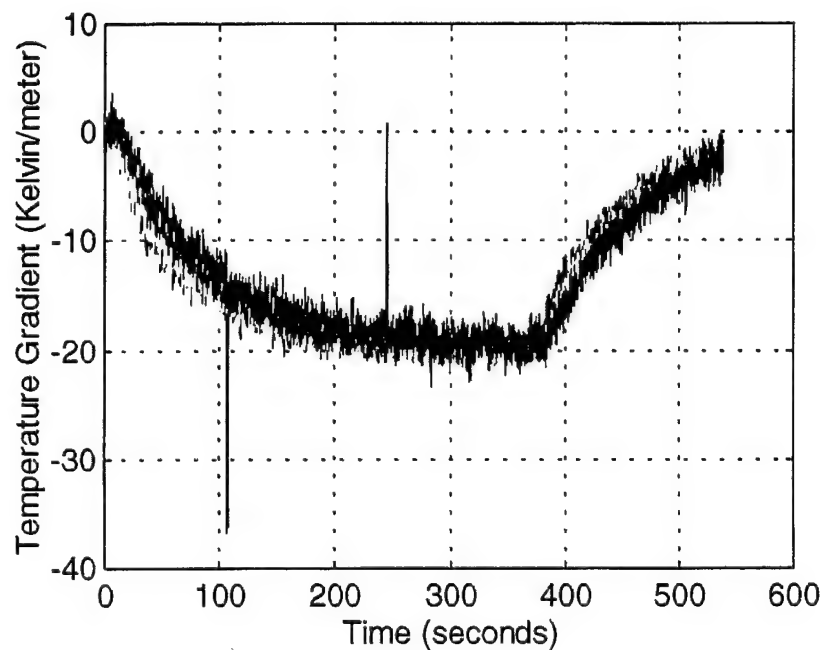
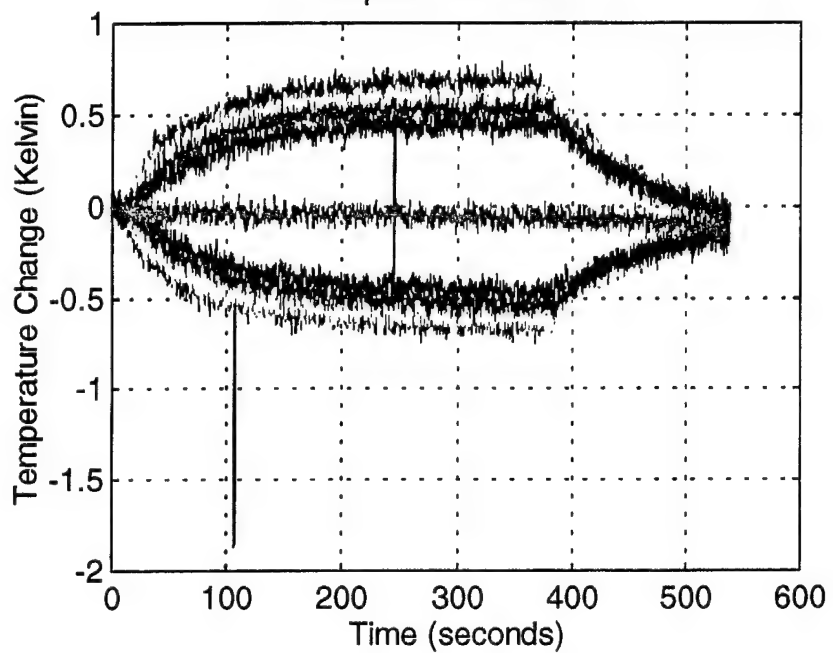
Temperature Gradient Steady State Values

	Red	error	Yellow	error	Green	error	Blue	error
run 1	-19.2	± 1	-19.1	± 1	-19.1	± 1.2	-19.0	± 1.3
run 2	-44.3	± .8	-44.4	± .7	-46.0	± 1.0	-46.0	± 1.2
run 3	-50.8	± 1.3	-51.5	± 1	-56.0	± 1.5	-54.0	± 2
run 4	-61.0	± 1	-63.2	± 1	-67.3	± .7	-66.0	± 1
run 5	-71.5	± 1.5	-73.2	± 1.2	-78.0	± 2	-78.0	± 2
run 6	-110.0	± 1	-108.0	± 1.5	-117.5	± 1	-118	± 1.5
run 7	-118.0	± 1	-118.0	± 1	-126.0	± 1	-126.5	± 1.5
run 8	-46.0	± 1	-47.0	± .75	-52.5	± 1	-55.0	± 1.5
run 9	-68.0	± 1	-69.0	± 1.2	-74.0	± 2	-75.0	± 2
run 10	-91.0	± 1	-91.2	± 1	-97.0	± 1	-95.8	± 1.2
run 11	-119.5	± 1.5	-120.3	± 1	-129.5	± 1.5	-128.5	± 1.5

**APPENDIX F. ARGON AT 18 PSIA, POSITIONED HALFWAY BETWEEN
PRESSURE AND VELOCITY NODES**

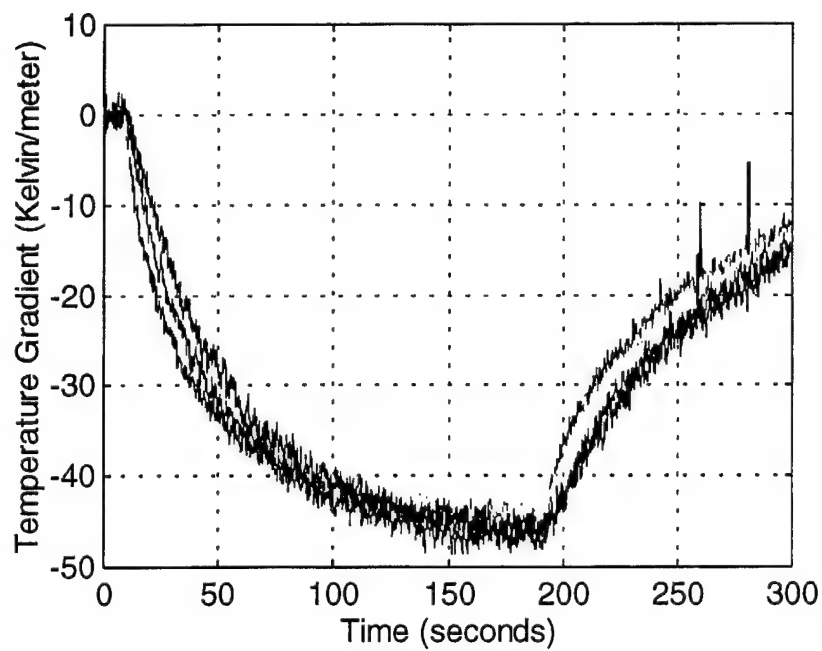
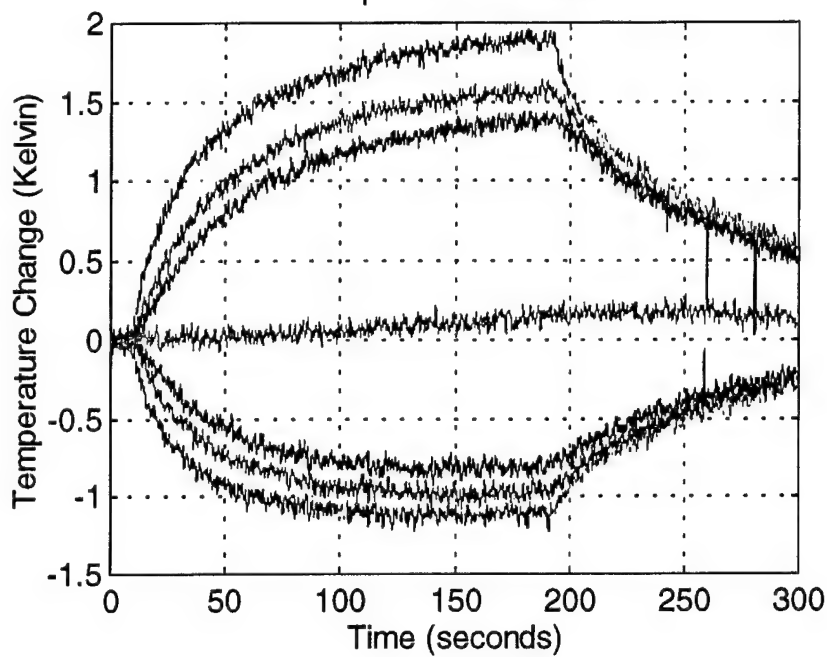
Run 1 1% drive ratio

Temperature Evolution



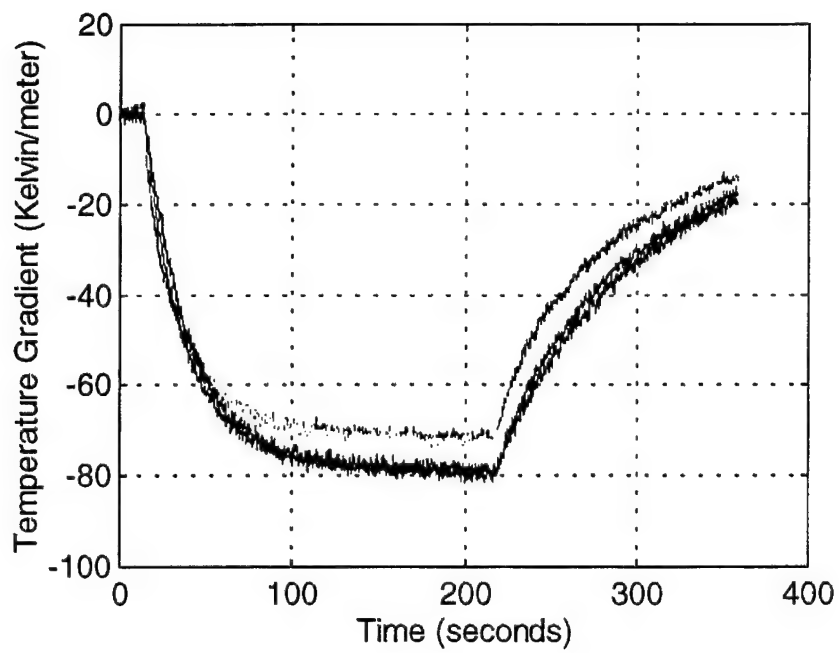
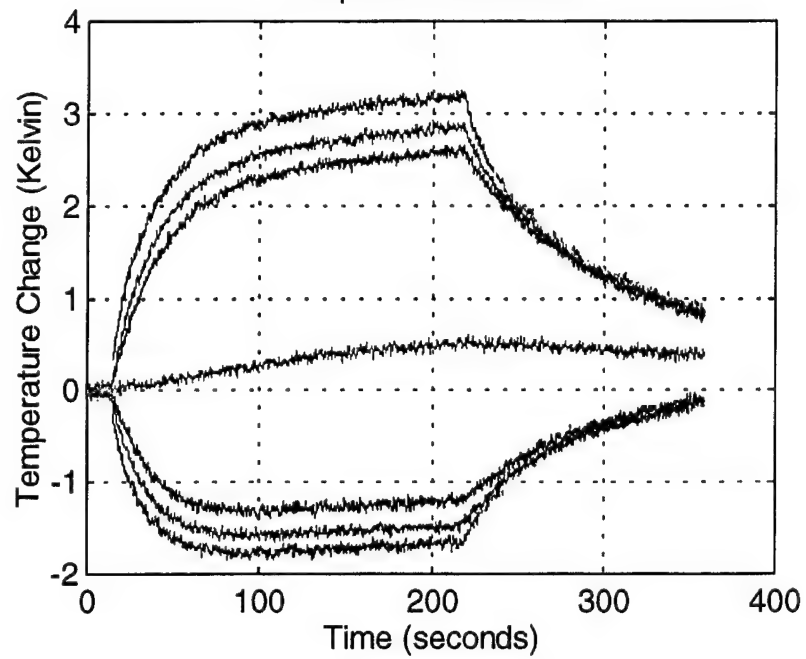
Run 2 2% drive ratio

Temperature Evolution

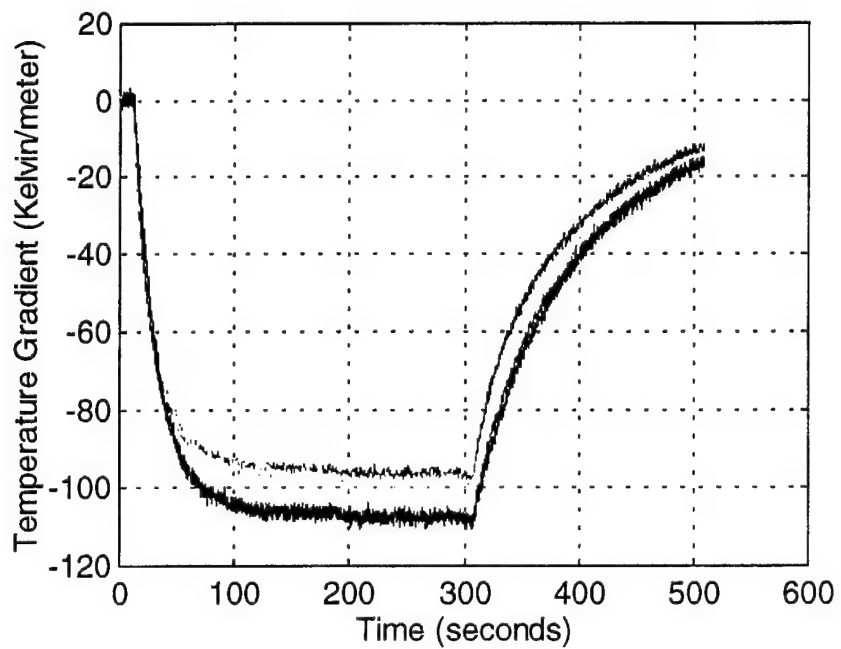
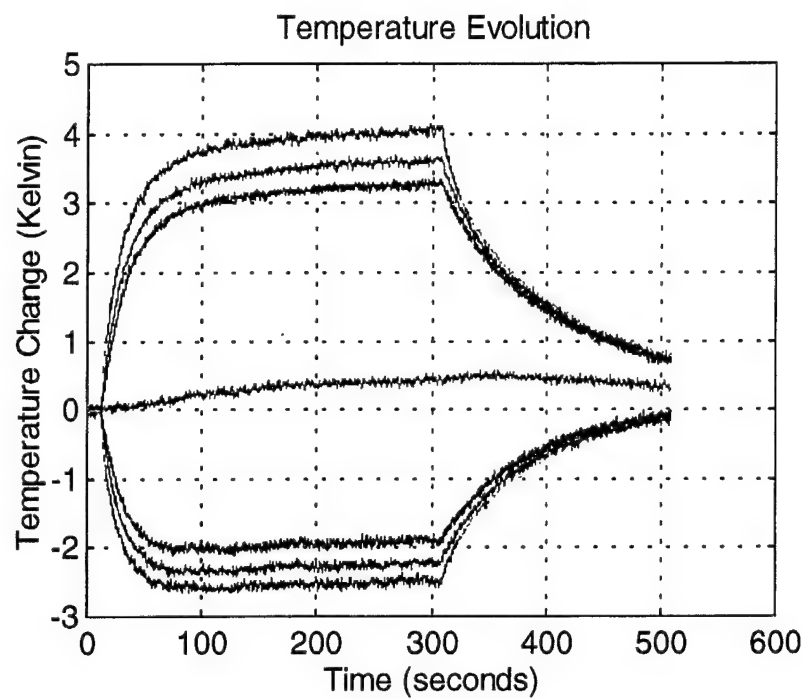


Run 3 3% drive ratio

Temperature Evolution



Run 4 4% drive ratio



Data Run Parameters

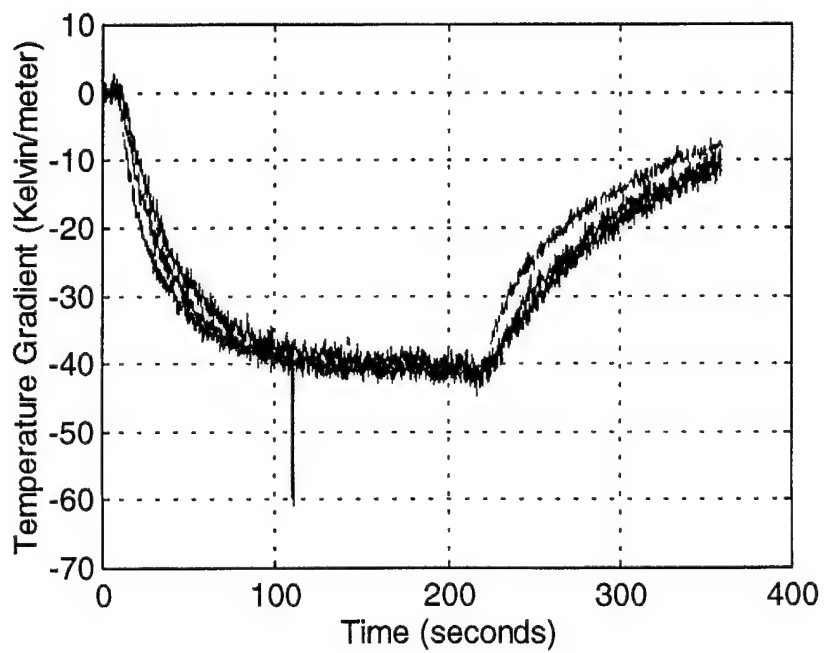
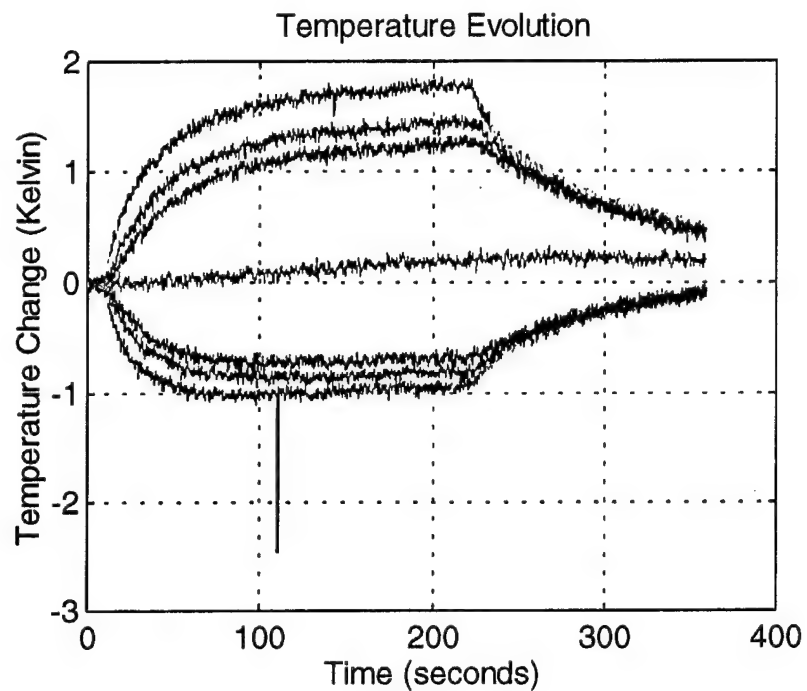
	P _{mean} (Pa)	T _{ref} (°C)	T _{wall} (°C)	F _o (Hz)	time/ point (sec/ point)	δ _k (mm)	δ _v (mm)	Drive ratio (%)	Disp amp (mm)
run 1	121370	24.6	23.3	79.9	0.1	.263	.214	.996	2.7
run 2	122040	25.7	25.2	81.3	0.1	.262	.213	1.95	5.1
run 3	121960	25.6	25.2	81.3	0.1	.261	.213	3.13	8.1
run 4	121880	25.5	25.3	81.3	0.1	.262	.213	4.11	10.7

Temperature Gradient Steady State Values

	Red	error	Yellow	error	Green	error	Blue	error
run 1	-19.5	± .8	-19.5	± 1.5	20.0	± 1	-18.5	± 1.5
run 2	-44.5	± 1.5	-44.0	± 1.2	-46.5	± 1.5	-46.0	± 1.5
run 3	-71.5	± 0.8	-72.8	± 0.5	-79.5	± 1.5	-79.0	± 1
run 4	-97.5	± 1.2	-99.0	± 1	-108.2	± 0.8	-108.0	± 1.3

**APPENDIX G. ARGON AT 29 PSIA, POSITIONED HALFWAY BETWEEN
PRESSURE AND VELOCITY NODES**

Run 1 2% drive ratio



Data Run Parameters

	P _{mean} (Pa)	T _{ref} (°C)	T _{wall} (°C)	F ₀ (Hz)	time/ point (sec/ point)	δ _k (mm)	δ _v (mm)	Drive ratio (%)	Disp amp (mm)
run 1	201480	24.8	24.5	81.5	.1	.203	.165	1.99	8.5

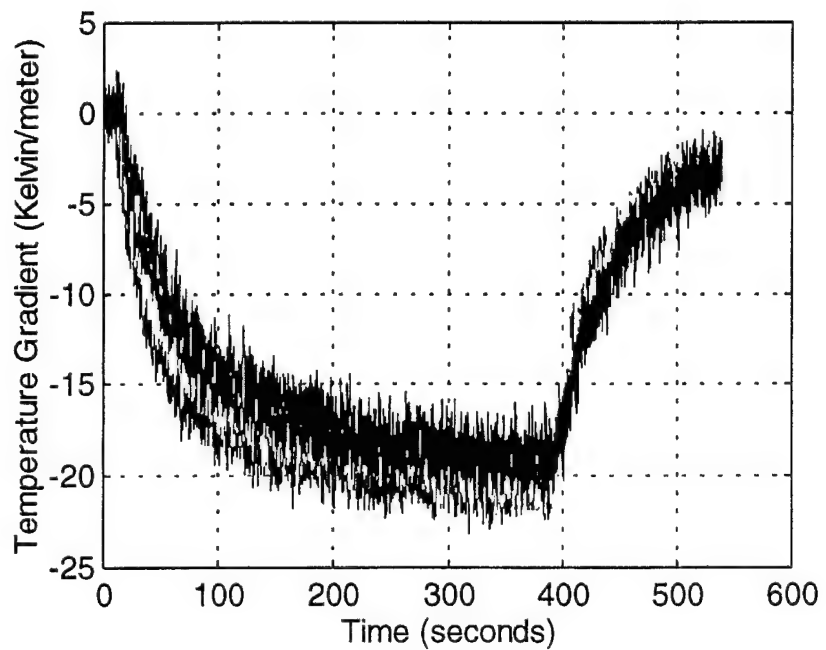
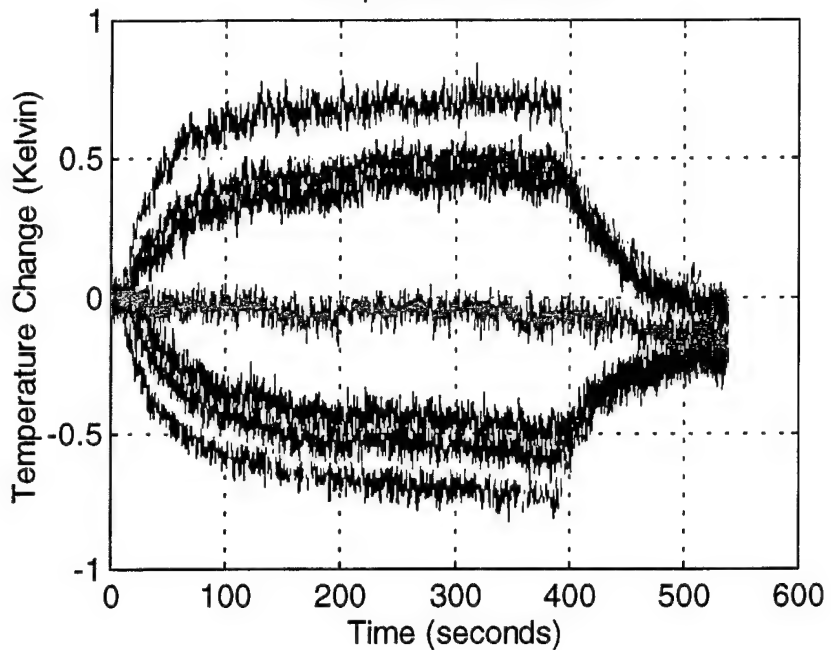
Temperature Gradient Steady State Values

	Red	error	Yellow	error	Green	error	Blue	error
run 1	-40.0	± .8	-39.2	± 1.5	-42.0	± 1	-41.3	± 1.5

**APPENDIX H. HELIUM AT 15 PSIA, POSITIONED HALFWAY BETWEEN
PRESSURE AND VELOCITY NODES**

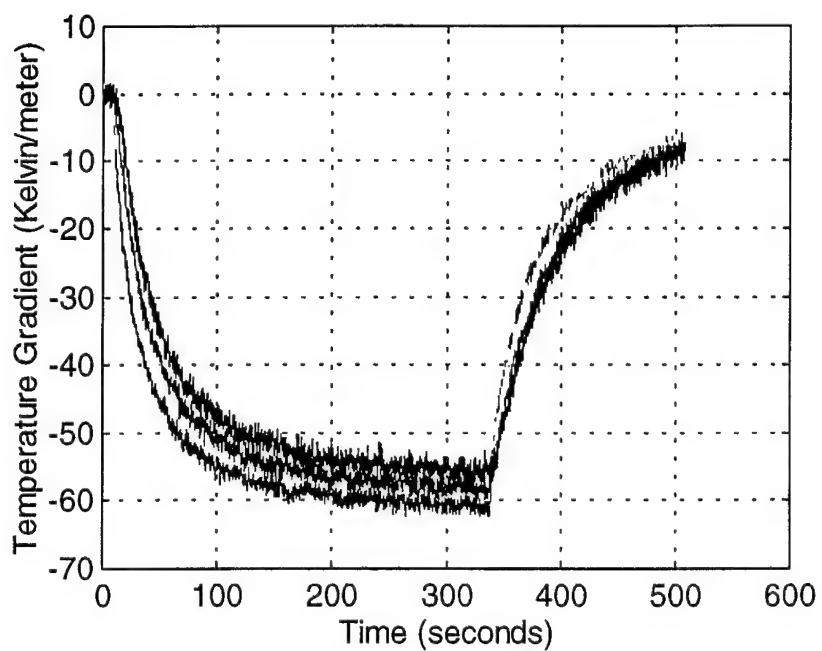
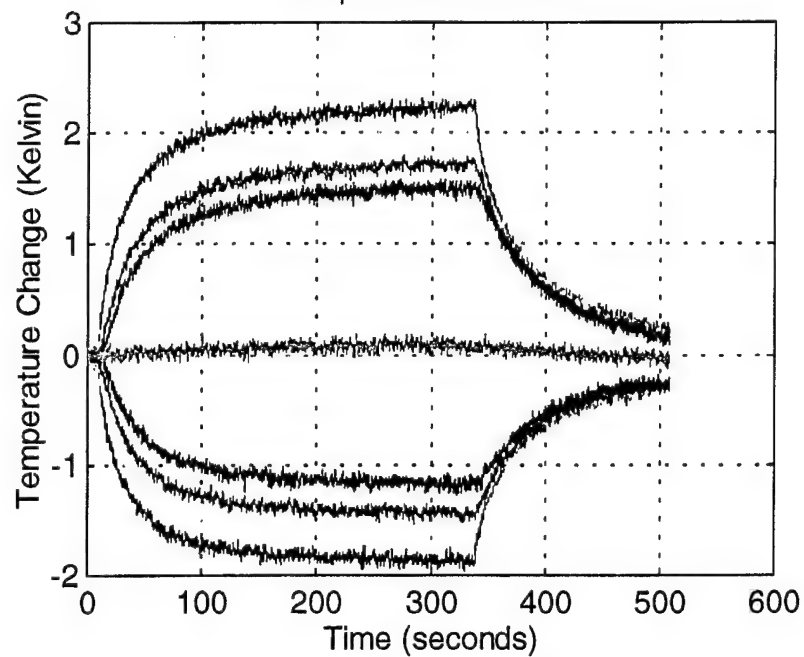
Run 1 0.5% drive ratio

Temperature Evolution

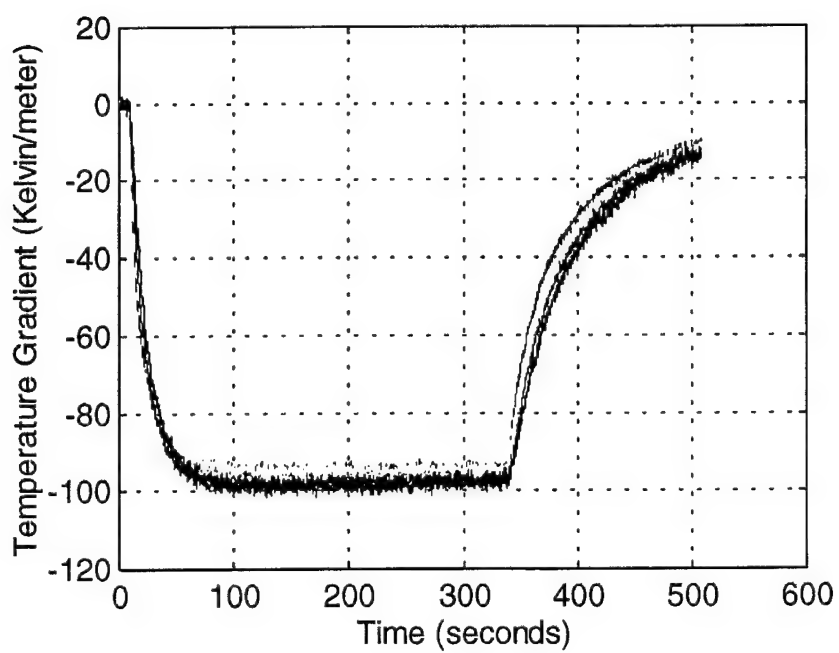
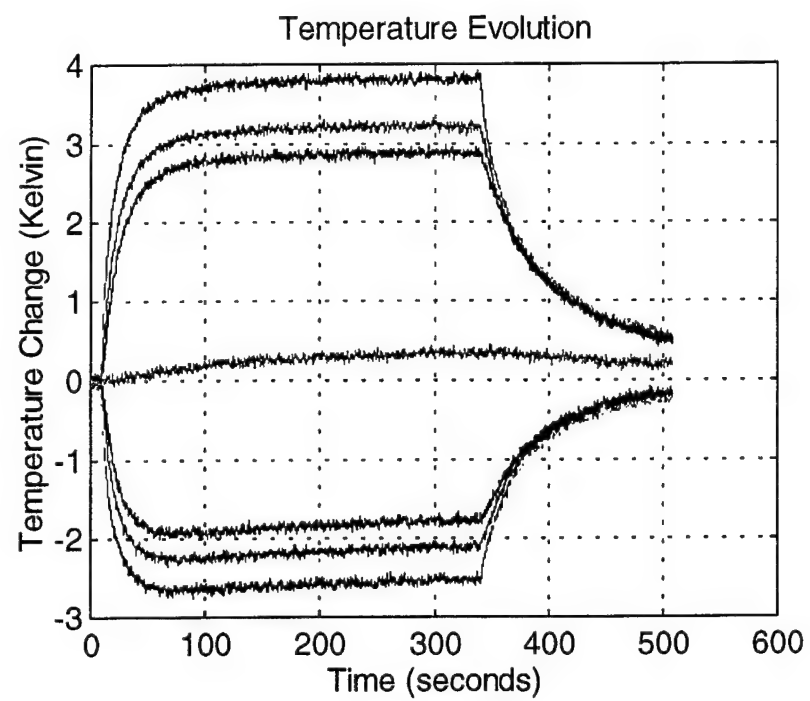


Run 2 1% drive ratio

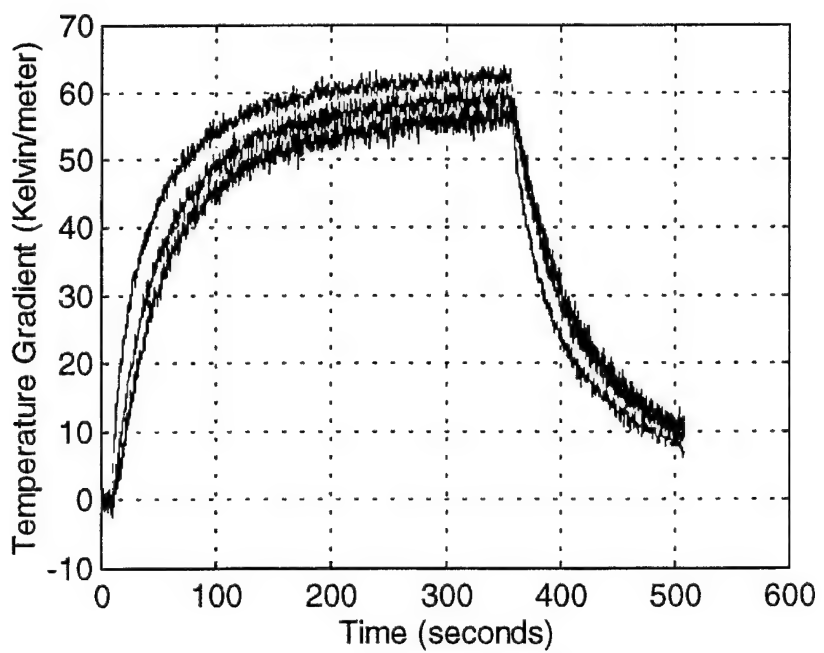
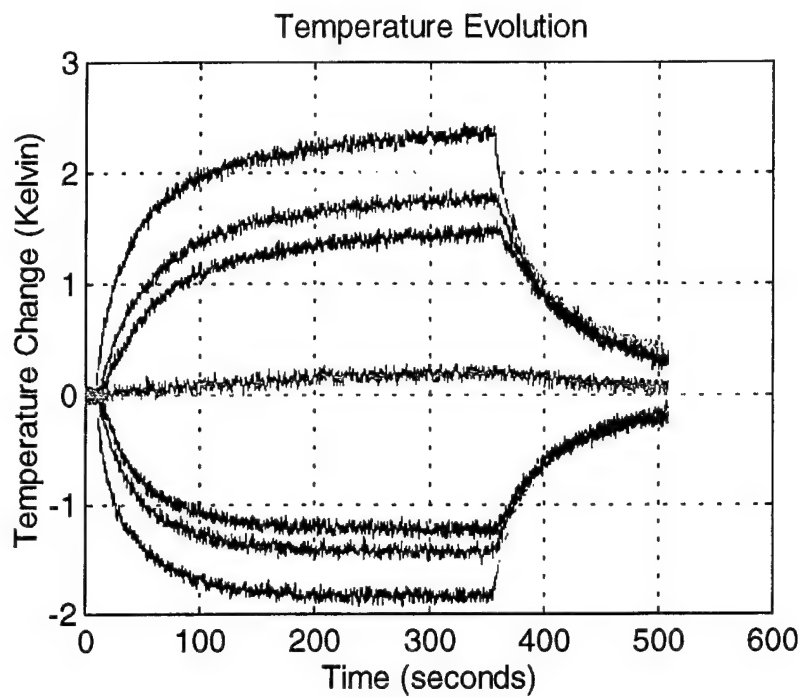
Temperature Evolution



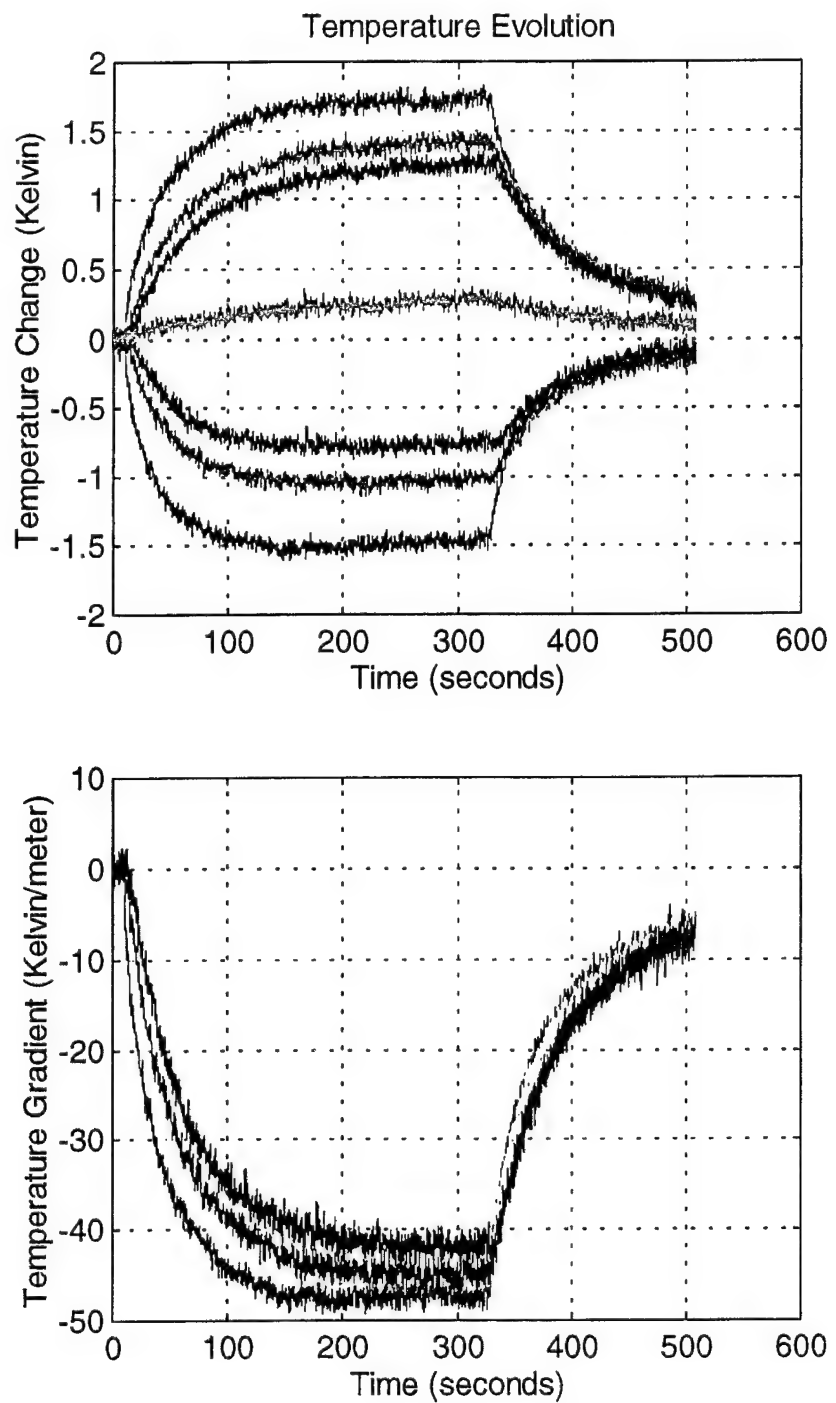
Run 3 1.5% drive ratio



Run 4 Helium w/ 1% drive ratio, 3rd frequency mode



Run 5 Helium 5psia, 1% drive ratio



Data Run Parameters

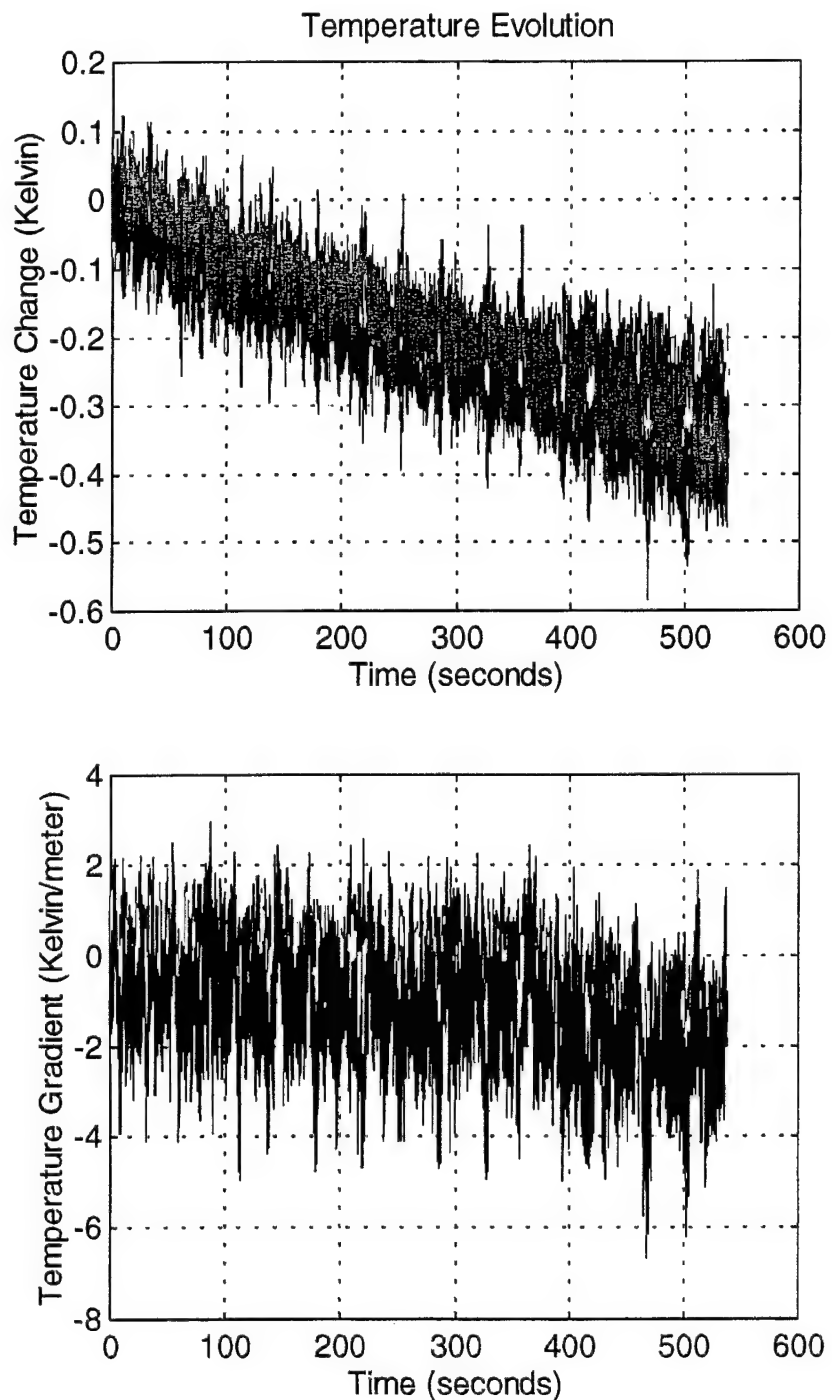
	P _{mean} (Pa)	T _{ref} (°C)	T _{wall} (°C)	F _o (Hz)	time/ point (sec/ point)	δ _k (mm)	δ _v (mm)	Drive ratio (%)	Disp amp (mm)
run 1	102460	22.2	25.0	244.1	0.1	.430	.355	.459	1.4
run 2	103470	23.6	23.8	248.9	0.1	.426	.351	.816	2.3
run 3	104040	23.5	23.5	248.9	0.1	.427	.352	1.51	4.3
run 4	104060	23.3	23.3	409.2	0.1	.366	.302	1.03	-1.5
run 5	35442	24.0	23.8	248.9	0.1	.805	.664	1.23	3.5

Temperature Gradient Steady State Values

	Red	error	Yellow	error	Green	error	Blue	error
run 1	-21.0	± 1	-20.0	± 1	-20.0	± 1	-18.5	± 1.5
run 2	-61.0	± 1.2	-58.5	± 1.5	-58.0	± 1.5	-55.5	± 2
run 3	-94.0	± 1.3	-94.5	± 1.3	-98.0	± 2	-97.0	± 2
run 4	-56.5	± 1.5	-53.0	± 2.4	-53.5	± 2	-50.0	± 2
run 5	-47.5	± 1	-45.0	± 1.3	-44.5	± 1.5	-41.5	± 2

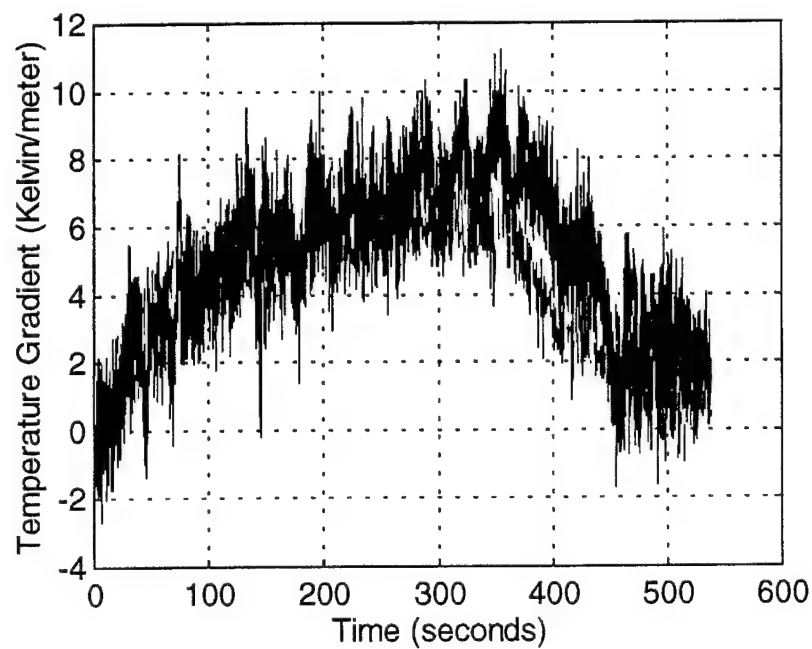
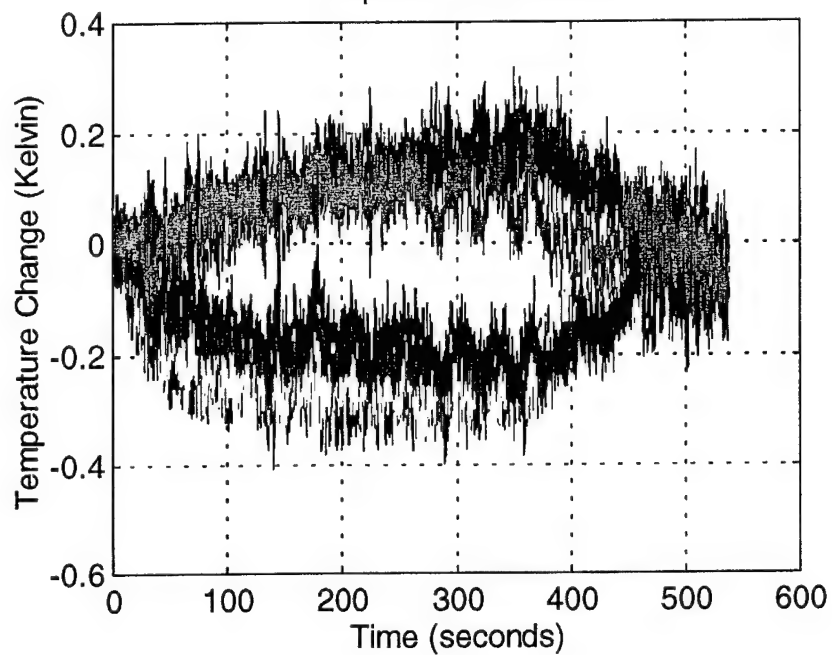
APPENDIX I: ARGON AT 5 PSIA, VELOCITY NODE

Run 1 1% drive ratio



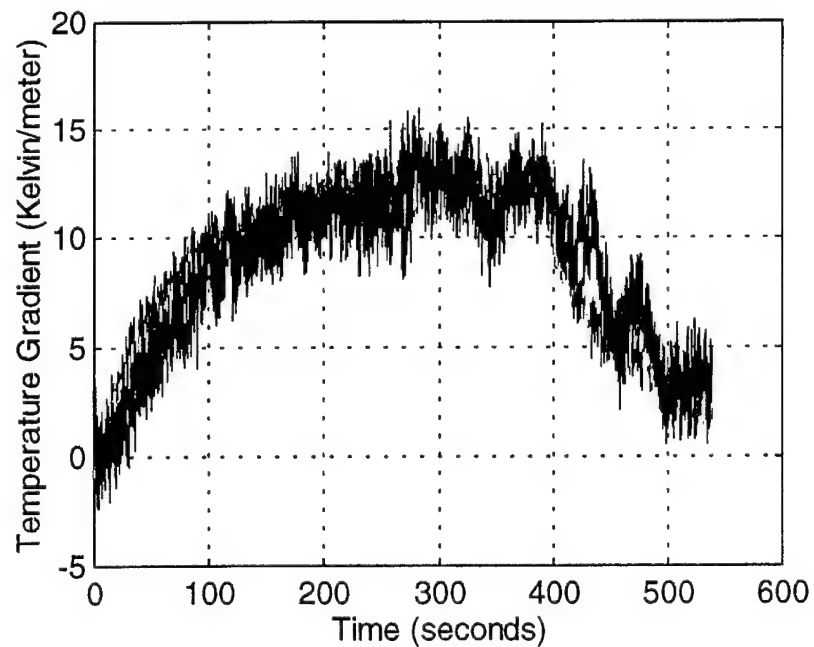
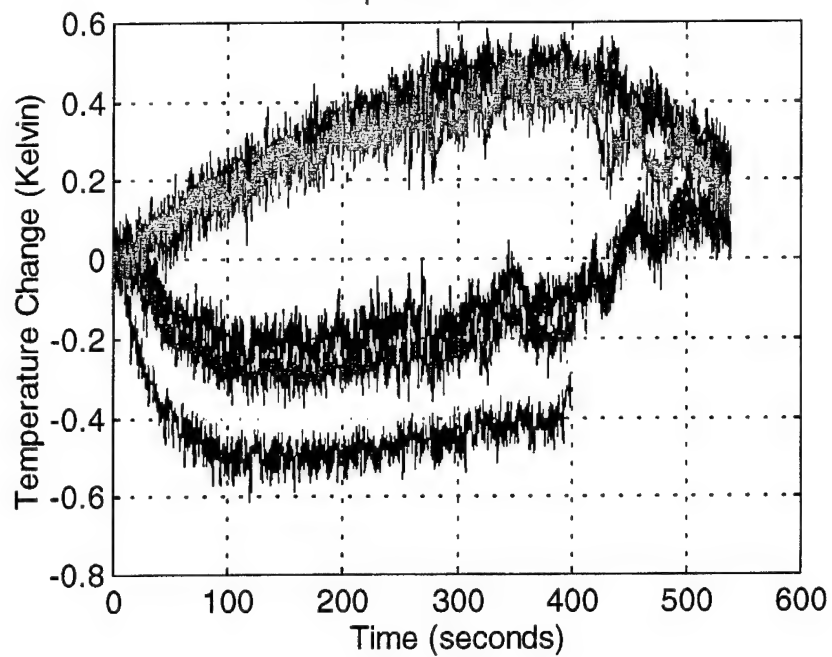
Run 2 2% drive ratio

Temperature Evolution



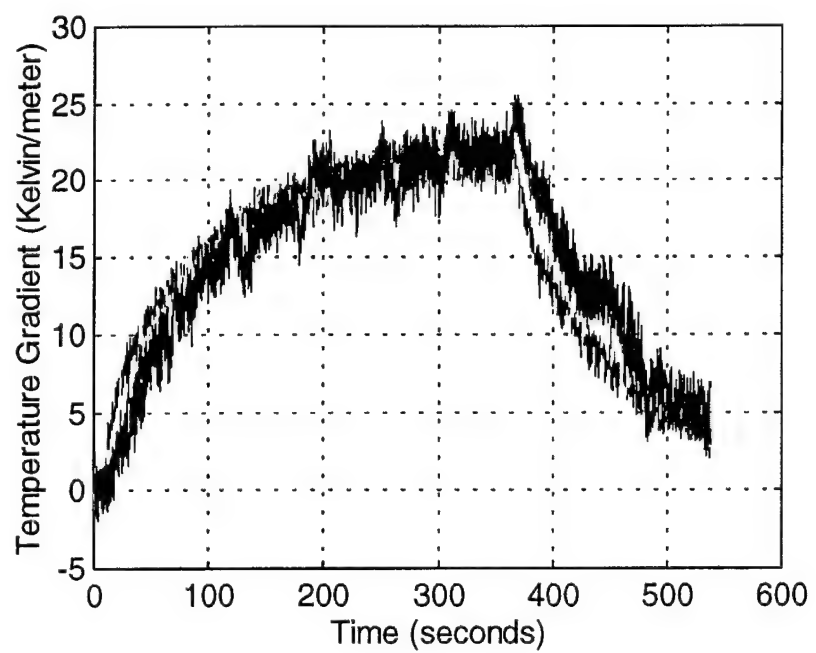
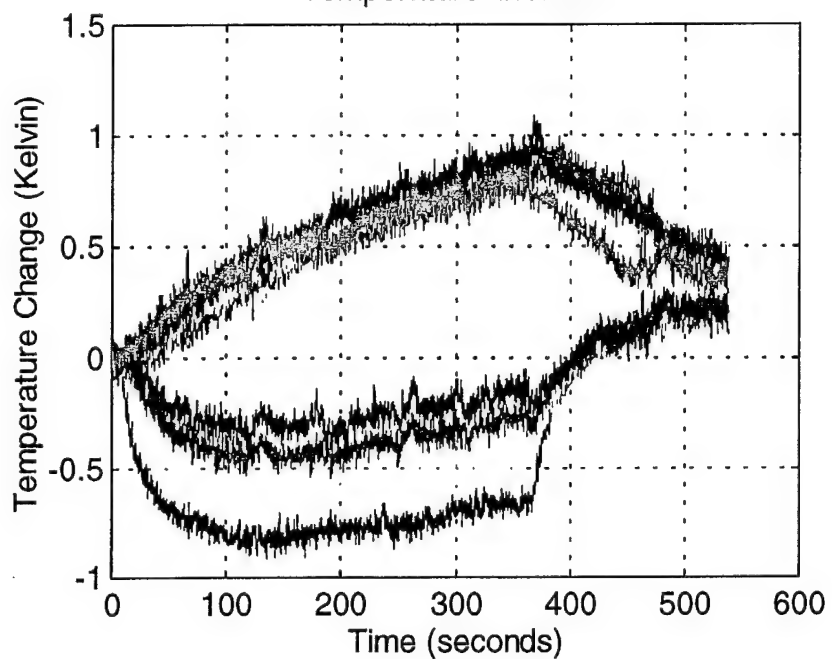
Run 3 3% drive ratio

Temperature Evolution

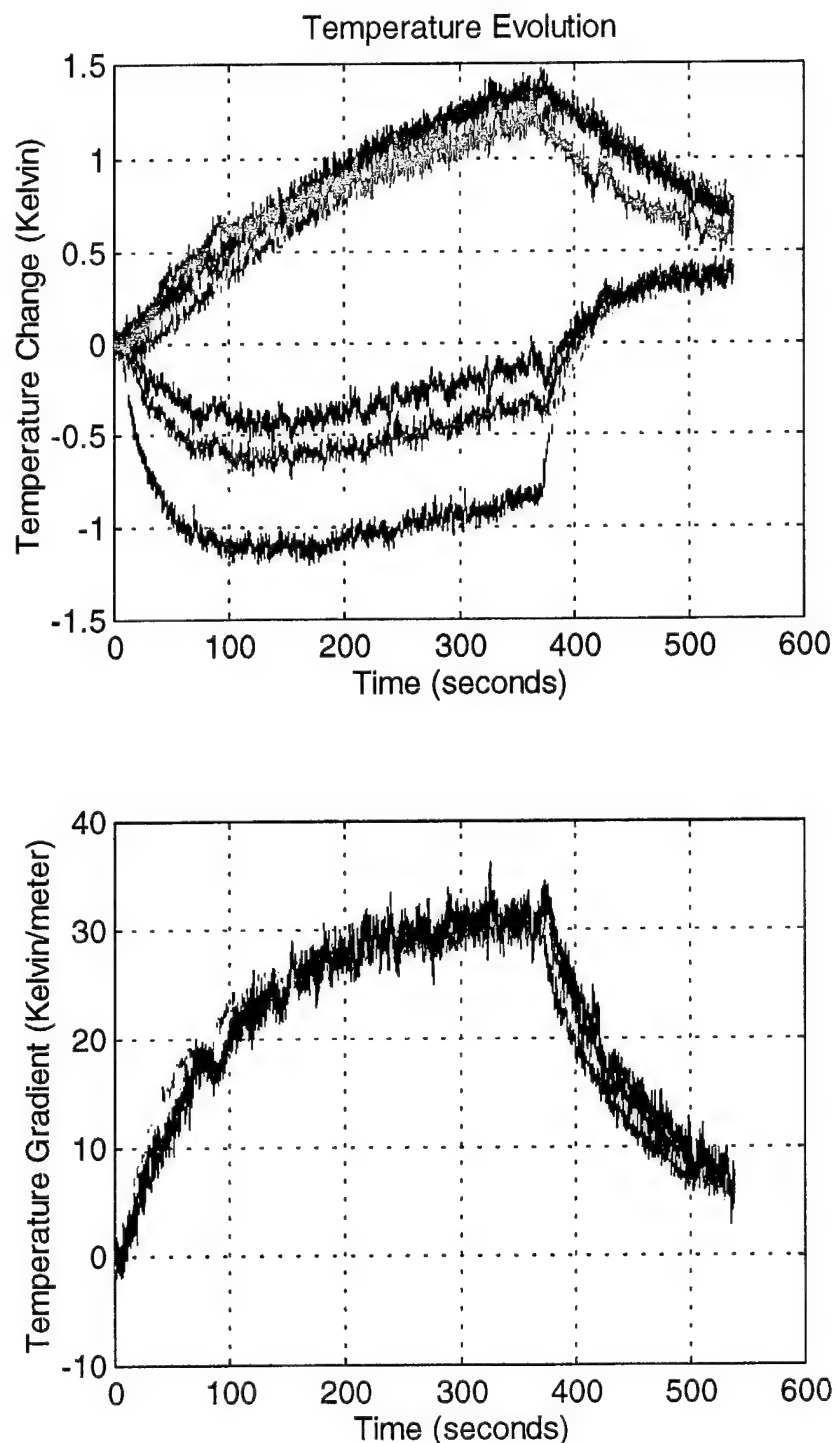


Run 4 4% drive ratio

Temperature Evolution



Run 5 5% drive ratio



Data Run Parameters

	P _{mean} (Pa)	T _{ref} (°C)	T _{wall} (°C)	F _o (Hz)	time/ point (sec/ point)	δ _k (mm)	δ _v (mm)	Drive ratio (%)	Disp amp (mm)
run 1	36322	24.5	26.1	79.4	0.1	.486	.396	0.96	2.72
run 2	36543	25.1	25.8	79.4	0.1	.484	.394	2.08	5.9
run 3	36741	24.2	25.8	79.4	0.1	.483	.393	2.97	8.4
run 4	36977	24.4	25.8	79.4	0.1	.481	.392	3.98	11.2
run 5	37247	24.0	26.0	79.4	0.1	.480	.390	4.88	13.8

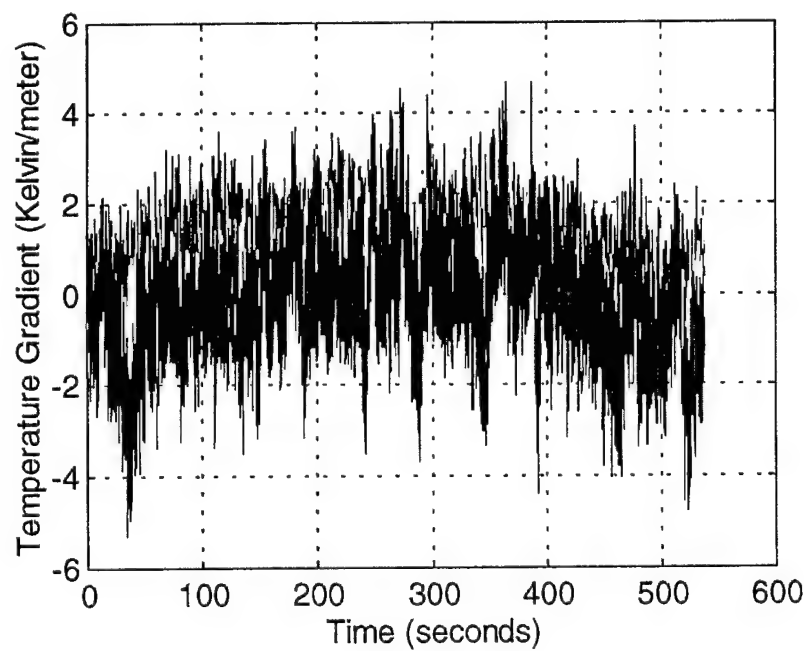
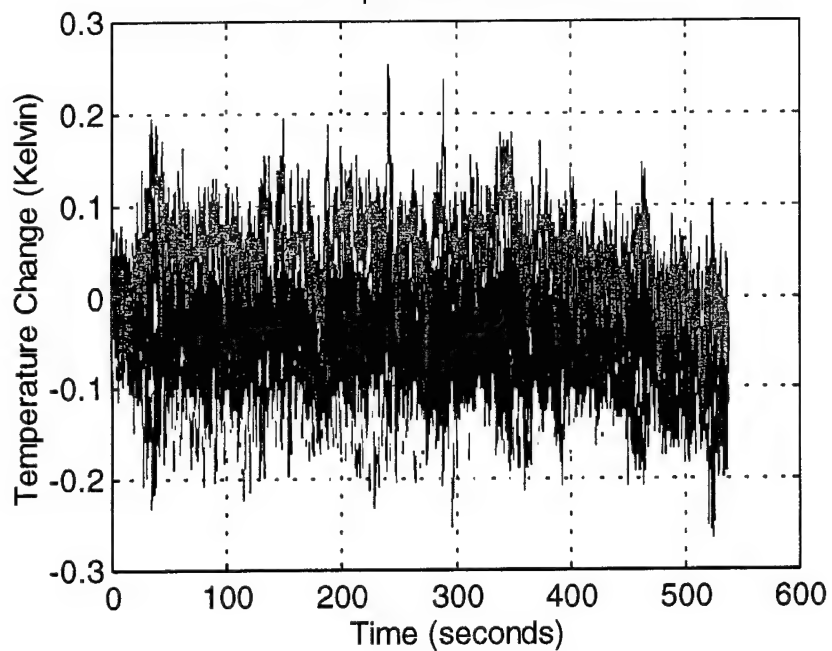
Temperature Gradient Steady State Values

	Red	error	Yellow	error	Green	error	Blue	error
run 1	0.5	± 1	-1.0	± 1	-1.5	± 1.3	-1.75	± 2
run 2	6.5	± 1	7.5	± 1.5	7.5	± 2	8.0	± 2.5
run 3	12.5	± 1.5	12.5	± 2	12.0	± 2.5	12.0	± 2.5
run 4	21.0	± 1	21.0	± 1	22.0	± 1	22.0	± 2
run 5	30.0	± 1.4	30.2	± 1	31	± 1	31.0	± 2

APPENDIX J: ARGON AT 10 PSIA, VELOCITY NODE

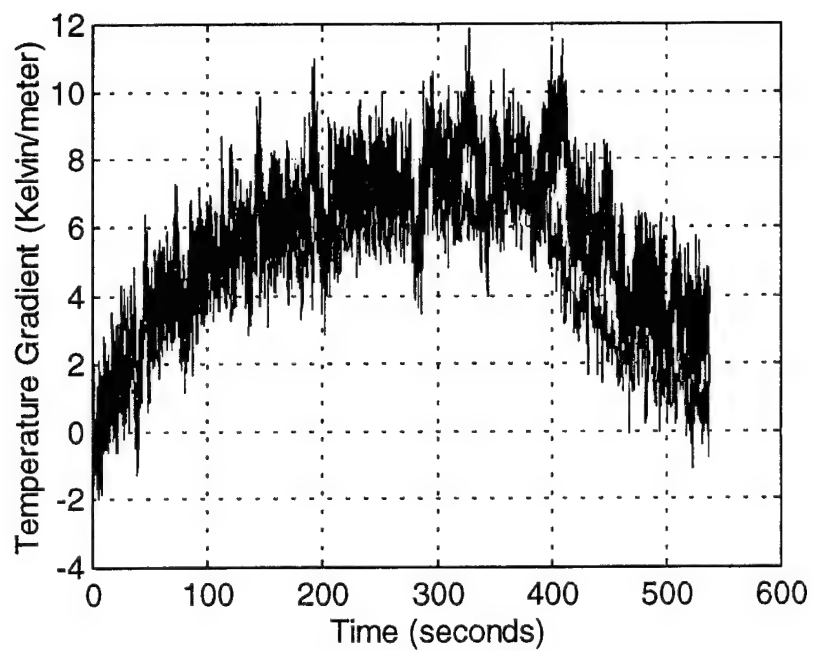
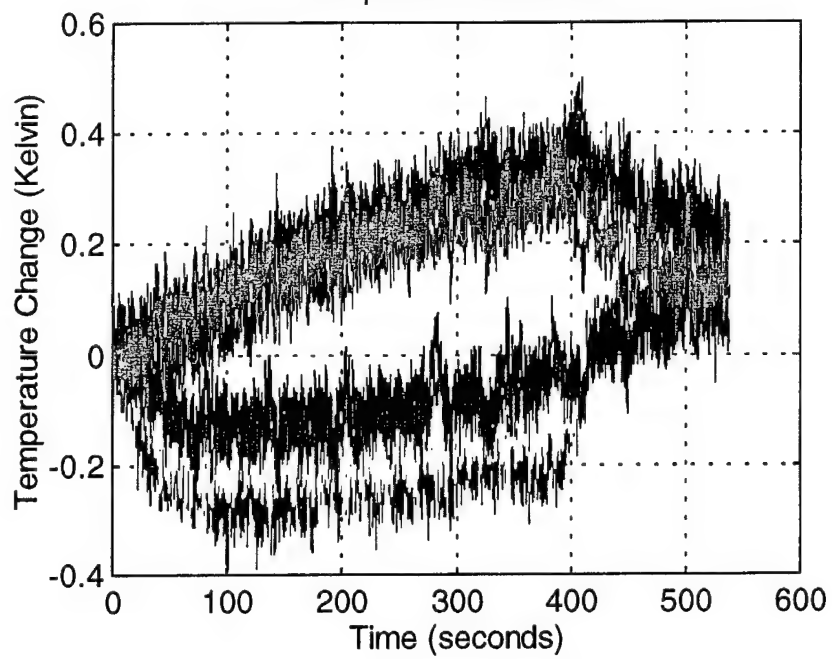
Run 1 1% drive ratio

Temperature Evolution

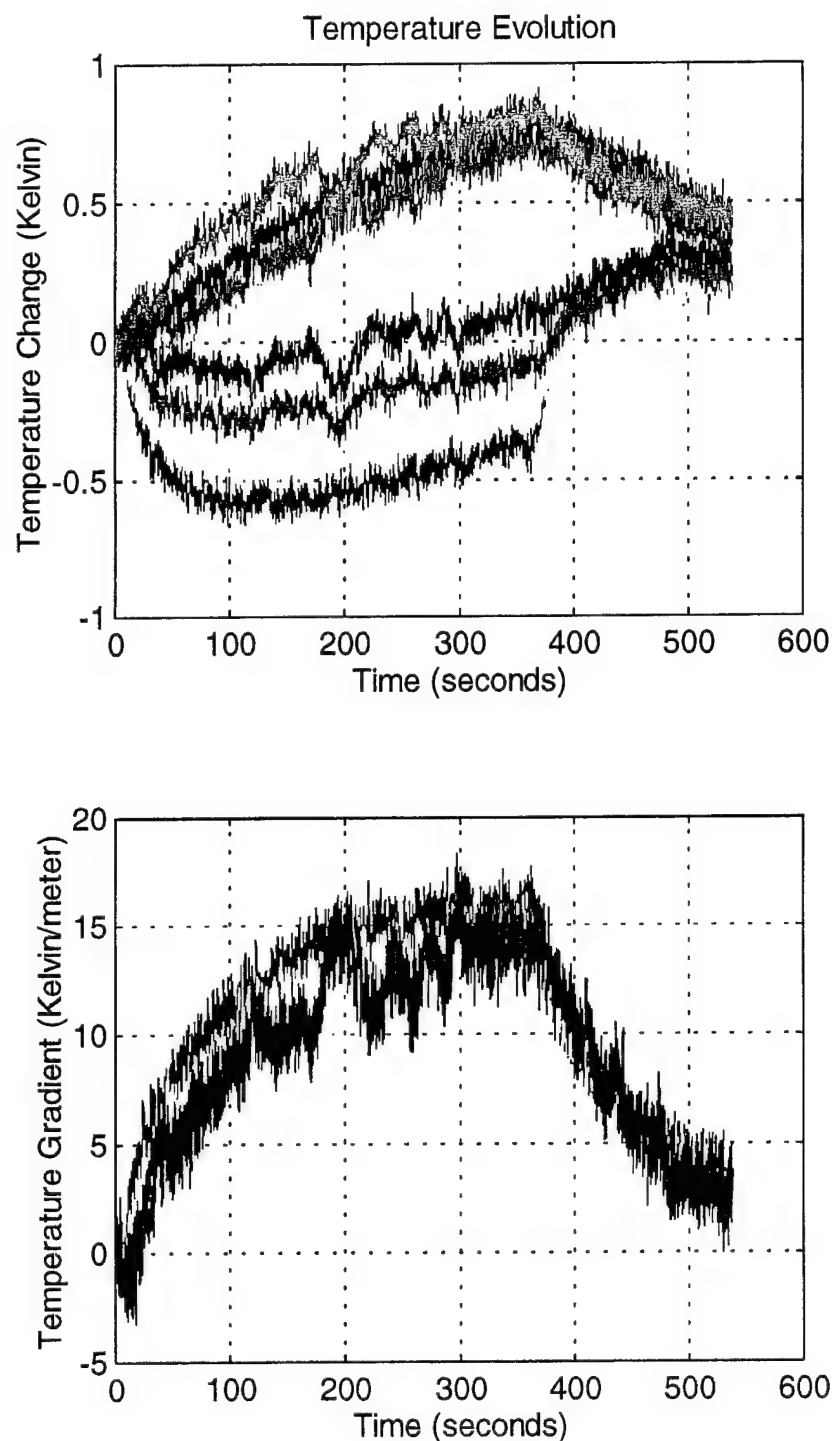


Run 2 2% drive ratio

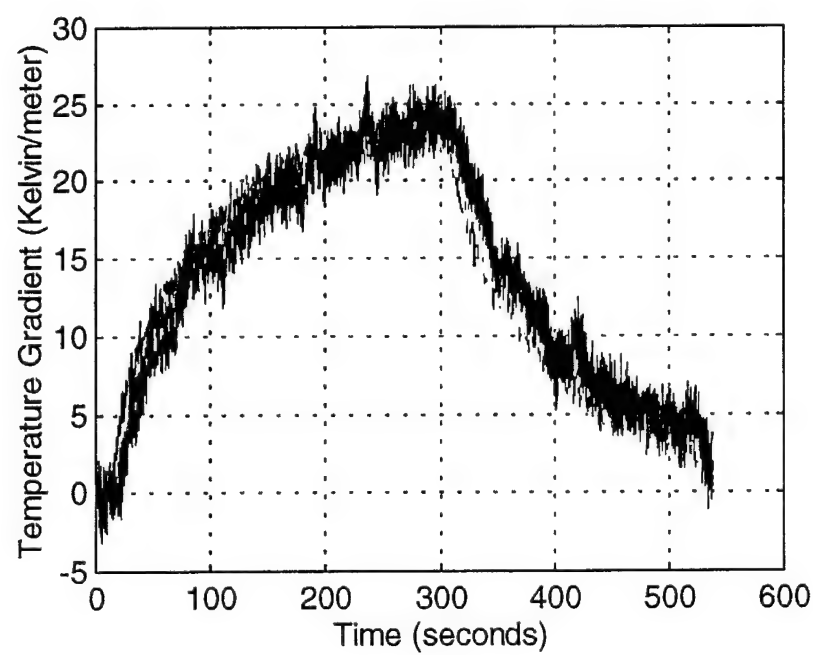
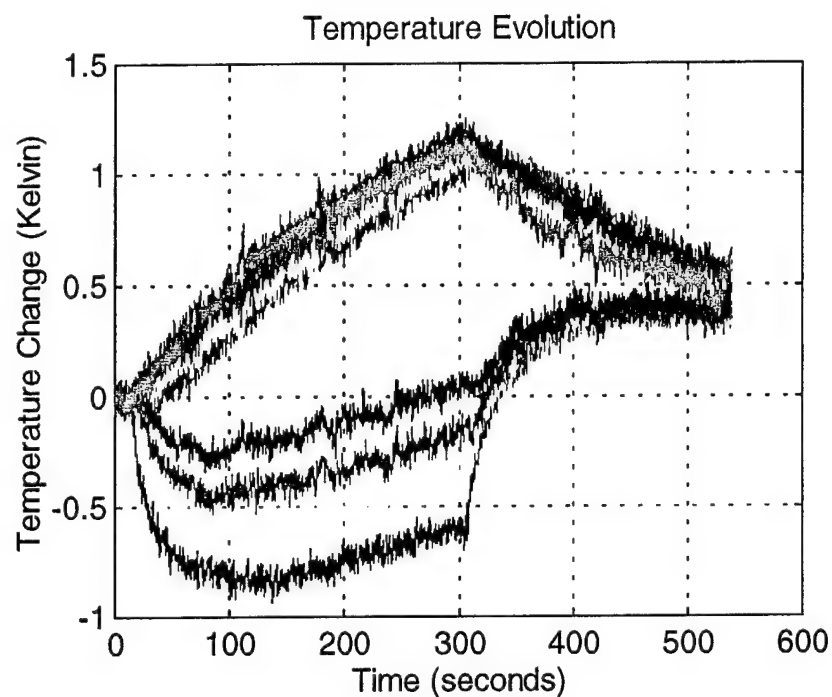
Temperature Evolution



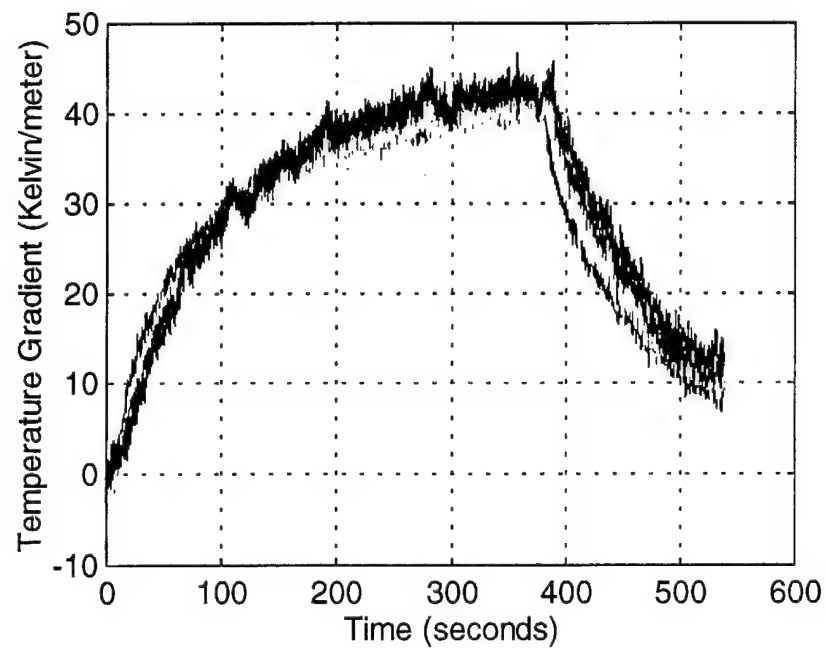
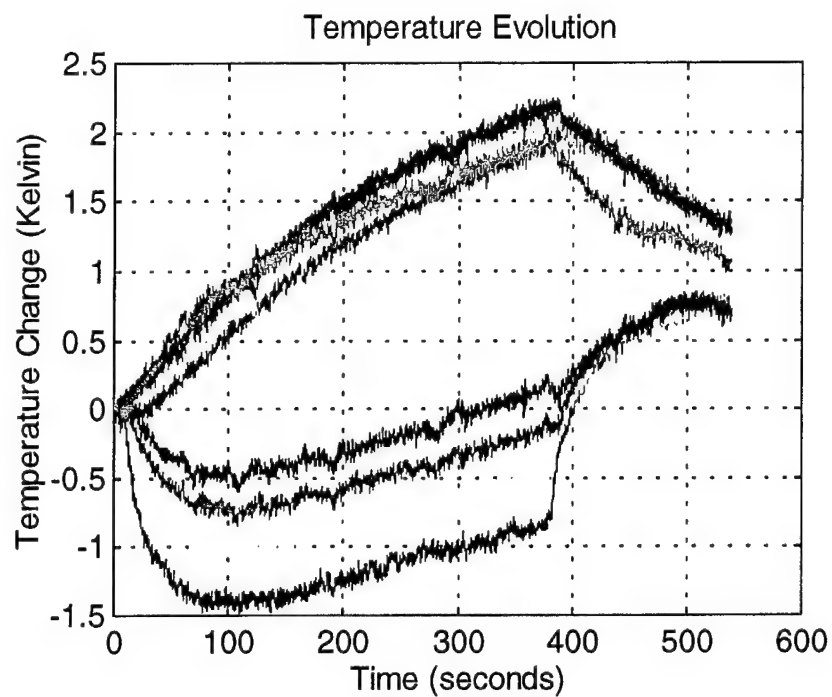
Run 3 3% drive ratio



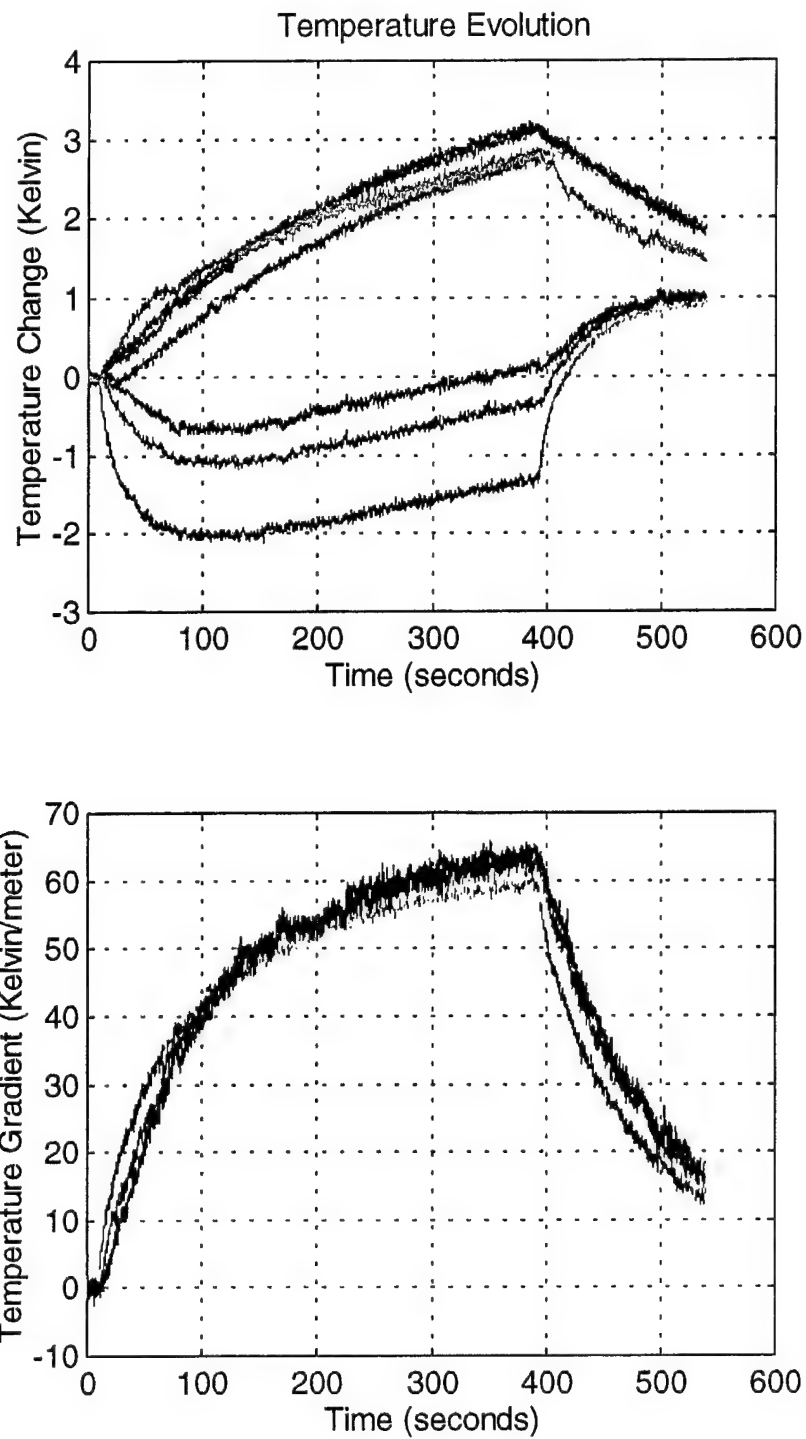
Run 4 4% drive ratio



Run 5 5% drive ratio



Run 6 6% drive ratio



Data Run Parameters

	P _{mean} (Pa)	T _{ref} (°C)	T _{wall} (°C)	F _o (Hz)	time/ point (sec/ point)	δ _k (mm)	δ _v (mm)	Drive ratio (%)	Disp amp (mm)
run 1	69355	23.9	25.6	79.4	0.1	.351	.286	1.10	3.1
run 2	69487	23.8	25.5	79.4	0.1	.351	.286	2.12	6.0
run 3	69022	23.9	25.4	79.4	0.1	.352	.286	3.13	8.8
run 4	69685	24.1	25.4	79.4	0.1	.350	.285	4.03	11.4
run 5	69518	24.1	25.6	79.4	0.1	.354	.288	5.12	14.4
run 6	68981	24.2	26.0	79.4	0.1	.353	.287	6.32	17.9

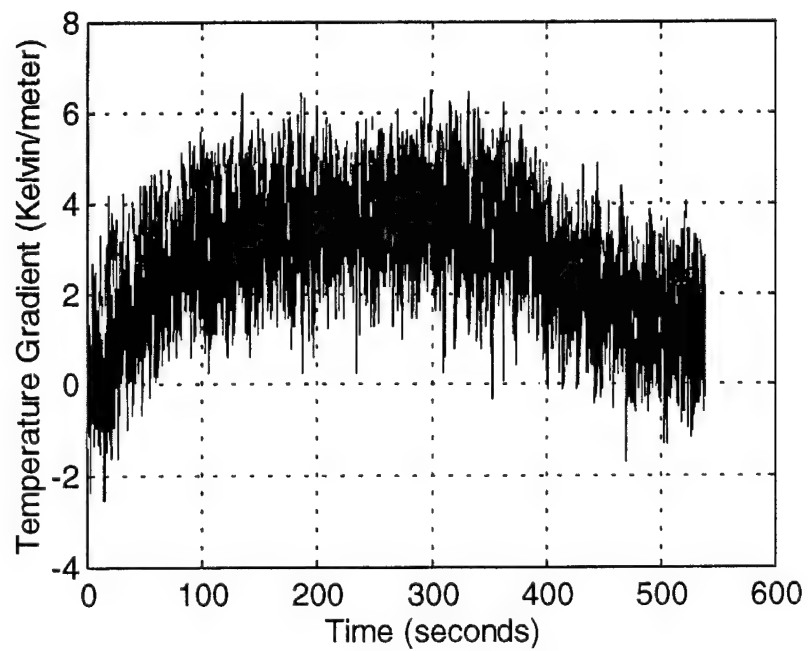
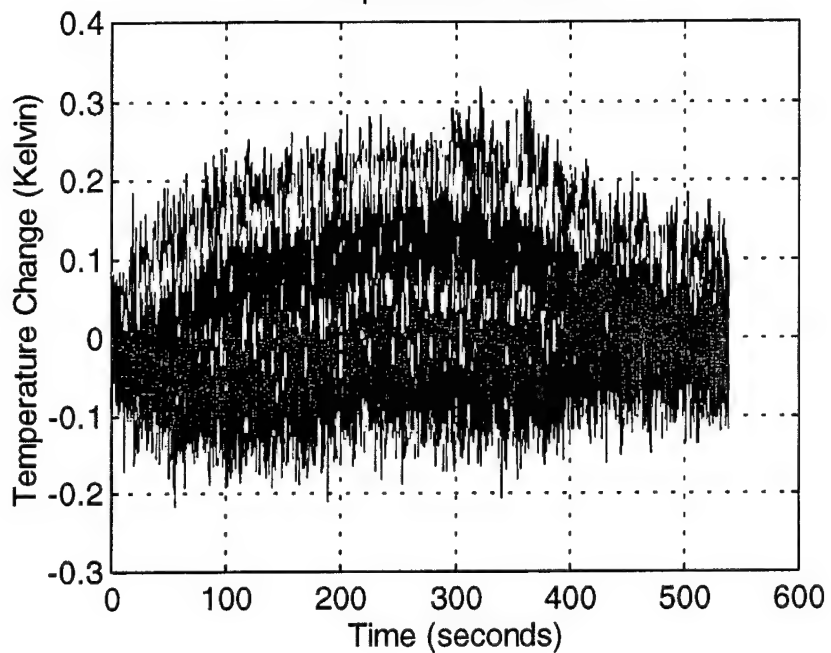
Temperature Gradient Steady State Values

	Red	error	Yellow	error	Green	error	Blue	error
run 1	2.0	± 1.5	1.0	± 1.5	0.3	± 1.5	0.5	± 2
run 2	6.5	± 0.75	7.5	± 1.5	7.5	± 2	8.5	± 2.5
run 3	15.8	± 1.3	15.0	± 0.75	14.5	± 1.5	14.0	± 2
run 4	23.5	± 1	23.0	± 1.5	24.0	± 2	23.8	± 2.5
run 5	39.5	± 1.5	40.0	± 1	42.0	± 2	41.5	± 2.5
run 6	59.0	± 1	61.0	± 1.5	63.0	± 1.5	63.0	± 2

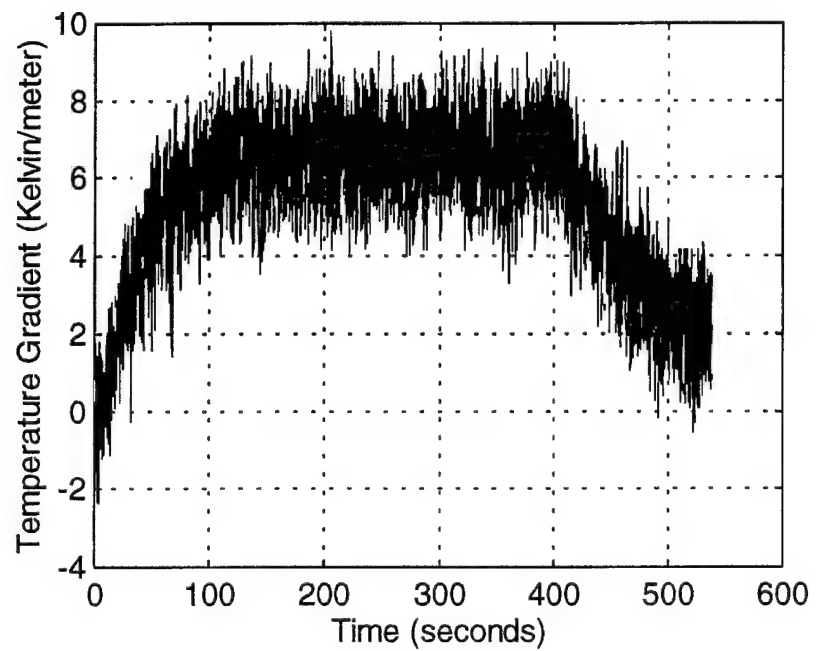
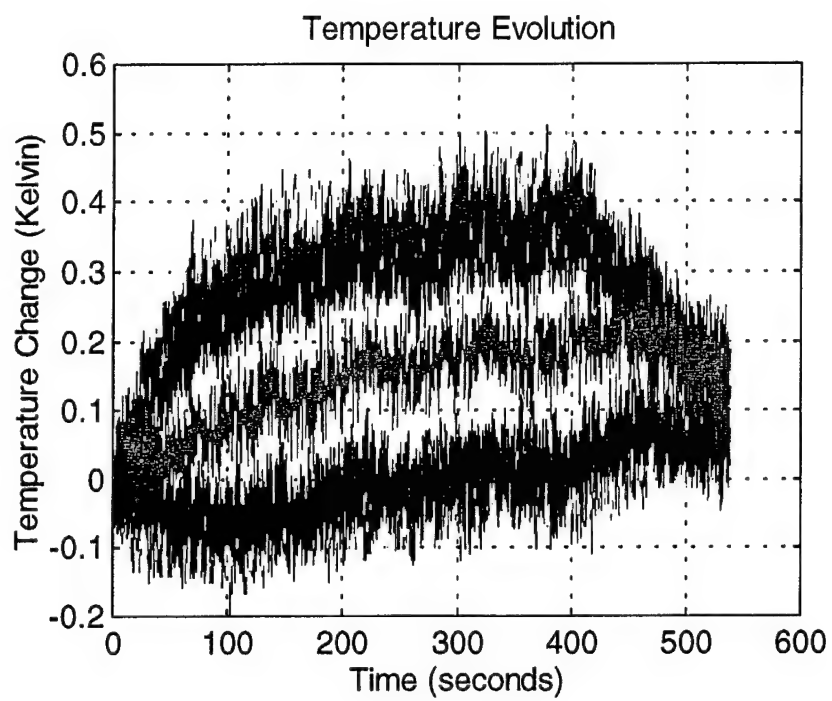
APPENDIX K. ARGON AT 10 PSIA, PRESSURE NODE

Run 1 1% drive ratio

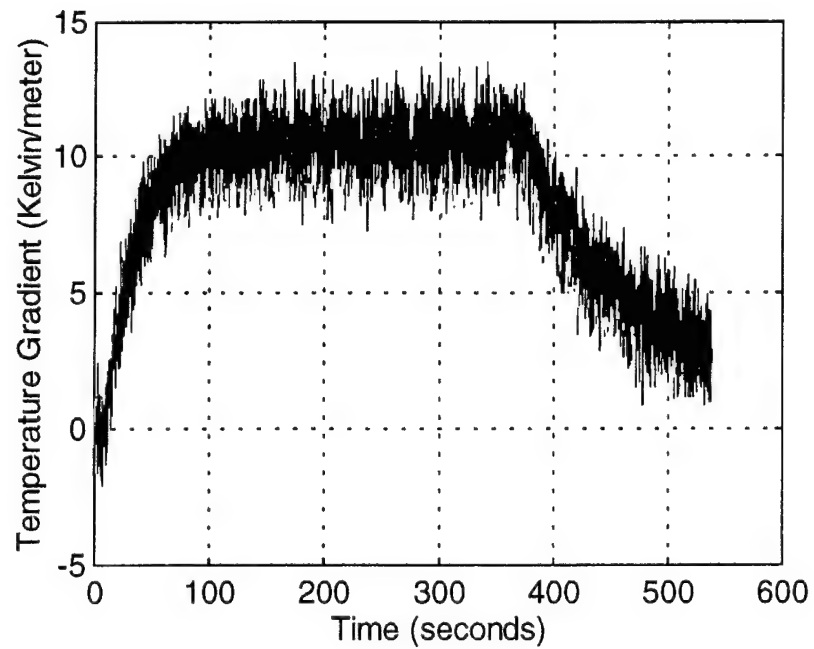
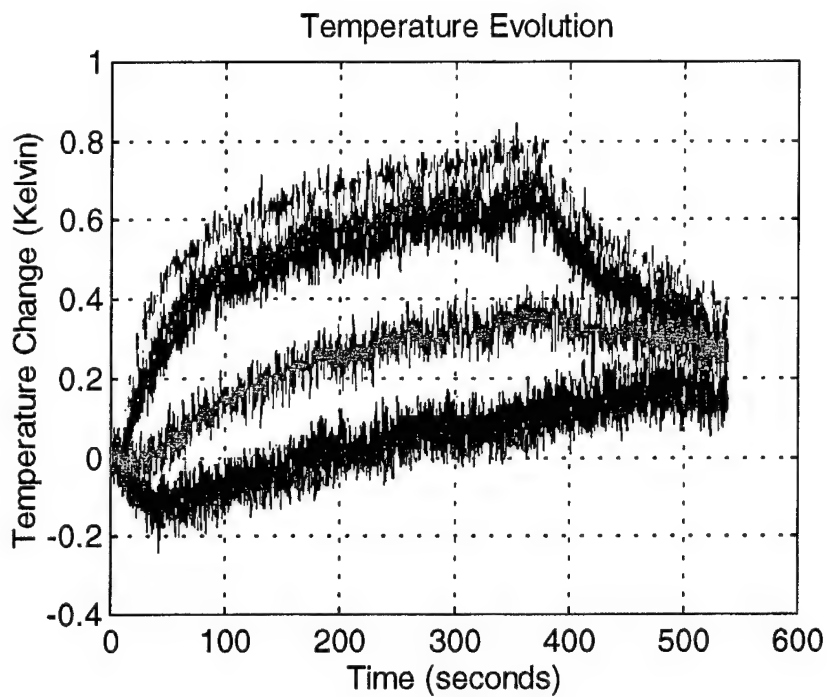
Temperature Evolution



Run 2 2% drive ratio

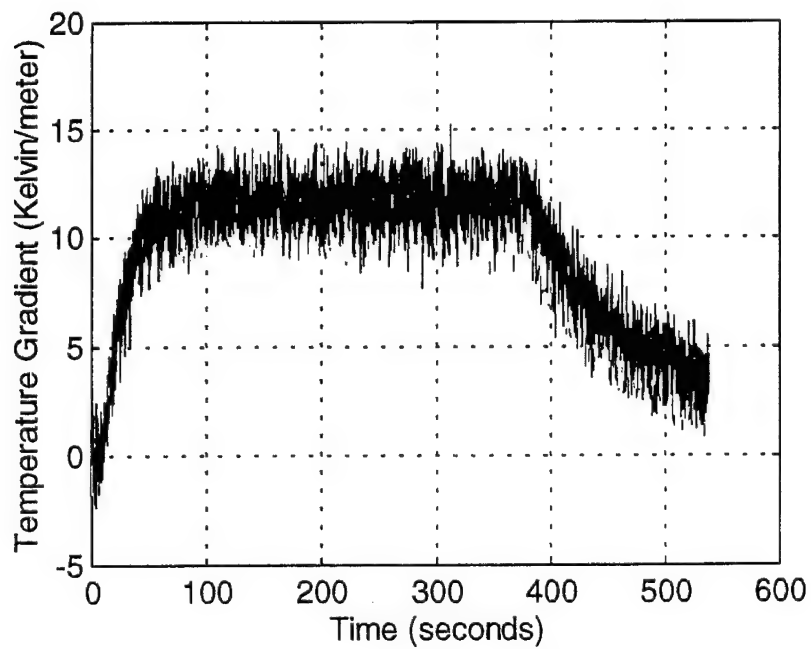
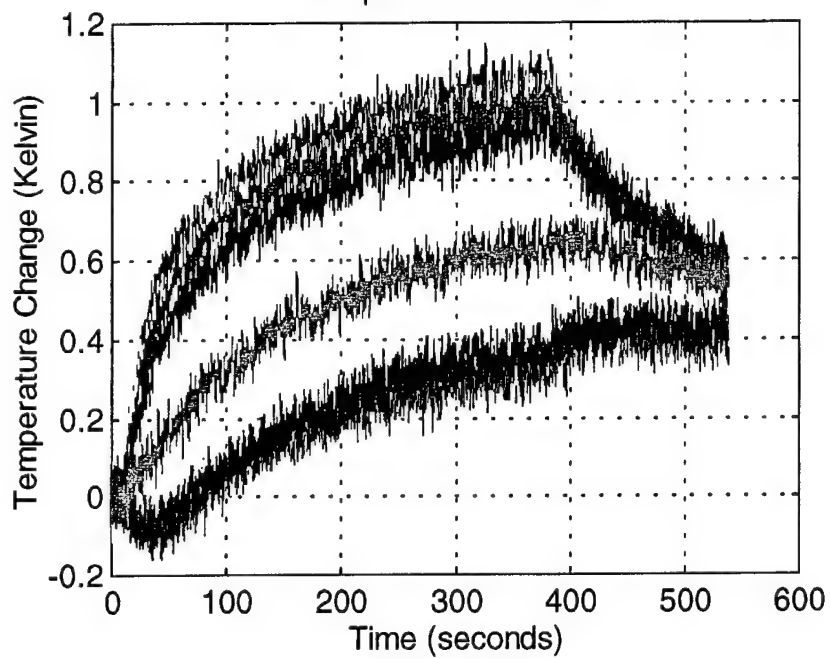


Run 3 3% drive ratio



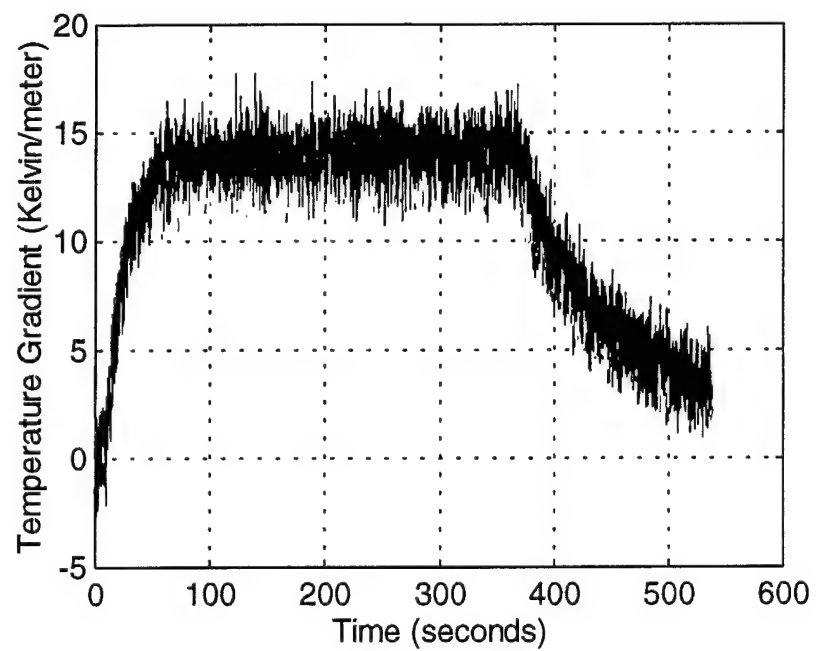
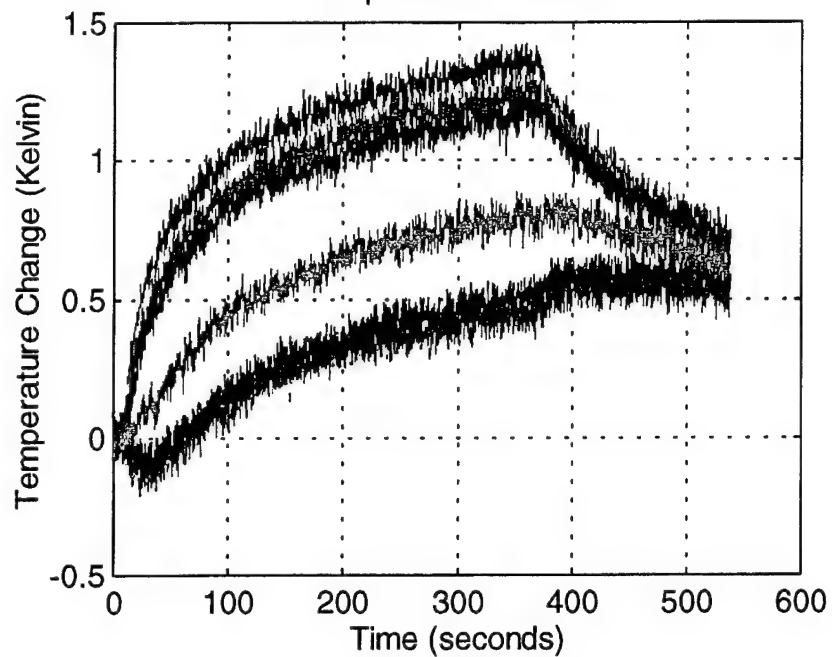
Run 4 drive ratio 4%

Temperature Evolution



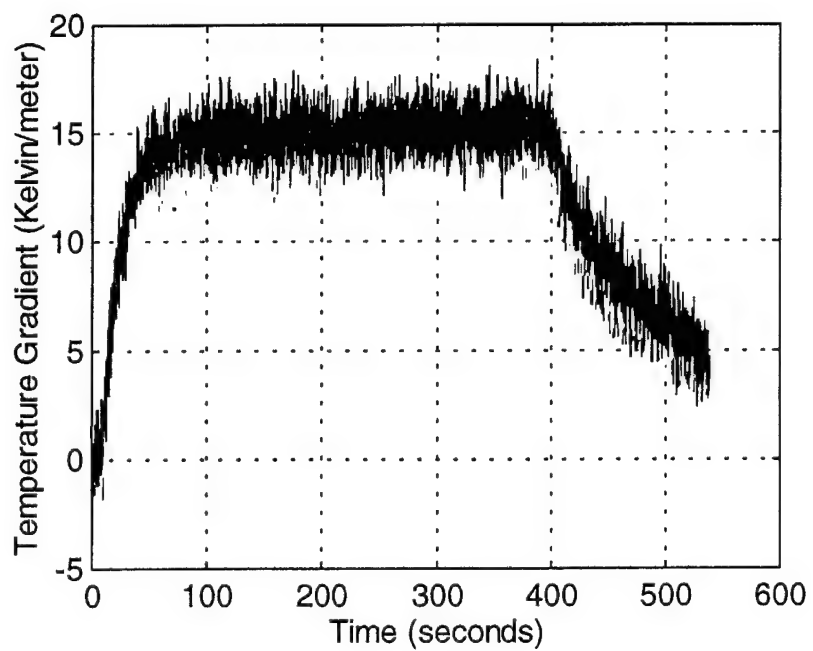
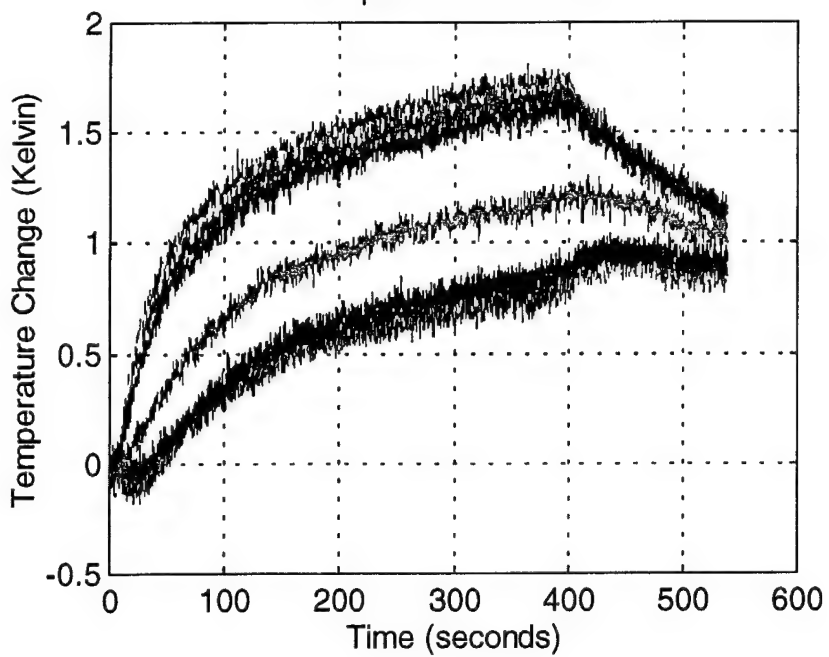
Run 5 5% drive ratio

Temperature Evolution



Run 6 6% drive ratio

Temperature Evolution



Data Run Parameters

	P _{mean} (Pa)	T _{ref} (°C)	T _{wall} (°C)	F _o (Hz)	time/ point (sec/ point)	δ _k (mm)	δ _v (mm)	Drive ratio (%)	Disp amp (mm)
run 1	68580	23.2	24.8	78.52	0.1	.354	.289	1.07	3.1
run 2	68754	23.3	24.8	78.52	0.1	.354	.288	2.03	5.92
run 3	69018	23.3	25.0	78.52	0.1	.354	.288	2.96	8.6
run 4	68331	23.5	25.2	78.92	0.1	.355	.289	4.07	11.7
run 5	68694	23.6	25.5	78.92	0.1	.354	.288	5.31	15.3
run 6	69183	23.8	25.6	78.92	0.1	.353	.287	5.97	17.2

Temperature Gradient Steady State Values

	Red	error	Yellow	error	Green	error	Blue	error
run 1	4.5	± 1	4.0	± 1	3.8	± 2	3.5	± 2.5
run 2	6.0	± 1	6.8	± 1.3	7.0	± 1.75	7.0	± 2.5
run 3	10.0	± 1	9.5	± 1	10.5	± 2	10.5	± 2.5
run 4	11.0	± 1	10.5	± 1	12.0	± 1.5	11.5	± 2
run 5	13.5	± 1	12.5	± 1	14.5	± 1	14.0	± 2
run 6	14.5	± 0.75	13.0	± 1	15.5	± 1.5	15.0	± 2

LIST OF REFERENCES

1. A.A. Atchley, T.J. Hofler, M.L. Muzerall, M.D. Kite, and C. Ao, "Acoustically generated temperature gradients in short plates," *J. Acoust. Soc. Am* 88 (1), July 1990.
2. A. Prosperetti, M. Watanbe, and H. Yuan, "A Simplified Model For Linear and Nonlinear Processes In Thermoacoustic Prime Movers," in progress.
3. A.S. Worlikar, O.M. Knio, and R. Klien, "Numerical study of unsteady, thermally stratified flow in an idealized thermoacoustic stack," *J. Acoust. Soc. Am* 100, Oct 1996.
4. John Wheatley, T. Hofler, G.W. Swift, and A. Migliori, "Understanding some simple phenomena in thermoacoustics with applications to acoustical heat engines," *Am. J. Phys.* 53 (2), February 1985.
5. John Wheatley, T. Hofler, G.W. Swift, and A. Migliori, "An intrinsically irreversible thermoacoustic heat engine," *J. Acoust. Soc. Am* 74 (1), July 1983.
6. G.W. Swift, "Thermoacoustic engines," *J. Acoust. Soc. Am.* 84, 1145-1180 (1988).
7. G.W. Swift, "Thermoacoustic engines and refrigerators," For *Encyclopedia of Applied Physics*; in progress.
8. John Wheatley and Arthur Cox, "Natural engines," *Physics Today*, 50-58, August 1995.
9. G.W. Swift, "Thermoacoustic Engines and Refrigerators," *Physics Today*, 22-28, July 1995.
10. "OMEGA Complete Temperature Measurement Handbook and Encyclopedia," Omega Engineering Inc., Stamford, CT, 1988.
11. National Instruments, "LabVIEW user Manual for Macintosh," National Instruments Corporation, Austin, Texas, 1994.
12. National Instruments, "LabVIEW Data Acquisition VI Reference Manual for Macintosh," National Instruments Corporation, Austin, Texas, 1994.

DISTRIBUTION LIST

1. Defense Technical Information Center.....2
8725 John J. Kingman Road., Ste 0944
Ft. Belvoir, VA 22060-6218
2. Dudley Knox Library.....2
Naval Postgraduate School
411 Dyer Rd.
Monterey, CA 93943-5101
3. Professor Anthony Atchley.....5
Department of Physics
Naval Postgraduate School
Monterey, CA 93943
4. Professor Thomas Hofler.....1
Department of Physics
Naval Postgraduate School
Monterey, CA 93943
5. Professor Robert Keolian.....1
Department of Physics
Naval Postgraduate School
Monterey, CA 93943
6. Dr. G.W. Swift.....1
Condensed Matter & Thermal Physics (P-10)
Los Alamos National Lab
P.O. Box 1667/MS 764
Los Alamos, NM 87545
7. Dr. Henry E. Bass.....1
National Center for Physical Acoustics
Coliseum Drive
University of Mississippi
University, MS 38677
8. Dr. L.E. Hargrove.....1
ONR 331
Office of Naval Research
800 N. Quincy Street
Arlington, VA 22217-5660

9.	LCDR Arthur R. Salindong, USN.....	2
	11475 Corley Ct.	
	San Diego, CA 92126	
10.	LT David D. Hebert, USN.....	2
	35124 W. Jefferson	
	Rockwood, MI 48173	
11.	Major Lin, Hsiao-Tseng.....	1
	SGC #2252, Naval Postgraduate School	
	Monterey, CA 93943	
12.	Dr. Andrea Prosperetti.....	1
	Department of Mechanical Engineering	
	122 Latrobe Hall	
	Johns Hopkins University	
	Baltimore, MD 21218	